PART 1. EMISSIVITY CALCULATIONS FOR CO_2

PART 2. SHOCK TUBE f-NUMBER MEASUREMENT FOR OH

Thesis by

Marshall Lapp

In Partial Fulfillment of the Requirements
For the Degree of
Doctor of Philosophy

California Institute of Technology
Pasadena, California
1960

To My Wife

ACKNOWLEDGEMENTS

The author is deeply indebted to Dr. S. S. Penner for suggesting these investigations and for helpful discussions and suggestions during the course of the work. He also expresses his appreciation to D. Olfe and Drs. H. Takeyama and U. Oppenheim for interesting discussions.

The author is grateful to the Rand Corp. and in particular to W. Sibley, for assistance in the machine computation of the shock tube state functions.

Financial assistance for the first two academic years was provided by a Daniel and Florence Guggenheim Jet Propulsion Fellowship. The research described in Part 1 was supported by the Physics Branch of the Office of Naval Research, U.S. Navy, under Contract Nonr-220(03), NR 015 401. The research described in Part 2 was supported by the Air Force Office of Scientific Research of the Air Research and Development Command, U.S. Air Force, under Contract AF 18(603)-2.

The author expresses his gratitude to Mrs. Barbara Rickert for the careful typing of this manuscript.

ABSTRACT
Part 1

A model has been developed for the calculation of total emissivities of polyatomic molecules at elevated temperatures in terms of room temperature measurements and of a few parameters characteristic of the major known regions of emission. The model involves a statistical redistribution of the theoretically available intensities throughout these regions. Using this model, emissivities of CO_2 have been calculated at 600°K for optical depths up to 3 ft-atm which agree with the experimental data of Hottel within 8%. Calculations made at temperatures up to 1750°K for optical depths of 0.1 to 2.0 ft-atm agree with the experimental data within 30%.

It appears that the proposed model for calculating the emissivities of CO_2 constitutes a good approximation at elevated temperatures and that the required parameters have been obtained with fair accuracy from a semi-empirical fit to total emissivity data measured at 300°K. It is apparent that a closer correlation with empirical data could have been obtained if an "optimal adjustment" had been made for the three variable parameters by fitting our theoretical formulae to high-temperature emissivity measurements. However, this "optimal fit" would not constitute as stringent a test of our model as the calculations described in this analysis.

We note that the success of these calculations does not depend upon a fit to Hottel's data at 300°K since (a) we are able to calculate the total emissivity at 300°K with fair accuracy from spectroscopic data and (b) we are able to estimate the parameters required by our model directly from available spectroscopic information. The use of Hottel's data is adopted only as a convenience for this test calculation in order to provide a consistent check on our method of calculating emissivities at elevated temperatures.

Part 2

The f-number for the (0, 0)-band of the $^2\Sigma \rightarrow {}^2\Pi$ transitions of OH has been found to be $(0.9 \pm 0.5) \times 10^{-3}$. A shock tube was used to produce hot gas samples at temperatures from 3300 to 3900°K with equilibrium partial pressures of OH of 0.004 to 0.02 atm. The emission intensities were measured photoelectrically as a function of time behind the reflected shock in a selected spectral interval. These results were then related to the f-number by means of an absolute intensity calibration.

TABLE OF CONTENTS

PART 1

EMISSIVITY CALCULATIONS FOR CO_2

I. INTRODUCTION

In engineering problems involving heat transfer, radiating gases in the infrared spectral region often contribute appreciably. It is therefore of importance to obtain estimates for the required basic parameters in radiative transfer problems. Unfortunately, most gases have been investigated experimentally only at relatively low temperatures.

High temperature measurements of gas emissivities under equilibrium conditions are possible, but the experiments are difficult to perform. Up to about 2000°K, the test gas may be put into a cell placed within a furnace. At higher temperatures, steady-state experiments may be performed in flames and shock tubes. For efficient utilization of available experimental results, it is important to obtain methods by which available emissivity data may be used for extrapolating to new test conditions. With this thought in mind, the following work was undertaken in an attempt to develop useful procedures for CO_2.

For this test case, the data chosen were the direct measurements of total emission by Hottel[1] (see Fig. 1 and Table 1), which were obtained for temperatures up to approximately 2000°K and optical depths up to 2 ft-atm, although both the extremes of temperature and optical depth were not achieved simultaneously. The total pressure was fixed at 1 atm.*

---

* The original emission experiments were performed with CO_2-air mixtures in a cell of length 1.68 ft heated by a furnace to about 1400°K.[2] These results were then extrapolated to 1600°K through use of absorption data. Emission experiments from carbon monoxide flames in a Meker burner[3] provided approximate checks on extrapolations up to about 2300°K.

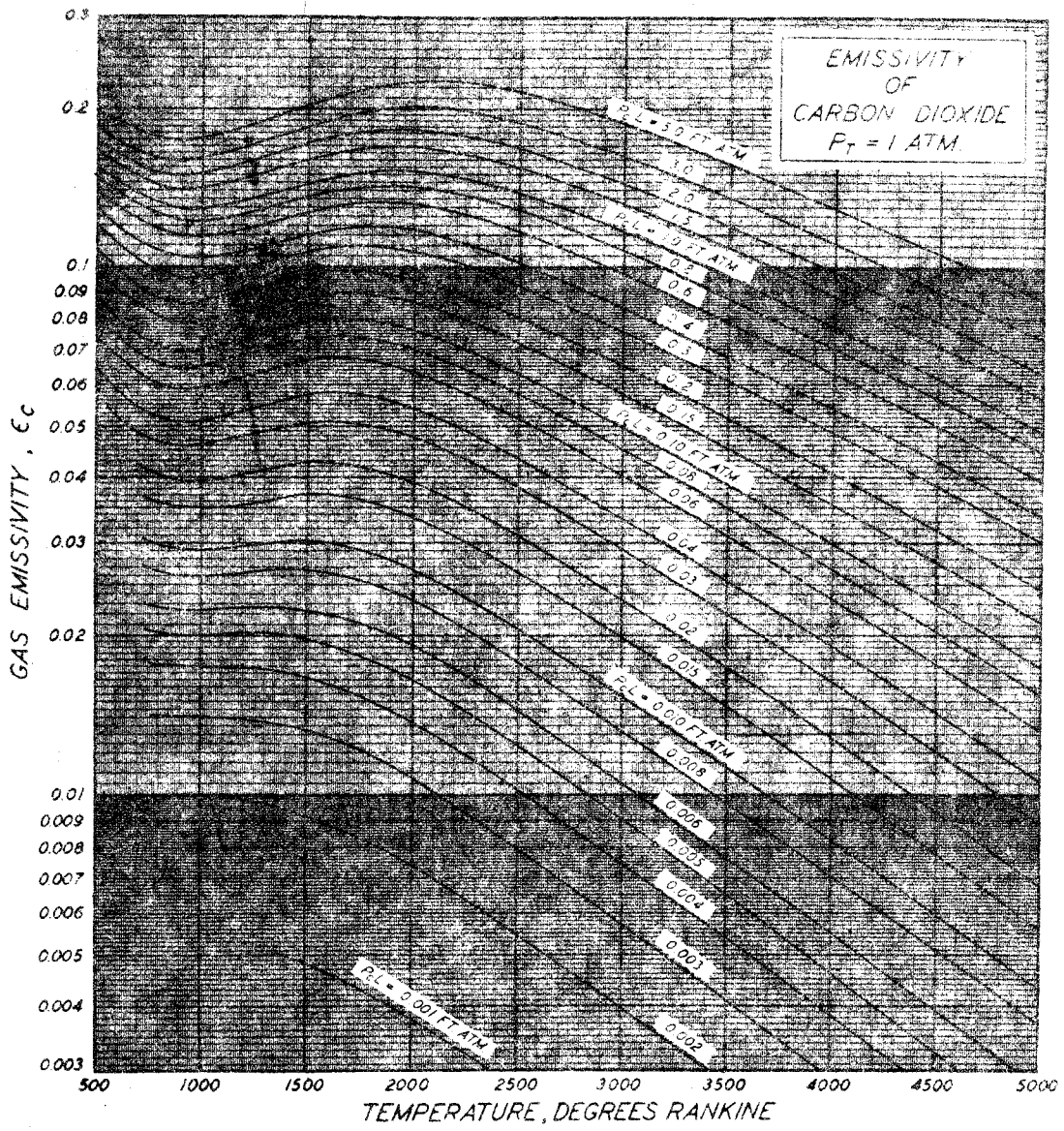

Fig. 1. Emissivities of carbon dioxide as measured by Hottel and collaborators.[1]

(By permission from Heat Transmission, Third Ed., by W. H. McAdams. Copyright, 1954. McGraw-Hill Book Company, Inc.)

Table 1. Emissivities of carbon dioxide at a total pressure p_T of 1 atm, measured by Hottel and collaborators.[1] The data were taken from a greatly enlarged photostat of Fig. 4-13 of Ref. 1.

T / X ft-atm	300°K 540°R	600 1080	900 1620	1200 2160	1500 2700	1750 3150	2000 3600	2500 4500
0.001			.0046*	.00342*				
0.002		.010*	$.0087_7$*	.00675*	.00480*			
0.003		.014*	.0128	.00983	.00696			
0.004		.0174*	.0161	.0126	.00900	.00675	.00502*	
0.005		.0201*	.0192	.0152	.0109	.0082	.00608*	.00327*
0.006		.0225	.0218	.0177	.0127	.00955	.00712*	.00392*
0.008		.0260	$.026_2$	.0217	.0158	.0120	.00910*	.00510*
0.010		.0292	$.029_9$	$.0247_5$	$.0183_5$	.0140	$.0105_5$*	.00598*
0.015		.0350	.037	.0313	.0236	.0182	$.0137_5$	.00778*
0.02		.0397	$.042_6$	.0366	$.0277_5$	.0214	$.0163_5$	.00933*
0.03		.0468	.051	.0449	.0343	.0268	.0207	.0120*
0.04	.062	.0520	.058	.0509	.0390	.0317	.0240	$.0142_4$*
0.06	$.071_5$	.0602	$.067_6$	.0599	.0468	.0371	.0292	.0176*
0.08	.078	.0664	$.074_2$	.0661	.0523	.0417	.0330	$.0201_7$*
0.10	.085	.0710	.080	.0720	.0570	.0460	.0367	$.0229_6$*
0.15	.095	.0808	$.089_5$	.0820	.0658	.0533	.0430	.0275*
0.2	.104	.0877	$.098_4$	.0905	.0740	.0605	.0490	$.0316_5$*
0.3	$.116_5$	.0973	$.108_5$	.103	.0850	.0706	.0581	.0383*
0.4	.125	.105	$.117_5$	.113	.0943	.0783	.0644	.0429*

Table 1, continued

T / X	300°K	600	900	1200	1500	1700	2000	2500
ft-atm	540°R	1080	1620	2160	2700	3150	3600	4500
0.6	.136	.115	.130	.128	.108	.0910	.0750	.0500*
0.8	.144	.123	.139	$.138_5$	$.119_5$	.1007	.0834*	.0560*
1.0	.151	.131	$.147_6$	.149	.130	.110	.0918*	.0614*
1.5	.162	$.143_5$	$.164_5$	.166	.145	.124	$.104_5$*	.0710*
2.0	.170	.153	.177	$.179_5$	.158	.136	$.119_5$*	.0788*
3.0	.180*	.164*	.191*	.203*	$.177_5$*	.153*	.130*	.0900*
5.0	.194*	.178*	.210*	$.226_5$*	$.202_4$*	.177*	.150*	.0106*

* Extrapolated Values.

A. Discussion of Emissivities

The overall emissivity ε of a distributed gas radiator is defined as the ratio of the emitted radiation to the radiation emitted by a blackbody at the same temperature, viz.,

$$\varepsilon = \frac{1}{\sigma T^4} \int_0^\infty R_\omega^o (1 - e^{-P_\omega X}) d\omega \qquad (1)$$

where σ is the Stefan-Boltzmann constant, T is the temperature, R_ω^o is the spectral radiancy of a blackbody at the temperature T, P_ω is the spectral absorption coefficient, X is the optical depth and ω is the wave number. In practice, the range of integration in Eq. (1) is extended over the wave number range in which $P_\omega X$ is sensibly different from zero.

The infrared emissivity covers a wavelength range of $\lambda = 0.7$ to 1000μ, or a wavenumber range of 10 to 14,000 cm^{-1}. The near infrared radiation results from vibration-rotation transitions, while the far infrared (greater than 20μ) is caused by pure rotational transitions.

A vibration-rotation band consists of the group of allowed rotational lines arising with a given vibrational transition. For example, the fundamental bands of a simple diatomic molecule are composed of all the allowed rotational lines accompanying vibrational transitions for which the vibrational quantum number changes by unity.

It is seen that the emissivity depends on the spectral blackbody radiancy function R_ω^o. The radiancy per unit wavenumber is a maximum at the wavenumber $\omega_{max} = 1.965\,T\ cm^{-1}$ with T expressed in degrees Kelvin; the radiancy per unit wavelength is a maximum at $\lambda_{max} = (2898/T)\mu$.

For the temperature range under consideration (300°K to 1750°K), the infrared emissivity may generally be computed by considering the vibration-rotation bands as the important contributors. In particular, CO_2 has no pure rotational spectrum since it has no permanent dipole moment.

In Fig. 2 we have plotted the normalized blackbody function $\rho_\omega = R^o_\omega / R^o_{\omega_{max}}$ vs. ω at 300, 600, and 1500°K. In Figs. 3 to 5, we have replotted these functions in greater detail and have also indicated the positions of the centers of the important vibration-rotation bands of CO_2. The notation vs, m, w, etc., refers to a rough indication of the band integrated intensity as very strong, medium, weak, etc.

It may be seen from Eq. (1) that the blackbody function exerts a relatively larger influence on the emissivity as the optical depth X is increased; for large X, the importance of P_ω decreases as X increases. On the other hand, in the limit of very small optical depth, we may expand the exponential and obtain

$$\varepsilon \simeq \frac{X}{\sigma T^4} \int_{\Delta\omega} R^o_\omega P_\omega \, d\omega \qquad (2)$$

as $X \rightarrow 0$, which indicates that the strength of the transition, as indicated by P_ω, becomes as important as the blackbody function. Whenever the product $P_\omega X$ is sufficiently small to warrant the use of Eq. (2), we consider the gas to be "transparent" or in "the linear part of the curves of growth", i.e., self-absorption may be neglected. In all cases, the integral of the spectral absorption coefficient over a band for a fixed number of absorbers is independent of the optical depth, and is known as the integrated intensity, a.

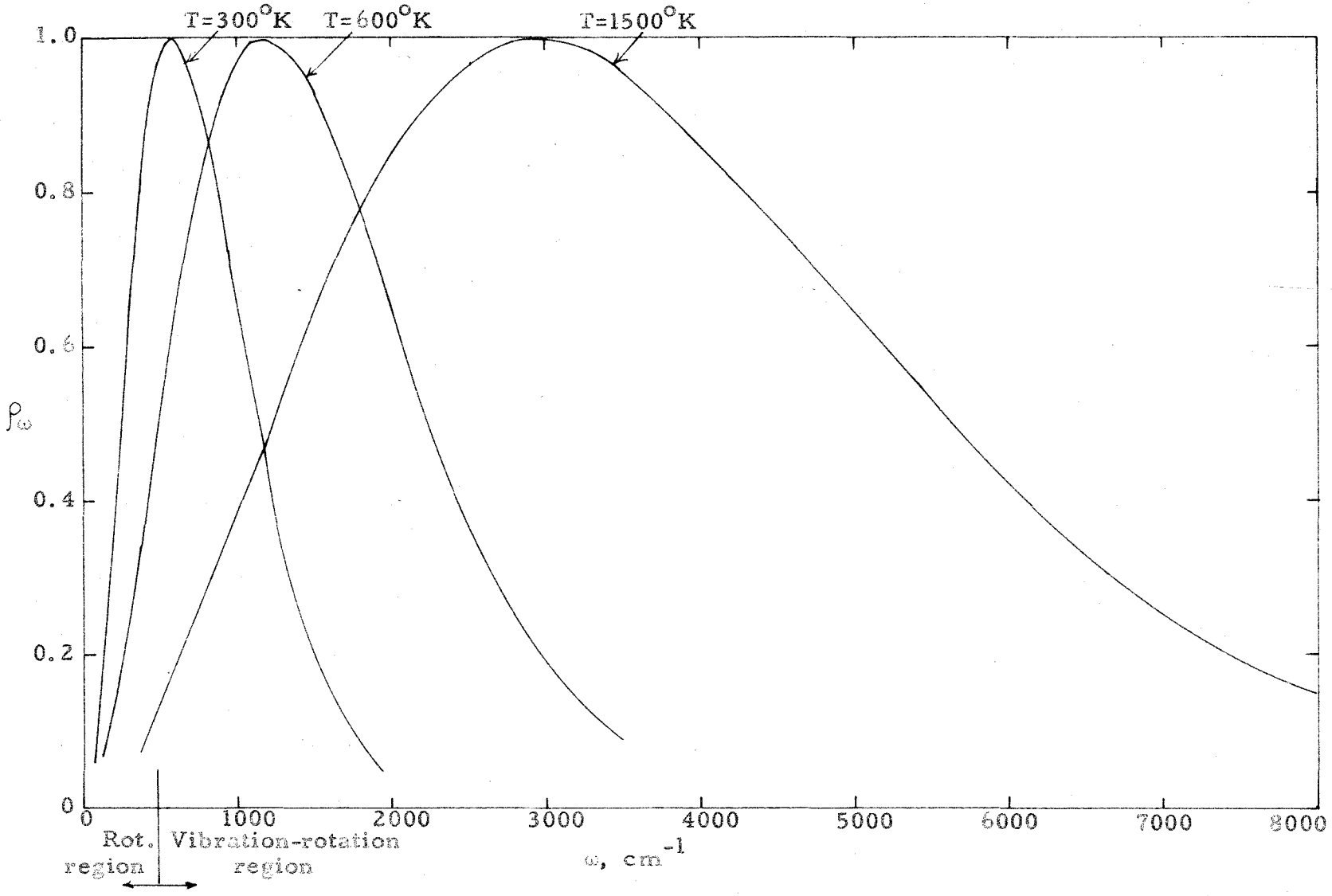

Fig. 2. Variation of the normalized blackbody function with wavenumber at 300, 600 and 1500°K

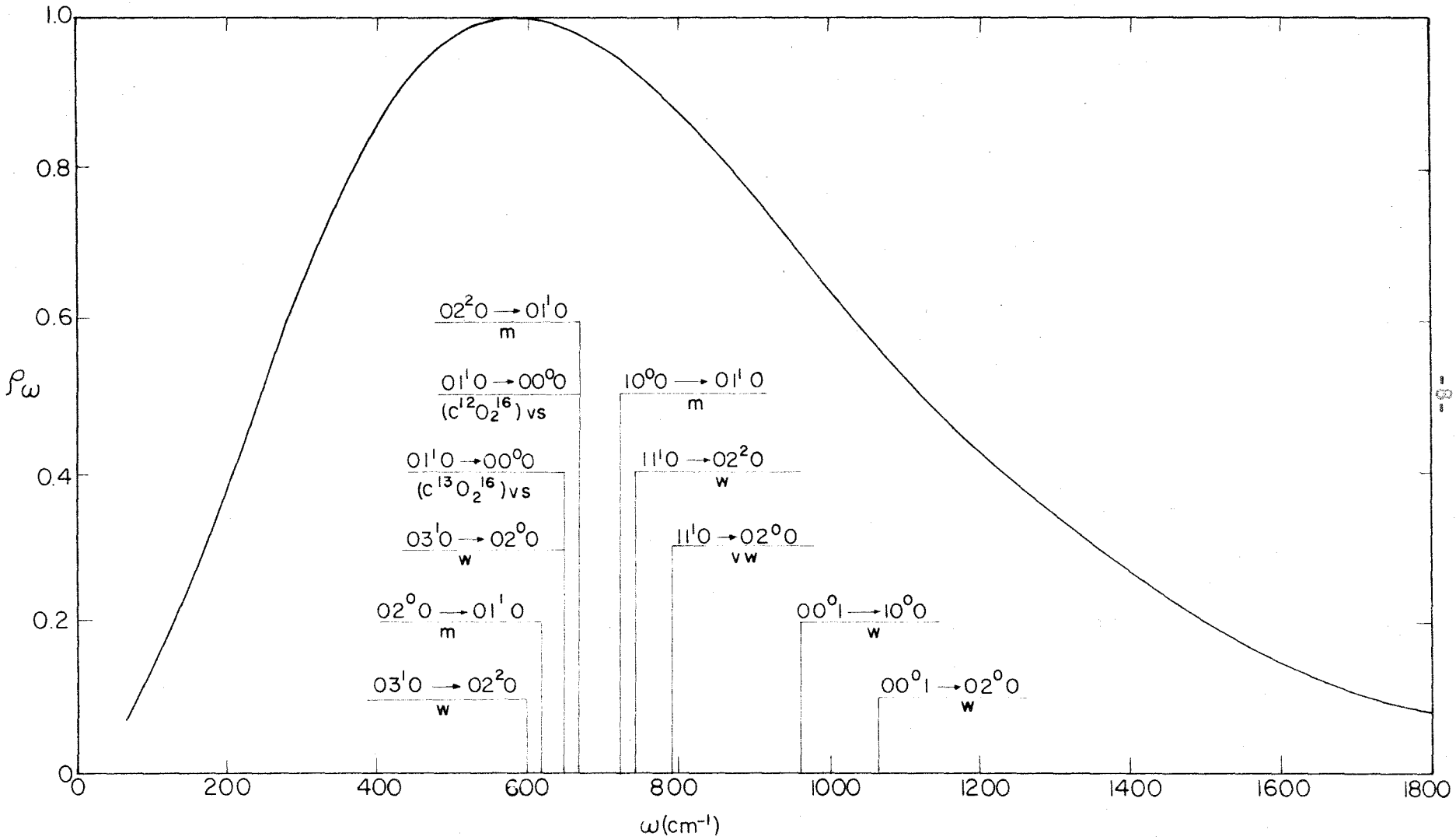

Fig. 3. The normalized blackbody function at 300°K. The positions of the centers of the important vibration-rotation bands of CO_2 are indicated. (The heights of the lines indicating these centers are arbitrary.) Explanation of the notation for the transitions appears on p. 20.

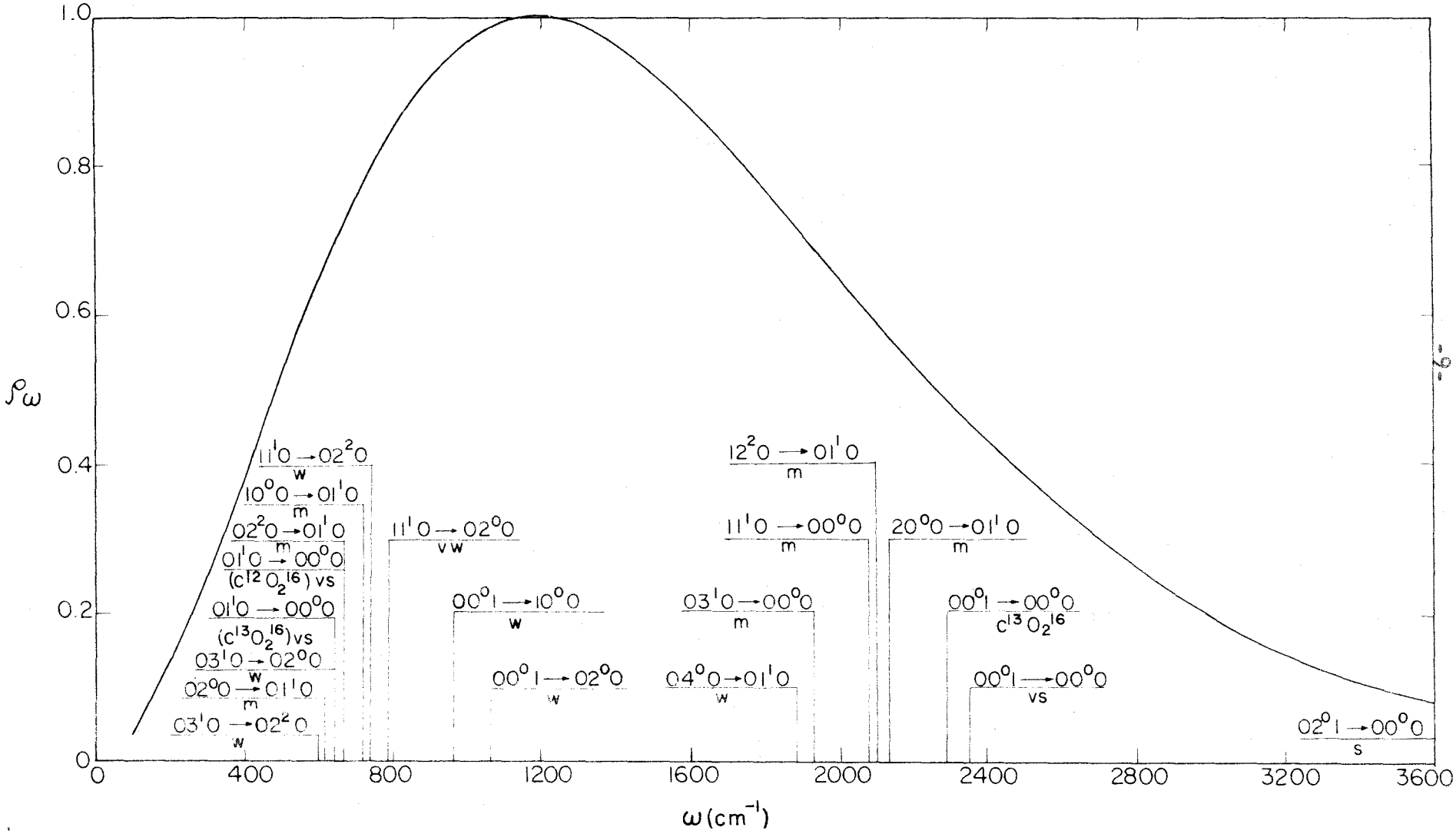

Fig. 4. The normalized blackbody function at 600°K. The positions of the centers of the important vibration-rotation bands of CO_2 are indicated. (The heights of the lines indicating these centers are arbitrary.) Explanation of the notation for the transitions appears on p. 20.

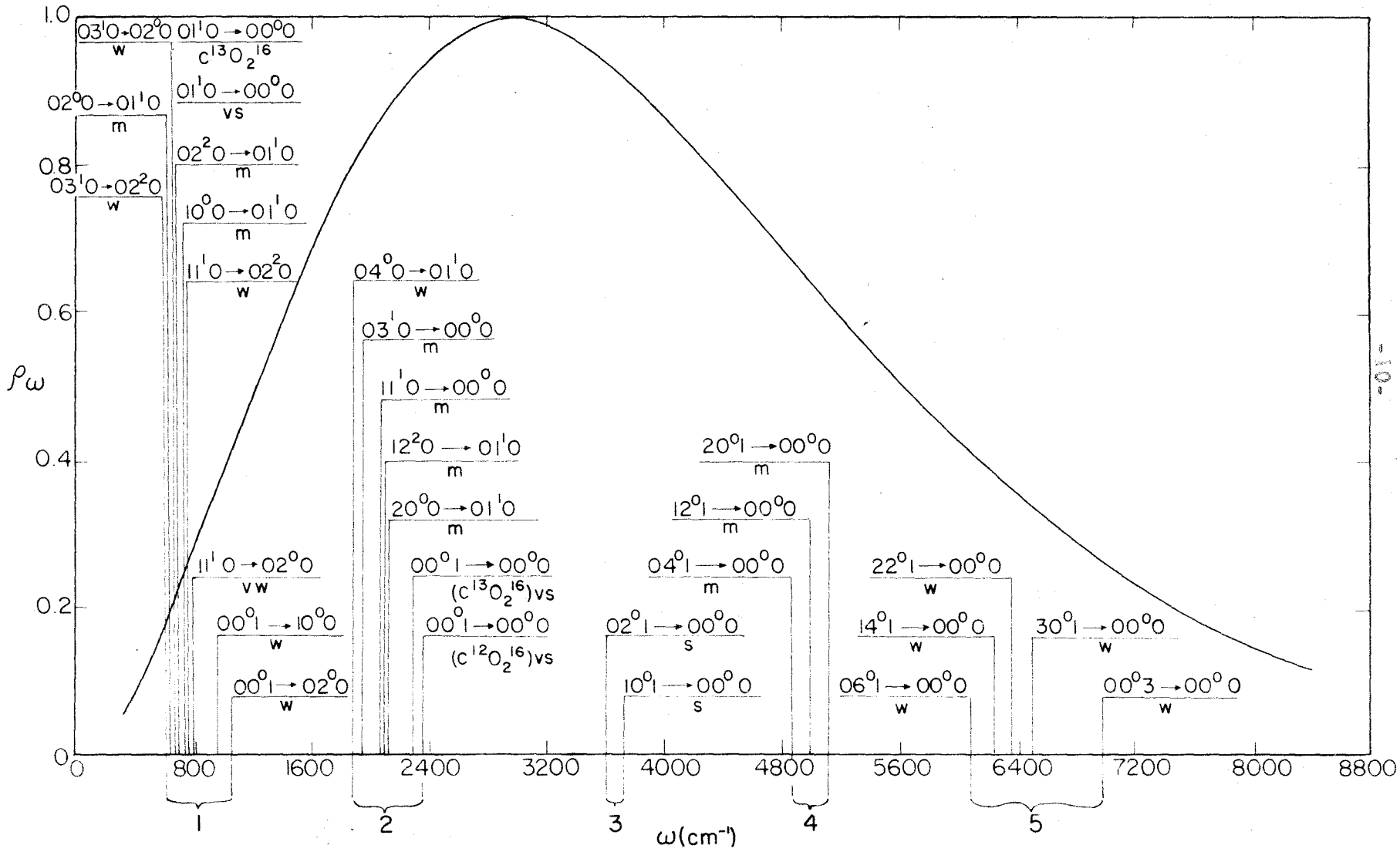

Fig. 5. The normalized blackbody function at 1500°K. The positions of the centers of the important vibration-rotation bands of CO_2 are indicated. (The heights of the lines indicating these centers are arbitrary.) Explanation of the notation for the transitions appears on p. 20.

B. Infrared Spectrum of CO_2

The complete calculation of the infrared emissivity of a polyatomic molecule at elevated temperatures involves (a) extrapolation to higher temperatures of data known from room temperature measurements, (b) theoretical predictions or assumptions concerning the variations of spectral profiles with temperature, and (c) introduction of new bands which were not observed in room temperature studies but which may be presumed to be present in order to account for observed emissivity data at elevated temperatures. The strengths of overtone and combination bands are generally not known sufficiently well to permit their explicit inclusion in emissivity calculations.

As an example of the problem, consider the emissivity of CO_2 at $1200^{\circ}K$, at which temperature the blackbody peak lies at the center of the ν_3-fundamental which is the most intense transition of CO_2. Computations indicate that the fraction of the total measured emissivity accounted for by the ν_3-fundamental and the surrounding relatively weak bands varies from two-thirds to one-third for $0.033 \leq X \leq 3.3$ ft-atm. The remainder of the emissivity is not easily accounted for by the other known bands, leading to the conclusion that either more information on the CO_2 spectrum is needed before detailed calculations of the total infrared emissivity at elevated temperatures should be attempted, or else that assumptions regarding the nature of the spectrum at elevated temperatures must be made.

Inspection of Herzberg's listing[4] of CO_2 bands indicates that they fall, in general, into four important spectral groupings. The first

contains eleven bands, including the intense ν_2-fundamental. The centers of the first nine of the bands range from 596.8 cm^{-1} to 790.8 cm^{-1}, with the last two weak bands extending the region to 1063.6 cm^{-1}. The second region, containing seven bands and including the intense ν_3-fundamental, extends from 1886 cm^{-1} to 2349.3 cm^{-1}. The third region consists of the two strong bands at 3609 and 3716 cm^{-1}, while the fourth consists of the three bands of medium strength between 4860.5 cm^{-1} and 5109 cm^{-1}. Five weak bands, extending from 6077 cm^{-1} to 6979 cm^{-1} are also listed. The following calculations show that only the first three regions are of significant importance.

C. Emissivity Calculations at 300°K

Three different approximations may be used as models for the calculation of the emissivity of CO_2 at 300°K. In the non-overlapping line model, the contributions of individual lines are added. For small optical depths or at very low pressures, this procedure is accurate; at moderate optical depths, overlapping causes the sum of the separate contributions to be very much larger than the emissivity. In the just-overlapping line approximation each line is represented by an average value that is determined by dividing the integrated intensity of the line by the mean spacing between adjacent lines. Since the spectral line profile is not used in this description, pressure-induced line broadening effects on the emissivity have been neglected. This is not a serious shortcoming for optical depths with moderate overlapping, since the decrease in the absorption coefficient near the line centers produced by pressure broadening and the increase in absorption coefficients produced by the

tails of adjacent lines tend to compensate. A third representation is the box approximation, wherein the entire vibration-rotation band profile is replaced by an average absorption coefficient localized within an effective band width.

The results obtained from these calculations are plotted in Fig. 6. The dominant contribution to the emissivity arises from the ν_2-fundamental at 667 cm^{-1}. It is seen that the just-overlapping line approximation affords the best fit at room temperature. Below X = 0.02 ft-atm, all of the models give the same result, since they all reduce to the expression for a transparent gas.

II. SPECTRAL STRUCTURE OF THE INFRARED BANDS

A. Statistical Model for Randomly Distributed Vibration-Rotation Bands

For calculations at elevated temperatures, we attempt to account for the overlapping between adjacent bands by calculating the emissivity on the basis of a model that does not depend on the extent of overlapping. We describe a given spectral region by considering the bands (except for the fundamentals) to be randomly distributed with respect to intensity and position. The fundamentals are treated separately, since they are far more intense than the remaining bands at the temperatures and pressures that we consider. Furthermore, their positions and intensities are reasonably well known.*

* Preliminary calculations were made considering all bands randomly distributed but, in order to achieve reasonable results, it was found necessary to separate the contributions of the ν_2- and ν_3-fundamentals to the effective absorption coefficient from the contributions of the remaining bands.

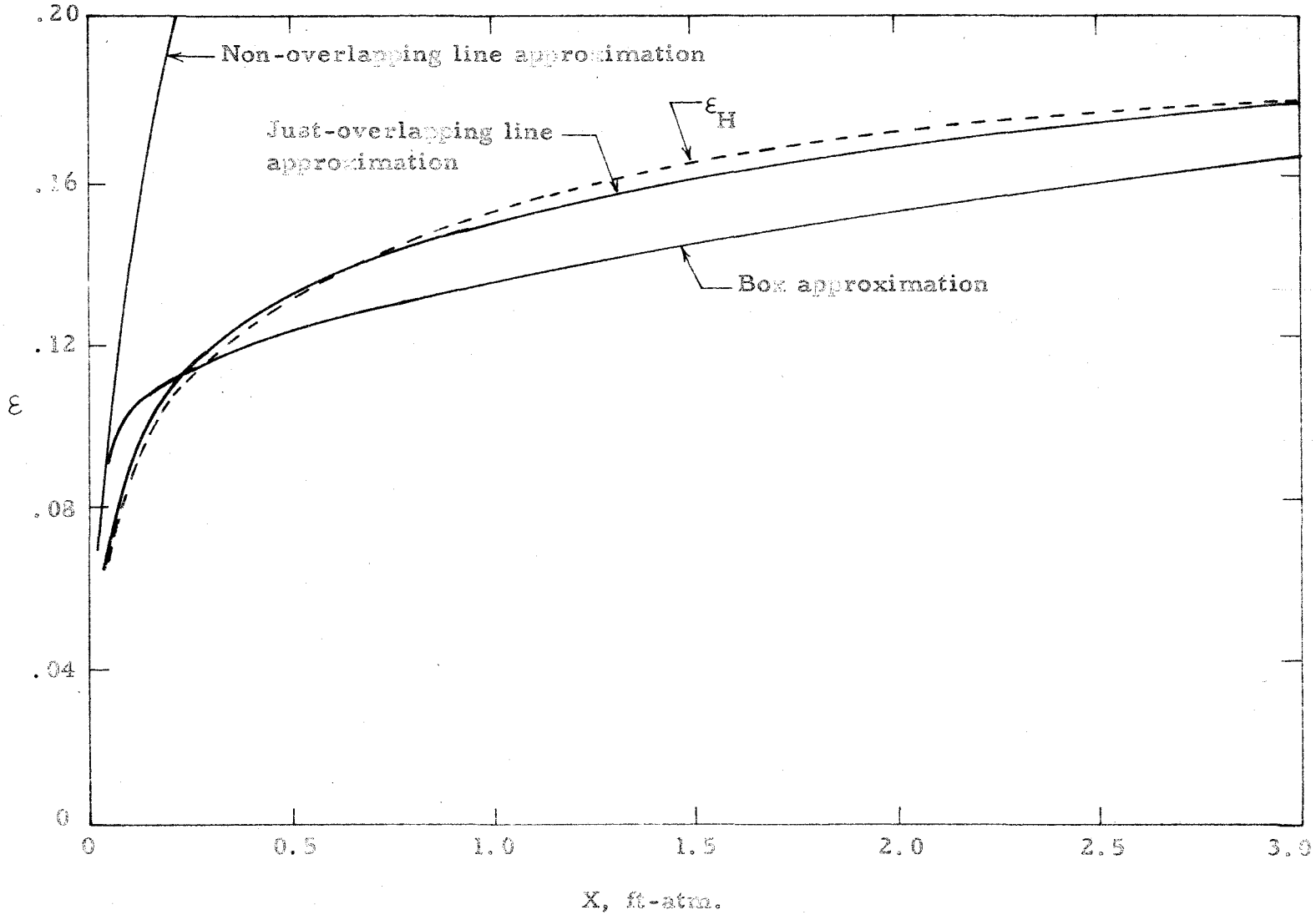

Fig. 6. Emissivity calculations for carbon dioxide at 300°K, compared with the experimentally determined values ε_H of Hottel.[1]

The statistical model was developed independently by Mayer[5] and Goody[6], and has been applied to randomly distributed vibration-rotation bands for purely Doppler-broadened lines.[7] In statistical calculations we may describe the band shape by considering the lines to be non-overlapping, just-overlapping, or well-overlapping (box model).

In the statistical approach an expression may be derived readily for $\bar{\varepsilon}(\omega)$, the mean spectral emissivity. In order to obtain the total emissivity (ε_j) for the jth region of the spectrum, we use average blackbody radiancies ($R^o_{\omega_j}$) and effective band widths ($\Delta\omega_j$) and define ε_j as

$$\varepsilon_j = \frac{R^o_{\omega_j}}{\sigma T^4} \bar{\varepsilon}_j(\bar{\omega}_j)\Delta\omega_j \ . \tag{3}$$

A criterion for the choice of $R^o_{\omega_j}$ will be described in Section IIIA.

We consider the spectral transmission $T(\omega)$ at the center of a region consisting of N bands whose mean spacing is given by δ. The width of the region is thus approximately given by $N\delta$. In effect, this statement assumes that the effective width of a band* is of the same order of magnitude as the mean band spacing for N sufficiently large.

Consider the region to be centered at ω, with no contributions to the transmission at ω coming from bands outside the interval $\omega \pm \frac{N\delta}{2}$. We assume no correlation between the band positions and intensities, except for the intense ν_2- and ν_3-fundamentals. The following derivation

---

* If we compute the effective band width $\Delta\omega_B$ by using $J \exp\left[-E(n, J)/kT\right]$ as the dominant rotational factor, we obtain $\Delta\omega_B$ = constant x $\sqrt{T}$ (see Ref. 7, p. 264). Here J is the rotational quantum number. For CO_2, we have $\Delta\omega_B = 6.20\sqrt{T} = 108$ cm^{-1} at 300°K.

of Eq. (7) is similar to that presented on pp. 317 to 318 of Ref. 7.

We define $\mathcal{P}(\bar{a}, a)da$ as the probability that a band has an integrated intensity between a and a + da and $N_o\, d\omega_1$, $d\omega_2$, ... $d\omega_N$ as the probability that a group of bands occurs in the wave number interval $d\omega_1$, $d\omega_2$, ... $d\omega_N$, where N_o is a constant. Then the probability of having N bands in $d\omega_1$, $d\omega_2$ ... $d\omega_N$, with the ith band intensity between a_i and $a_i + da_i$ is $N_o \prod_{i=1}^{N} \mathcal{P}(\bar{a}, a_i)da_i\, d\omega_i$. Let the absorption coefficient of the ith band be given by $(P_\omega)_i$. The fractional transmission of the ith band through an optical path X at the wave number ω is $T_i(\omega) = \exp\left[-(P_\omega)_i X\right]$ for the ith band at ω_i with an integrated intensity a_i. The spectral emissivity at ω is $\mathcal{E}(\omega) = 1 - T(\omega) = 1 - \prod_{i=1}^{N} \exp\left[-(P_\omega)_i X\right]$. Averaging this expression over all possible band positions and intensities, we may write

$$\bar{\mathcal{E}}(\omega) = \frac{1}{N_o(N\delta)^N} \int_{-N\delta/2}^{N\delta/2} \cdots \int_{-N\delta/2}^{N\delta/2} N_o \int_0^\infty \cdots \int_0^\infty \prod_{i=1}^{N} \mathcal{P}(\bar{a}, a_i)\, \mathcal{E}(\omega)da_i\, d\omega_i ,$$

where the jth wave number range extends from $\omega_j = \omega - N\delta/2$ to $\omega + N\delta/2$. Using the explicit relation for $\mathcal{E}(\omega)$ given previously, we find that

$$\bar{\mathcal{E}}(\omega) = \frac{1}{N_o(N\delta)^N} \int_{-N\delta/2}^{N\delta/2} \cdots \int_{-N\delta/2}^{N\delta/2} \int_0^\infty \cdots \int_0^\infty \prod_{i=1}^{N} \mathcal{P}(\bar{a}, a_i) \left[1 - \prod_{i=1}^{N} e^{-(P_\omega)_i X}\right]$$

$$\times\, da_i\, d\omega_i$$

$$= 1 - \frac{1}{(N\delta)^N} \int_{-N\delta/2}^{N\delta/2} \cdots \int_{-N\delta/2}^{N\delta/2} \int_0^\infty \cdots \int_0^\infty \prod_{i=1}^{N} \mathcal{P}(\bar{a}, a_i) e^{-(P_\omega)_i X} \, da_i d\omega_i, \quad (4)$$

or

$$\bar{\varepsilon}(\omega) = 1 - \left\{ \frac{1}{N\delta} \int_{-N\delta/2}^{N\delta/2} \int_0^\infty \mathcal{P}(\bar{a}, a) e^{-P_{\omega'} X} \, da \, d\omega' \right\}^N$$

$$= 1 - \left\{ 1 - \frac{1}{N\delta} \int_{-N\delta/2}^{N\delta/2} \int_0^\infty \mathcal{P}(\bar{a}, a) \left[1 - e^{-P_\omega X} \right] da \, d\omega' \right\}^N . \quad (5)$$

Since we have constructed the integrand so that it vanishes outside of the range of integration $|\omega - \omega'| > N\delta/2$, we may replace $\pm N\delta/2$ by $\pm \infty$ and obtain

$$\bar{\varepsilon}(\omega) = 1 - \left\{ 1 - \frac{1}{N\delta} \int_{-\infty}^{\infty} \int_0^\infty \mathcal{P}(\bar{a}, a) \left[1 - e^{-P_{\omega'} X} \right] da \, d\omega' \right\}^N . \quad (6)$$

For N sufficiently large, the preceding relation may be approximated by

$$\bar{\varepsilon}(\omega) = 1 - \exp \left\{ -\frac{1}{\delta} \int_{-\infty}^{\infty} \int_0^\infty \mathcal{P}(\bar{a}, a) \left[1 - e^{-P_{\omega'} X} \right] da \, d\omega' \right\} . \quad (7)$$

We define the band absorption (or "equivalent width") as

$$A(a) = \int_{-\infty}^{\infty} \left[1-e^{-P_{\omega'}X}\right] d\omega' \tag{8}$$

(and its weighted mean value as

$$\bar{A} = \int_{0}^{\infty} \mathcal{P}(\bar{a}, a)\, A(a)\, da\ . \tag{8a}$$

In terms of $\bar{A}$, the mean spectral emissivity for the selected wave number interval becomes now

$$\bar{\varepsilon}(\omega) = 1-e^{-\bar{A}/\delta}\ . \tag{9}$$

The intensity probability distribution function for region 1 containing N_1 bands and the ν_2-fundamental at 667 cm^{-1} with integrated intensity a_{667} is defined as

$$\mathcal{P}_1 = \frac{1}{N_1}\left[\delta(a_{667}-a) + (N_1-1)\,\delta(\bar{a}_1{}^*-a)\right].$$

Here $\bar{a}_1{}^* = a_1{}^*/(N_1-1)$; $a_1{}^*$ represents the sum of the integrated intensities of all the bands other than that of the ν_2-fundamental in region 1; also

$$\delta(a'-a) = 0 \quad \text{for } a \neq a',$$

$$\int_{-\infty}^{\infty} \delta(a'-a)da = 1.$$

In terms of the distribution function $\mathcal{P}_1$, it follows that

$$\bar{A}_1 = \int_{0}^{\infty} \mathcal{P}_1 A(a)da = \frac{1}{N_1}\left[A_{667} + (N_1-1)\,\bar{A}_1{}^*\right]$$

---

* The choice of intensity probability distribution function for the weak bands does not influence significantly the computed emissivity, as has been previously noted by Goody[6] for randomly distributed H_2O lines.

where

$$A_{667} = \int_{-\infty}^{\infty} (1-e^{-P^{o}_{\omega'}X})d\omega'$$

and

$$(N_1-1)\bar{A}_1^* = A_1^* = \int_{-\infty}^{\infty} (1-e^{-P^{*}_{\omega'}X})d\omega' \ ;$$

$P^{*}_{\omega'}$ is the spectral absorption coefficient in region 1 produced by all of the bands other than the ν_2-fundamental, while $P^{o}_{\omega'}$ represents the absorption coefficient of the fundamental. For region 1 we now have the relation

$$\varepsilon_1 = \frac{R^{o}_{\omega_1}}{\sigma T^4} \left\{ 1-\exp\left\{ -\frac{1}{\Delta\omega_1}\left[A_{667} + (N_1-1)\bar{A}_1^* \right] \right\} \right\} \Delta\omega_1 \qquad (10)$$

where $N_1 = \Delta\omega_1/\delta_1$.

B. Rotational Band Structure

Thus far we have chosen a random distribution of bands but have not yet specified the model to be used for the description of the rotational structure of the bands. As a reasonable model, we assume the rotational lines to be "just-overlapping", which requires that the absorption coefficient for the Jth line be represented by the average value across the line: $\bar{P}_J = S_J/\delta'$ where S_J is the integrated intensity of the Jth line and δ' is the line spacing, viz., $\delta' \simeq 4B_e$ for large J for CO_2.

For a linear triatomic molecule,*

* Ref. 7, Chapt. 7.

$$\frac{S(n_1 n_2^{\ell} n_3;\ J \rightarrow n_1' n_2'^{\ell'} n_3';J')}{\sum_{\ell'} a(n_1 n_2^{\ell} n_3 \rightarrow n_1' n_2'^{\ell'} n_3')} =$$

$$\frac{\omega(n_1 n_2^{\ell} n_3;J \rightarrow n_1' n_2'^{\ell'} n_3';J')}{\omega^* Q_R} \frac{g_{J'\ell'}}{g_{\ell}} \left| \mathcal{A}_{J\ell}^{J'\ell'} \right|^2 e^{-W_R(J)/kT} \qquad (11)$$

where n_1, n_2, and n_3 are the vibrational quantum numbers corresponding to the three fundamental vibrational frequencies ν_1, ν_2 and ν_3 and ℓ is the quantum number which indicates the angular momentum about the symmetry axis of the bending mode. The rotational transition is identified by the symbol $n_1 n_2^{\ell} n_3;J \rightarrow n_1' n_2'^{\ell'} n_3';J'$; the initial state quantum numbers are unprimed while the final state numbers are primed; ω^* is the wave number for the $J=0 \rightarrow J'=0$ transition; $g_{J'\ell'}$ is the statistical weight of the upper state and is given by $2J'+1$ for $\ell'=0$ or $2(2J'+1)$ for $\ell' \neq 0$; g_{ℓ} is the statistical weight of the lower state and is equal to 1 for $\ell=0$ or 2 for $\ell \neq 0$; $\left| \mathcal{A}_{J\ell}^{J'\ell'} \right|^2$ represents the rotational amplitude for the transition $J\ell \longrightarrow J'\ell'$; $W_R(J)$ is the rotational energy for quantum number J; $Q_R = \sum_J g_J \exp\left[-W_R(J)/kT\right]$ is the rotational partition function.

Consider, for example, the rotational transitions in the ν_3-fundamental of CO_2: $00^00;\ J' \longrightarrow 00^01;\ J$. This is a parallel band, with $\ell=0$ in both the initial and final states. Only the transitions $\Delta J = \pm 1$ are allowed giving P($\Delta J=-1$) and R ($\Delta J=1$) branches. Neglecting vibration-rotation interactions,*

---

* Ref. 7, pg. 152.

$$\left|\mathcal{A}^{J\ \ \ell}_{J-1\ \ \ell}\right|^2 = \frac{J^2-\ell^2}{J(2J+1)} \quad \text{and} \quad \left|\mathcal{A}^{J-1\ \ \ell}_{J\ \ \ell}\right|^2 = \frac{J^2-\ell^2}{J(2J-1)},$$

whence

$$\left|\mathcal{A}^{J\ \ 0}_{J-1\ \ 0}\right| = \frac{J}{2J+1} \qquad \text{and} \qquad \left|\mathcal{A}^{J-1\ \ 0}_{J\ \ 0}\right|^2 = \frac{J}{2J-1} .$$

Also $W_R(J) = (hcB_e/kT)\, J(J+1)$ and $\omega(J \rightarrow J-1) = \left[W_R(J) - W_R(J-1) + \Delta W_V\right]/hc$ $= 2B_eJ + \Delta W_V/hc$, where ΔW_V is the change in vibrational energy corresponding to the transition under consideration. Similarly, $\omega(J-1 \rightarrow J) = -2B_eJ + \Delta W_V/hc$. Through use of the relations $\omega^* = \Delta W_V/hc$ and $Q_R \simeq kT/2hcB_e$, we finally obtain

$$S(J-1 \rightarrow J) \simeq \frac{a_{2349}}{\omega^* Q_R}\,(\omega^* - 2B_eJ)\, J\, e^{-hcB_eJ(J-1)/kT} \tag{12}$$

and

$$S(J \rightarrow J-1) \simeq \frac{a_{2349}}{\omega^* Q_R}\,(\omega^* + 2B_eJ)\, J\, e^{-hcB_eJ(J+1)/kT} . \tag{13}$$

Since $\omega^* \gg 2B_eJ$ and since we consider, in general a large number of lines, we may use the approximation

$$S(J-1 \rightarrow J) \simeq S(J \rightarrow J-1) \simeq \frac{2ahcB_e}{kT}\, J\, e^{-hcB_eJ^2/kT} \tag{14}$$

which assumes equally intense branches for the bands. The average absorption coefficient for the just-overlapping line model is therefore

$$\overline{P}_\omega = \frac{ahc}{2kT}\, J\, e^{-hcB_eJ^2/kT} . \tag{15}$$

If we let $\gamma = hcB_e/kT$ and $\xi = \sqrt{\gamma}\, J$, we obtain

$$\overline{P}_{\omega} = \frac{a\sqrt{\gamma}}{2B_e}\, \xi e^{-\xi^2} . \qquad (16)$$

Since $\omega = \omega^* \pm 2B_e J = \omega^* \pm 2B_e \xi/\sqrt{\gamma}$, $d\omega = \pm (2B_e/\sqrt{\gamma})d\xi$. From Eq. (8) it follows now that the band absorption is given by

$$A(a) = \frac{4B_e}{\sqrt{\gamma}} \int_0^{\infty} \left[1-\exp\left(-\frac{aX\sqrt{\gamma}}{2B_e}\, \xi e^{-\xi^2}\right)\right] d\xi . \qquad (17)$$

If we let $K = aX\sqrt{\gamma}/2B_e$ and $I(K) = \int_0^{\infty} \left[1-\exp(-K\xi e^{-\xi^2})\right] d\xi$, Eq. (17) reduces to $A = (4B_e/\sqrt{\gamma})\, I(K)$. Values of the integral I(K) for K up to 120 have been obtained numerically through use of a digital computer.* For small K, which corresponds to the transparent gas regime, $I \simeq K/2$ (good to 2% for K = 0.05); in the other extreme, $\lim_{K\to\infty} I = \sqrt{\ln CK/2}$, where C is Euler's Constant. This expression may be found by utilizing an approximate analytic solution to the integral.**

In order to extend the computed I(K) vs. K curve for large values of K, an extrapolation was performed with the requirement that I(K) is of the form

$$(\text{constant}) \times \sqrt{\ln (\text{constant} \times K)} .$$

This expression was fitted to the I(K) vs. K curve for values of K close to the upper limit of calculation and resulted in the expression $I \simeq 1.11 \sqrt{\ln(1.21K)}$. Curves of I vs. K for the range of K used in the present calculations appear in Figs. 7 to 9.

---

* Ref. 7, pg. 279.

** Ref. 7, pg. 330.

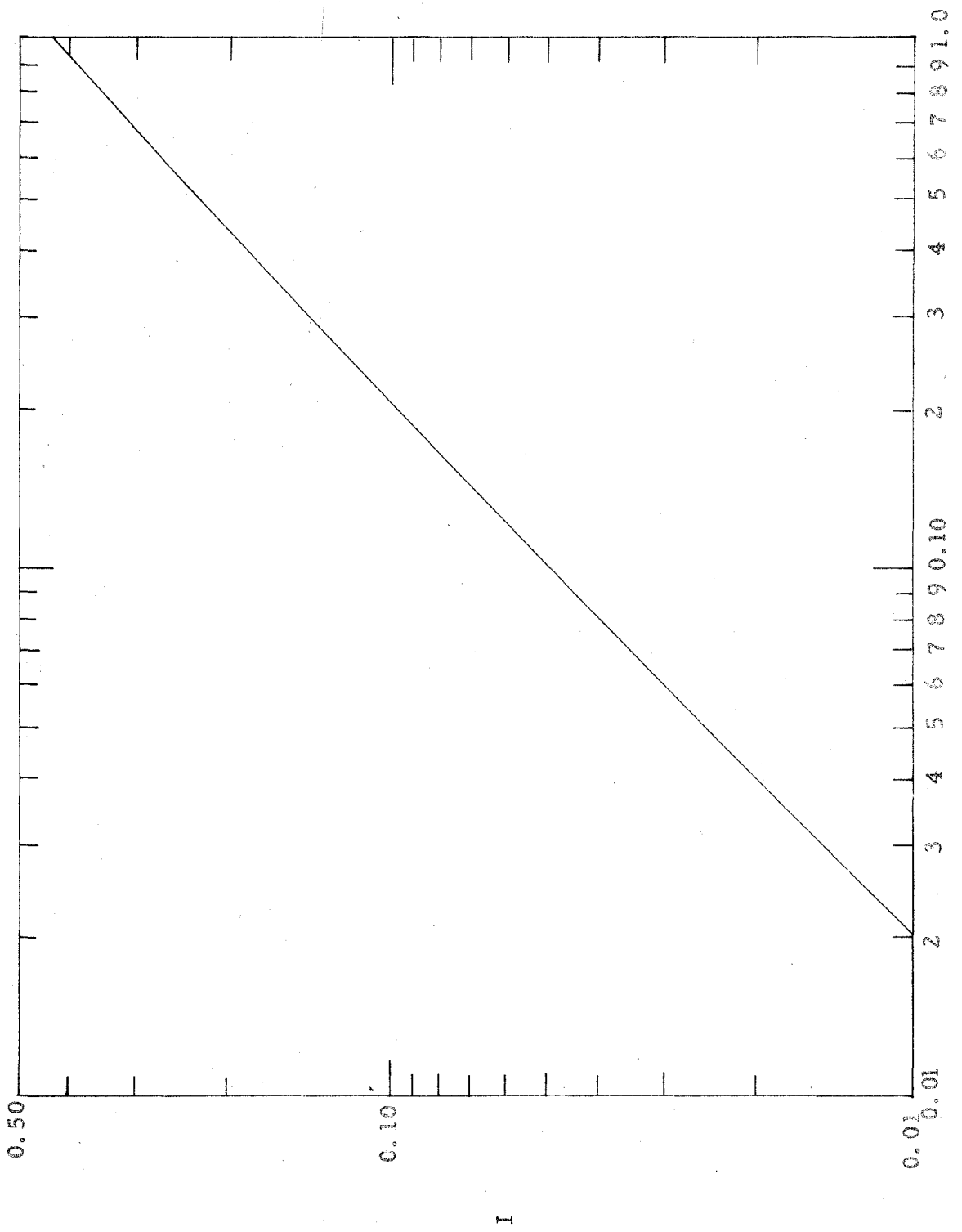

Fig. 7. I(K) vs. K, for use in the (not-overlapping) line model calculations of band absorption.

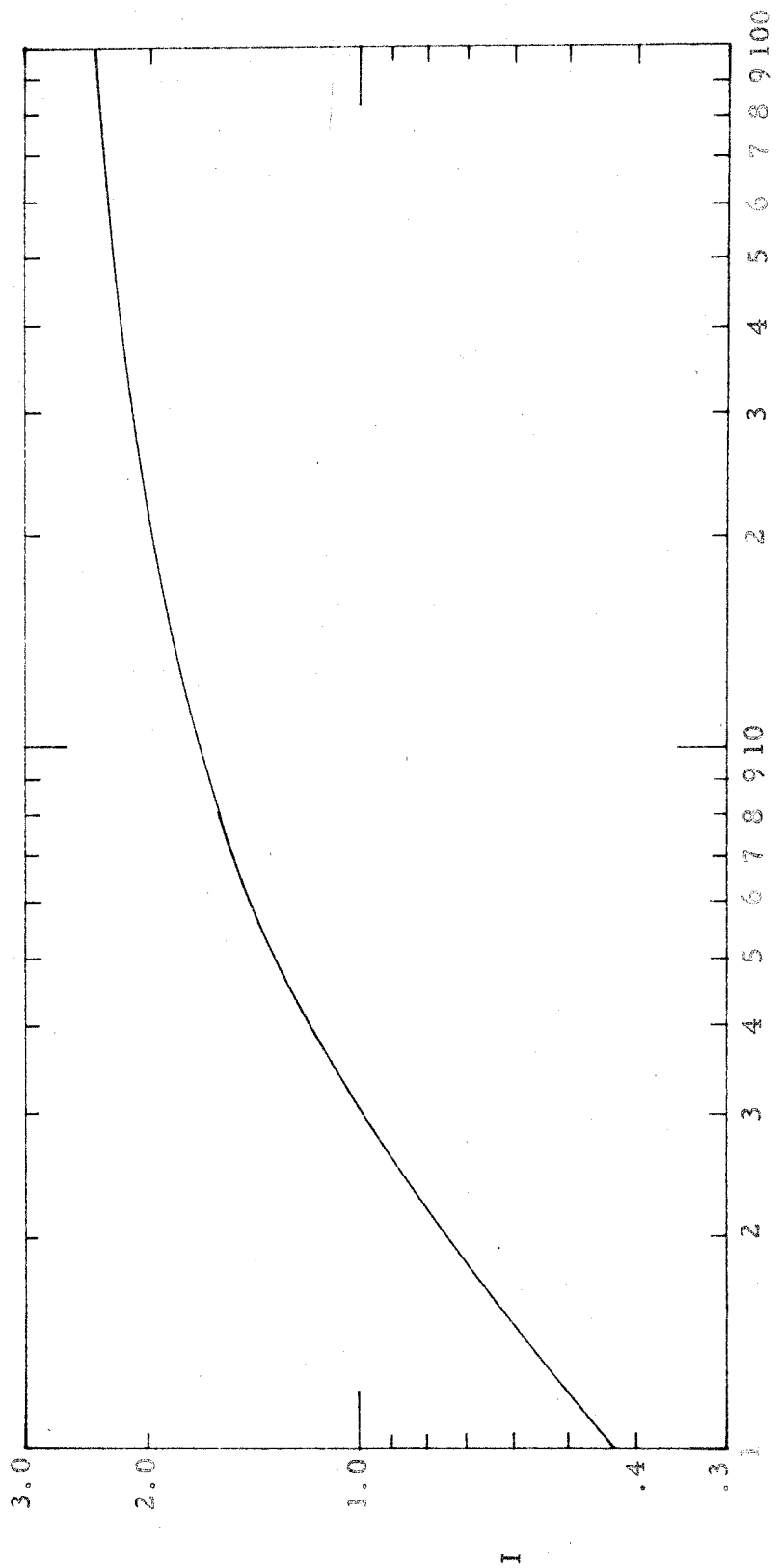

Fig. 8. I(K) vs. K, for use in the just-overlapping line model calculations of band absorption.

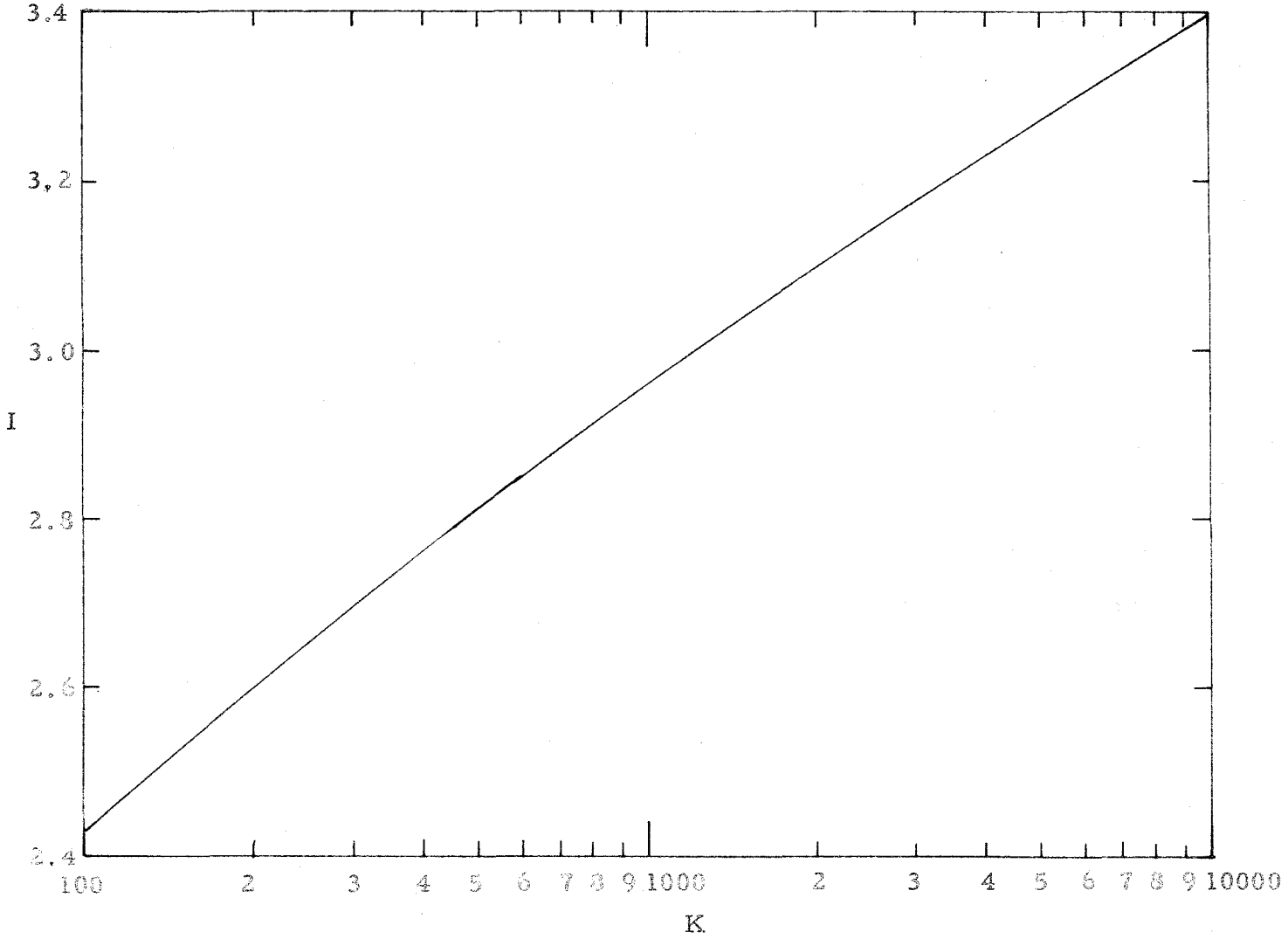

Fig. 9. I(K) vs. K, for use in the just-overlapping line model calculations of band absorption.

We may now write the expression for the emissivity of the jth region as follows:

$$\varepsilon_j = \frac{0.3148}{T} \rho_j (1 - e^{-\bar{g}_j}) \Delta\omega_j \tag{18}$$

where, for region 1,

$$\bar{g}_1 = \frac{4B_e}{\sqrt{\gamma}\,\Delta\omega_1} \left[I(K_{667}) + \left(\frac{\Delta\omega_1}{\delta_1} - 1 \right) I(K_1^*) \right], \tag{19}$$

K_{667} = K for $a = a_{667}$,

K_1^* = K for $a = \bar{a}_1^*$,

$\rho_1 = R^o_{\omega_1} / R^o_{\omega_{max}}$, $(0 < \rho \leq 1)$

and also

$$R^o_{\omega_{max}} / \sigma T^4 = 0.3148/T.$$

The expression for the total emissivity is therefore

$$\varepsilon = \sum_j \varepsilon_j \tag{18a}$$

where ε_j is given by Eq. (18) for all regions whose emissivities are calculated by use of the statistical model.

We have now obtained a relation for the emissivity that requires the determination, for each spectral region, of (a) the normalized blackbody function (ρ_j), (b) a quantity which represents an average absorption coefficient multiplied by the optical depth ($\bar{g}_j$), and (c) the effective region width ($\Delta\omega_j$). Assuming that the required integrated

intensities are known, $\bar{g}_j$ is a function of $\Delta\omega_j$ and the mean band spacing δ_j. Thus we have three unknowns for each region: ρ_j, δ_j, and $\Delta\omega_j$. In the next section we present a criterion for choosing the ρ_j and introduce the approximation that all of the δ_j are equal.

III. CALCULATION OF EMISSIVITIES ACCORDING TO THE BAND MULTIPLICATION MODEL

A. Calculation of Emissivities at 600°K, Based on the Direct Use of Available Spectroscopic Data

Before proceeding with emissivity calculations according to Eqs. (18) and (18a), we attempt an a priori computation assuming that the CO_2 spectrum can be described by our random model but using only directly measured data for the band intensities. This type of calculation cannot be performed at higher temperatures because the required spectroscopic parameters are not available. At 600°K we may assume that the bands of importance are the same as those that have been identified and measured at 300°K. For each band, the integrated intensity at 600°K was calculated from the measured value at 300°K through use of the relation*

$$\frac{a(T)}{a(300^\circ K)} = \frac{N_T(T)}{N_T(300)} \frac{Q_V(300)}{Q_V(T)} e^{-\frac{W_V}{k}\left(\frac{1}{T}-\frac{1}{300}\right)} \left(\frac{1-e^{-hc\omega^*/kT}}{1-e^{-hc\omega^*/300k}} \right) \qquad (20)$$

where N_T = total number of molecules per unit volume per unit pressure, Q_V = vibrational partition function, and W_V = vibrational energy. These bands and their integrated intensities are listed in Table 2, which

---

* Ref. 7, p. 153.

Table 2:* Integrated intensities of bands considered for the band multiplication model.

Band Center	Transition	$a(300^{\circ}K)$[1]	$a(600^{\circ}K)$
		cm^{-2} - atm^{-1}	
648 cm^{-1}[2]	$01^{1}0 \rightarrow 00^{0}0$	1.88	0.526
667.3	$01^{1}0 \rightarrow 00^{0}0$	240.	67.0
720.5	$10^{0}0 \rightarrow 01^{1}0$	7.5	10.6
740.8	$11^{1}0 \rightarrow 02^{2}0$	.22	1.22
960.8	$00^{0}1 \rightarrow 10^{0}0$	.0219	.186
1063.6	$00^{0}1 \rightarrow 02^{0}0$	.0532	.361
1886	$04^{0}0 \rightarrow 01^{1}0$	.0415	.0675
1932.5	$03^{1}0 \rightarrow 00^{0}0$	.0415	.0137
2076.5	$11^{1}0 \rightarrow 00^{0}0$	.12	.040
2094	$12^{2}0 \rightarrow 01^{1}0$	.020	.033
2137[3]	$20^{0}0 \rightarrow 01^{1}0$	.007	.012
2284.5[2]	$00^{0}1 \rightarrow 00^{0}0$	30.0	10.0
2349.3	$00^{0}1 \rightarrow 00^{0}0$	2676	892
3609	$02^{0}1 \rightarrow 00^{0}0$	28.5	9.51
3716	$10^{0}1 \rightarrow 00^{0}0$	42.3	14.1
4860.5	$04^{0}1 \rightarrow 00^{0}0$	.272	.0909
4983.5	$12^{0}1 \rightarrow 00^{0}0$	1.01	.337
5109	$20^{0}1 \rightarrow 00^{0}0$	.426	.142

* Band identifications from Ref. 4, pg. 274.

(1) Ref. 7, pg. 310.

(2) These are transitions of the isotope $C^{13}O_2^{16}$, which is assumed to represent 1.1% of the total CO_2.

(3) This is the weakest band included, and may be considered to represent the sum of several very weak bands (see Ref. 7, pg. 314).

contains only the bands whose measured integrated intensities exceed 0.007 cm^{-2} atm^{-1} at 300°K. Using this listing, the grouping of bands into regions was performed according to the scheme described in Section IB. Letting s_j denote the number of measured bands in region j, we have $s_1 = 6$, $s_2 = 7$, and $s_3 = 2$.

At optical depths ranging from 0.0656 ft-atm to 3 ft-atm, the band absorption (A_i) for each measured band is computed by use of the just-overlapping line model. Next the weighted-mean value ($\overline{A}_j$) is found for the band absorption from Eq. (8a) and the average distance between band centers (δ_j) estimated. The average spectral emissivity for each region $\overline{\varepsilon}_j(\omega)$ is then computed from Eq. (9). The blackbody radiancies for use in Eqs. (10) or (18) are specified by assuming that the ratio of the total emissivity of the jth region (ε_j) for randomly distributed bands to the total emissivity of the jth region (ε_j^*) considering no overlapping of bands is the same as the corresponding ratio of mean spectral emmisivities, viz.,

$$\varepsilon_j / \varepsilon_j^* = \overline{\varepsilon}_j(\omega) / \overline{\varepsilon}_j^*(\omega)$$

where

$$\left.\begin{aligned} \varepsilon_j^* &= \frac{1}{\sigma T^4}\left[\sum_{\substack{\text{bands}\\ \text{within } \Delta\omega_j}} R^o_{\omega_j} \int_{\Delta\omega_i} (1-e^{-P_i X})d\omega\right]_j = \frac{1}{\sigma T^4}\sum_i R^o_{\omega_i} A_i, \\ \overline{\varepsilon}_j(\omega) &= 1-\exp(-\overline{A}_j/\delta_j), \\ \text{and} \quad \overline{\varepsilon}_j^*(\omega) &= \frac{1}{\Delta\omega_j}\sum_i \int_{\Delta\omega_i} (1-e^{-P_i X})d\omega = \frac{1}{\Delta\omega_j}\sum_i A_i \,. \end{aligned}\right\} \quad (21)$$

This expression may be rewritten as

$$\varepsilon_j = \frac{1}{\sigma T^4} \frac{\sum_i R^o_{\omega_i} A_i}{\sum_i A_i} \left[1-\exp(-\bar{A}_j/\delta_j)\right] \Delta\omega_j$$

$$= \frac{0.3148}{T} \rho_j \left[1-\exp(-\bar{g}_j)\right] \Delta\omega_j \qquad (22)$$

where

$$\rho_j = \frac{\sum_i \rho_{\omega_i} A_i}{\sum_i A_i} \; . \qquad (22a)$$

We note that Eq. (22) has the same form as Eq. (18) but that we have now defined ρ_j as the normalized blackbody function weighted with respect to the band absorptivities.

Values of δ_j for the first three spectral regions are 83.1, 77.2 and 107 cm^{-1}, respectively. At 600°K and 1 ft-atm we have, for example, $A_1 = 45.0\ cm^{-1}$ and $(0.3148/T)(\sum_{i=1}^{6} \rho_{\omega_i} A_i)_1 = 0.112$. Use of the relations $\Delta\omega_j = s_j\delta_j$ and $(\sum_{i=1}^{6} A_i)_j = s_j\bar{A}_j$, together with Eqs. (22) and (22a), results in the value 0.0862 for ε_1. Similar calculations of ε_2 and ε_3 yield 0.0492 and 0.00525, respectively. Addition of these contributions gives a total emissivity ε of 0.141. The corresponding value of Hottel's empirical results ε_H is 0.131.

Emissivities computed from Eq. (22) are shown in Fig. 10 together with Hottel's results. The observed satisfactory agreement between emissivities computed from spectroscopic data and the observed

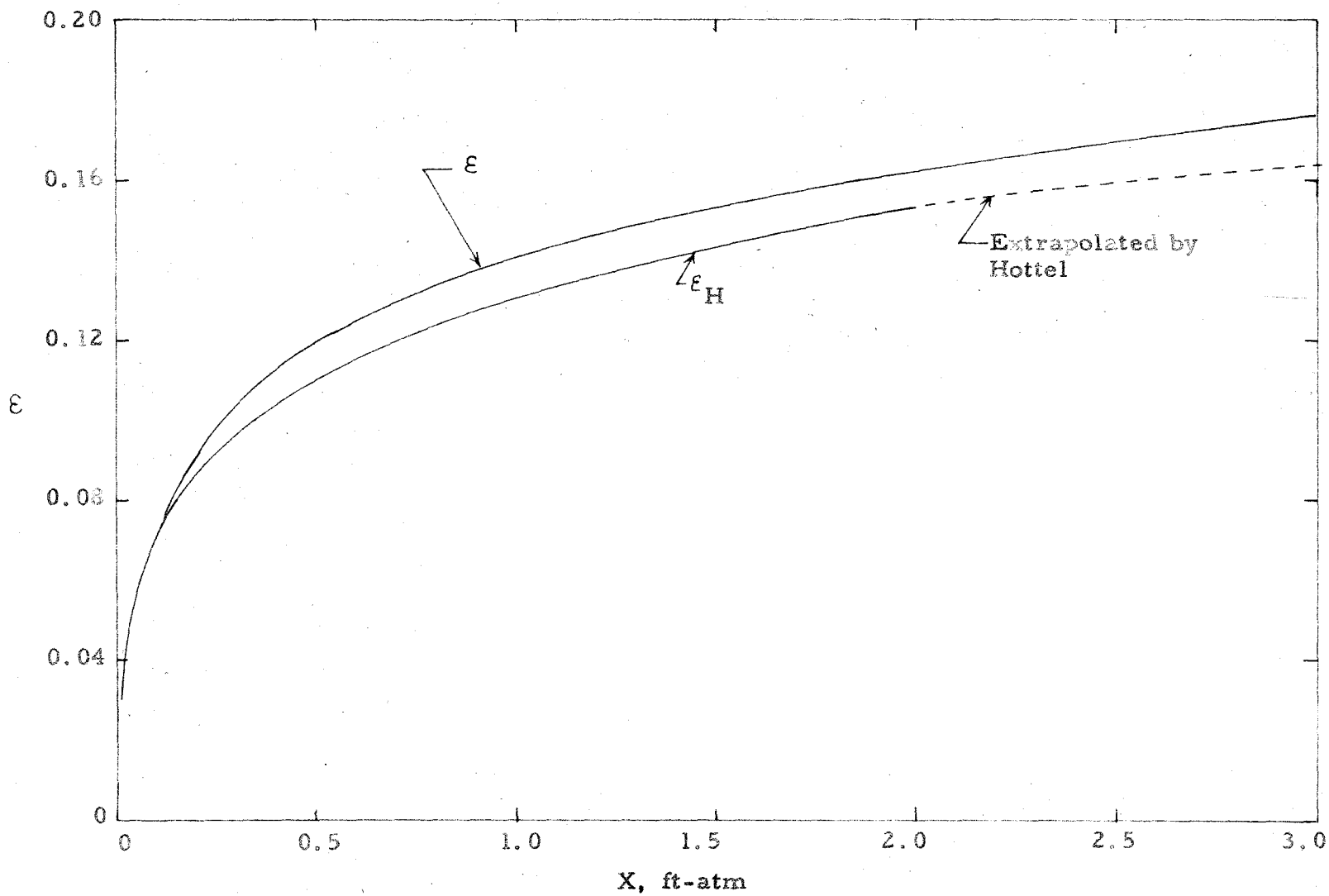

Fig. 10. Comparison of the emissivity ϵ with ε_H at 600°K; ε was calculated by use of the band multiplication model with available spectroscopic data.

emissivities suggests that the model we have adopted for calculation constitutes a reasonably satisfactory approximation.

Another interesting comparison may be made between our results and data obtained by numerical machine calculations for the spectral emissivity of CO_2 in the region of the ν_3-fundamental by G. N. Plass[8] who used the harmonic oscillator approximation for computing band intensities. Plass made calculations at 300 to 2400°K for a wide range of optical depths at different pressures, assuming collision-broadened spectral lines. A half-width b = 0.064 cm^{-1} at 1 atm and 298°K[9] was used and all transitions with n_3 changing by unity were considered. At the highest temperature, approximately 890,000 lines were involved. At 600°K, 70 bands were taken into account. The 4.8 and 5.2μ bands were also included. At 300°K, the rotational band structure was described by the Elsasser model, while at 2400°K it was described by a statistical model. At intermediate temperatures, a random Elsasser structure was used.[10] We shall restrict our comparison to data applicable at a total pressure of 1 atm. Plass' spectral emissivity curves* were converted to total emissivity data by use of the relation

$$\varepsilon = \frac{0.3148}{T} \int_{\Delta\omega} \rho_\omega \varepsilon_\omega \, d\omega.$$

Here, $\Delta\omega$ refers to the total width of the spectral emissivity curve as presented in Plass' report. Results for ε are given in Table 3. A comparison between ε derived from Plass' data and our estimates for $\varepsilon = \varepsilon_2$ derived from spectroscopic data [and also with $\varepsilon_2(b)$, the

* The curves were obtained from the publication listed as Ref. 11.

Table 3. Total emissivities ε_2 in the region of the ν_3-fundamental computed from Plass' spectral emissivities.

T / X ft, atm	300°K	600	1200	1800	2400
3.28×10^{-6}	2.86×10^{-5}	4.45×10^{-4}			
3.28×10^{-4}	3.80×10^{-4}	0.00430	0.00183	5.11×10^{-4}	
3.28×10^{-2}	0.00159	.0253	.0157	0.00620	0.00236
3.28	.00321*	.0525*	.0603**	.0310	.0159**
3.28×10^{2}			.112*	.0588*	.0373*

* The plotted curves were extended and the tabulated results may be somewhat too small.

** The plotted curves were extended only slightly.

calculation of which will be discussed in Section IIIC] appears in Fig. 11. Two points derived from Plass are applicable, giving results which are seen to be in good accord with our estimates. It should be noted that Plass' point at 3.28 ft-atm may actually be slightly higher than indicated for the reason mentioned in the footnote to Table 3. Plass has stated that his spectral results at room temperature agree closely with the experiments of Howard, Burch and Williams,[12] while those at 600°K are slightly higher than the measurements of Tourin.[13] Plass' results are lower than Tourin's at 1200°K.

B. Calculation of Emissivities at 300°K, Based on Spectroscopic Data and Experimentally Determined Total Emissivities

1. Discussion of parameters

We now consider methods for choosing the parameters that characterize the emission of CO_2. In order to reduce the number of parameters,

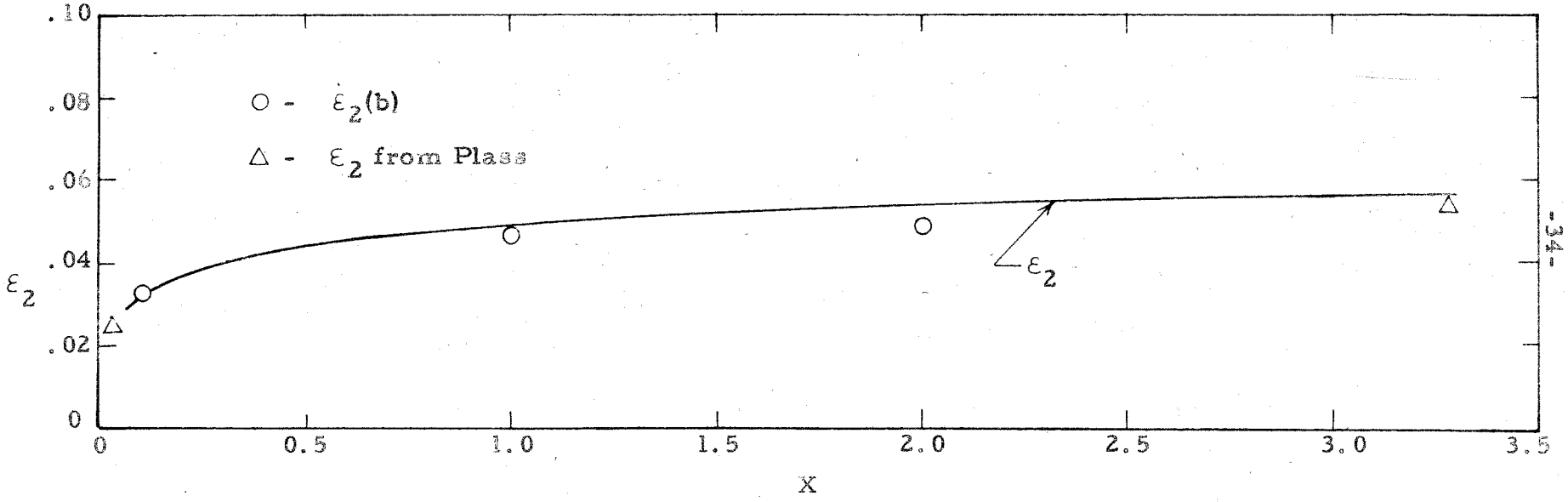

Fig. 11. Comparison of emissivity ε_2 in the second spectral region at 600°K (calculated by use of the band multiplication model and based on available spectroscopic data) with the results of Plass.[8], [11] The values indicated as ε_2(b) are discussed in Section C3.

we assume that the mean spacing (δ_o) is the same in all spectral regions for which the statistical approach is useful. At the higher temperatures, at which a great number of bands is present, this assumption should be quite reasonable. At lower temperatures, inspection of the measured transitions (cf. Table 2) also validates this assumption. In our calculations, the emissivity contributions made by the first two regions will be treated by statistical methods. It should perhaps be emphasized that we infer the relation $\delta_1 = \delta_2$ without meaning to imply that the average of these values should be used in practice. The substitution of the averaged weak bands for the actual ones does not imply that the effective region width should be identified with the distance between the band extremeties since most of the bands will be clustered in a relatively small spectral interval for the first and second spectral regions. In practice, an "effective" representation is best obtained by determining δ_o and $\Delta\omega_j$ from a fit of experimentally measured emissivity data. The final selections must be consistent with the idea that the actual number of bands N_j in the region $\Delta\omega_j$ is $N_j = \Delta\omega_j / \delta_o$.

In attempting a fit to the measured emissivity data, we consider first the emissivity at 300°K where region 1 makes the dominant contributions; region 2 contributes only about 2% of the intensity and the remaining regions are of negligible importance. We may therefore choose δ_o and $\Delta\omega_1$, neglecting ε_2 in first approximation; in a second iteration we may include ε_2 and amend slightly our choices for δ_o and $\Delta\omega_1$. The choice of the parameters δ_o and $\Delta\omega_1$ is of great importance for the high-temperature calculations.

2. Determination of the average blackbody functions for the first and second spectral regions

The wave number $\bar{\omega}_j$ at which ρ_j is calculated for each region is best determined at a temperature at which the region contributes most strongly to the emissivity. As we have seen, this temperature is about 300°K for region 1. At 600°K we found it appropriate to average over the contributing bands according to Eq. (22a); for region 1, Eq. (22a) becomes

$$\rho_1 = \frac{\varepsilon_{667}\,\rho_{667} + \varepsilon_1^*\rho_1^*}{\varepsilon_{667} + \varepsilon_1^*}$$

where $\varepsilon_{667} = 1-\exp(-g_{667})$ = spectral emissivity of ν_2-fundamental, $\varepsilon_1^* = 1-\exp(-\bar{g}_1^*)$ = spectral emissivity of the average remaining bands of the first region, and ρ_{667} and ρ_1^* are the corresponding normalized blackbody functions. At 300°K,

$$g_{667} = \frac{4B_e}{\sqrt{\gamma\delta}}\ I(K_{667}) = 36.1\ I(K_{667})/\delta$$

and

$$g_1^* = \frac{4B_e}{\sqrt{\gamma\delta}}\ I(K_1^*) = 36.1\ I(K_1^*)/\delta\ .$$

Each value of optical depth, region width, and average band spacing leads to an average blackbody function. For a given value of X, we first calculate $g_{667}\delta_o$ and $g_1^*\delta_o$ as functions of N_1 where $N_1 = \Delta\omega_1/\delta_o$. Then, for a given value of δ_o, we obtain g_{667} and g_1^* and therefore also ε_{667} and ε_1^* as functions of $\Delta\omega_1$. We finally obtain ρ_1 as a function of $\Delta\omega_1$ for given δ_o. This procedure is then repeated for all values of δ_o and X under consideration.

One method for determining the wavenumber ω_1^* at which ρ_1^* is evaluated involves setting the short wavenumber limit $\delta_o/2$ below the center of the limiting observed band; thus ω_1^* (cm^{-1}) = 597 + $\Delta\omega_1/2 - \delta_o/2$. In another method, we set ω_1^* equal to the arithmetic mean value for the region considering the strongest bands that remain after the fundamental has been excluded. For region 1 there are two bands, viz., a_{648} = 1.88 cm^{-2}-atm^{-1} at 300°K, $a_{720.5}$ = 7.5 cm^{-2}-atm^{-1} at 300°K. The average wave number is therefore 684 cm^{-1}, giving ρ_{648} = 0.967. The second procedure is presumably valid at least until the region half-width ($\Delta\omega_1/2$) exceeds (684-597) + $\delta_o/2$ = 87 + $\delta_o/2$ because no reasonably strong identified bands are known to exist below the 597 cm^{-1} band. For $\Delta\omega_1 \simeq 200$ cm^{-1} and $\delta_o \simeq 20$ cm^{-1}, which appear best for a fit at 300°K, the first two methods lead to similar values for ρ_1. For X = 1 ft-atm with $\Delta\omega_1$ = 180 cm^{-1} and δ_o = 20 cm^{-1}, the first method gives ρ_1 = 0.977 while the second gives ρ_1 = 0.975. For X = 0.1 ft-atm at the same values of $\Delta\omega_1$ and δ_o, the methods give 0.980 and 0.979, respectively, indicating that the variation of ρ_1 with changes in X is small. We expect ρ_j to vary significantly with X only in a region which contains either a relatively weak fundamental or no fundamental at all, as well as an asymmetric distribution of the remaining bands. This state of affairs is illustrated in Fig. 12 where an increase in optical depth from X to 2X would cause the average blackbody function to shift to a larger wavenumber.

The calculation of ρ_2 is similar to that of ρ_1; however, here we must separate both the very intense normal and isotopic fundamentals from the remaining bands. Preliminary calculations of ε_2 indicate

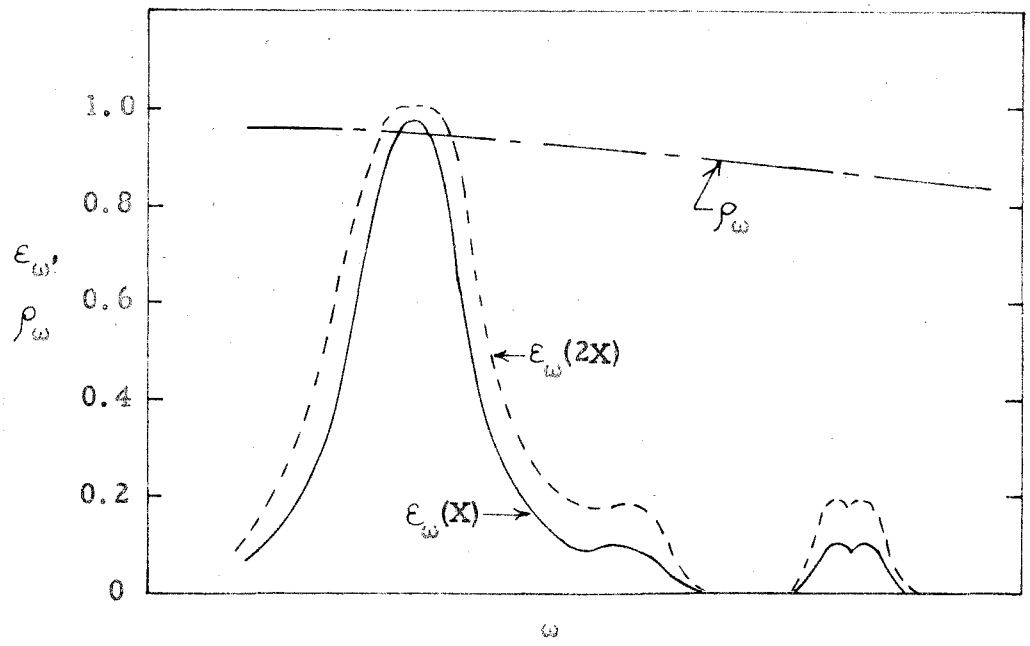

Fig. 12. Hypothetical asymmetric band structure, suggesting the effect of optical depth upon the choice of the average blackbody function.

that its maximum value occurs at about 900°K. At this temperature, ρ_2 is found to be equal to 0.898. The change of ρ_2 with $\Delta\omega_2$ is negligible because of the large intensity of the ν_3-fundamental. Values of ρ_j for the first four spectral regions appear in Table 4.

Table 4. Average blackbody functions for the first four spectral regions.

T	ρ_1	ρ_2	ρ_3	ρ_4
300°K	0.978	0.0138	0.894×10^{-4}	0.395×10^{-6}
600	.732	.458	.0727	.00775
900	.451	.898	.404	.123
1200	.296	1.00	.747	.382
1500	.207	.940	.937	.651
1750	.160	.851	.995	.817
2400		.631		

3. Identification of the parameters δ_o and $\Delta\omega_1$

Use of Eqs. (18) and (19) gives

$$\epsilon_1 = 1.05 \times 10^{-3} \rho_1 (1-e^{-\bar{g}_1}) \Delta\omega_1 \tag{23}$$

where

$$\bar{g}_1 = \frac{36.1}{\Delta\omega_1} \left\{ I(K_{667}) + \left[\frac{\Delta\omega_1}{\delta_o} - 1 \right] I(K_1^*) \right\} . \tag{24}$$

Although we use five bands to determine the value of a_1^*, calculations keeping N_1 at a fixed integral value do not lead to satisfactory results. If we permit N_1 to be determined as the ratio $\Delta\omega_1/\delta_o$, fairly

good results may be obtained over wide ranges of the variables by suitable adjustments of ρ_1. Three good choices for the parameters are shown in Fig. 13. For $\Delta\omega_1 = 504$ cm^{-1} and $\delta_o = 180$ cm^{-1}, ρ_1 is required to be 0.875 and the resulting value of N_1 is 2.8. The arbitrary choice of ρ_1 and the conclusion that fewer than 3 bands are present are unsatisfactory. Furthermore, since most of the bands in the first region are located within a relatively small wavelength interval, it is expected that "best values" for $\Delta\omega_1$ and δ_o are actually considerably smaller than the above values. With reasonable choices for the parameters, two additional curves for correlating the data may be drawn (cf. Fig. 13). In spite of this success, it is certainly desirable to use properly averaged values of ρ_1 obtained from Eq. (22a) and to adopt a method of determination of $\Delta\omega_1$ and δ_o which is less arbitrary.

Investigation of the interdependence of $\Delta\omega_1$, δ_o, and ρ_1 shows that the following numerical estimates are preferred: $\rho_1 \simeq 0.98$, $185 \text{ cm}^{-1} > \Delta\omega_1 > 175 \text{ cm}^{-1}$, and $30 > \delta_o > 15$. The results of calculations of ε_1 with these values (for X = 0.1, 1.0, and 2.0 ft-atm) appear in Fig. 14. Reference to Fig. 14 shows that the results for 0.1 ft-atm are insensitive to δ_o enabling us to choose $\Delta\omega_1 = 181$ cm^{-1} from the intersection with the line $\varepsilon_H = 0.085$. In turn, the intersections of the extreme ε_1 vs. $\Delta\omega_1$ curves (with respect to δ_o) for 1 and 2 ft-atm with the corresponding ε_H curves contain, within their limits, the determined value of $\Delta\omega_1$. We find $\delta_o = 24$ cm^{-1} to be an appropriate compromise value leading to $N_1 = 7.54$ and $\rho_1 = 0.978$. This value of ρ_1 is accurate to better than 0.4% for X between 0.1 and 2 ft-atm and corresponds to $\bar{\omega}_1 = 670$ cm^{-1}.

The stated choice of parameters causes ε to exceed ε_H slightly at

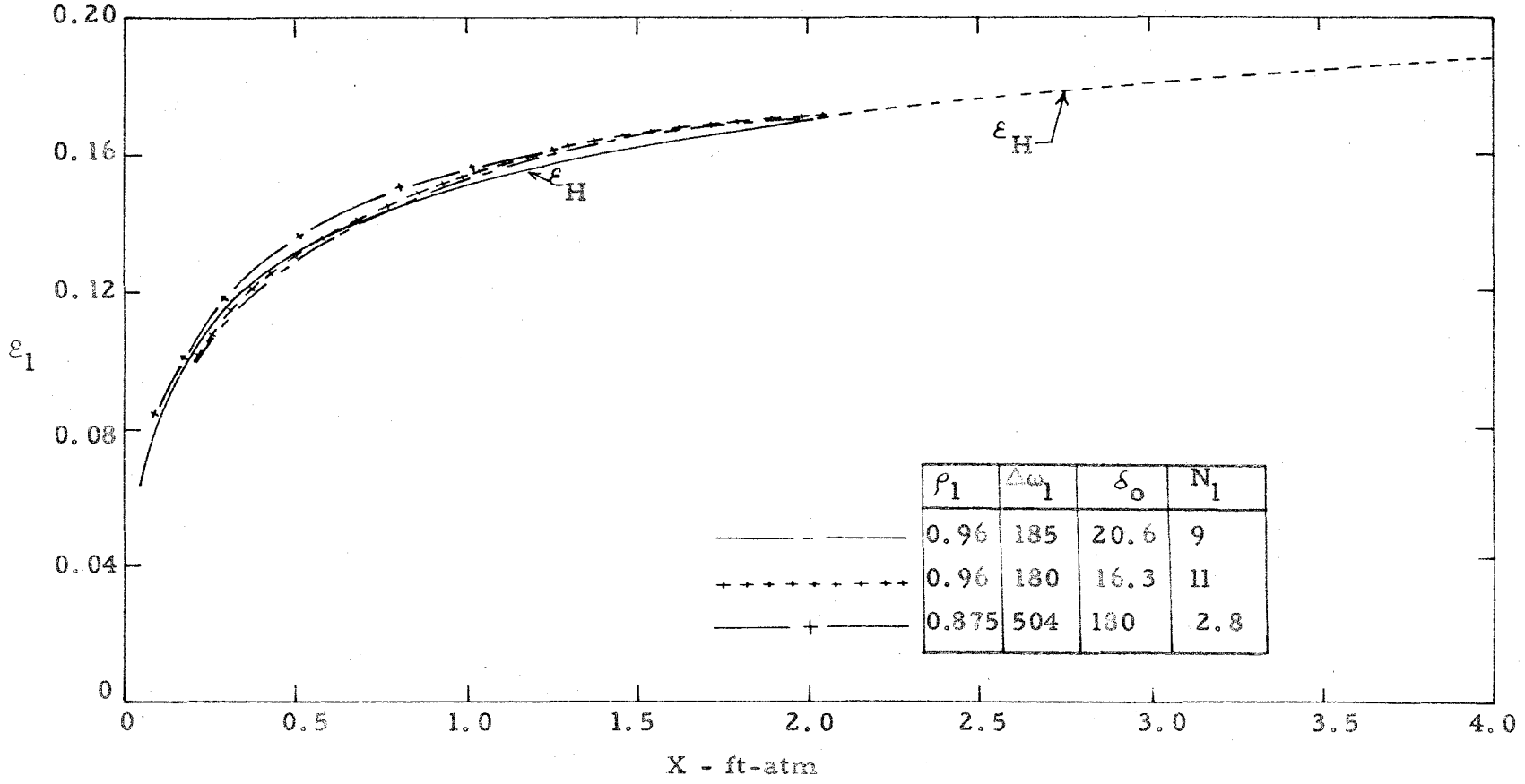

Fig. 13. Preliminary determinations of the width of the first region and of the mean band spacing at 300°K.

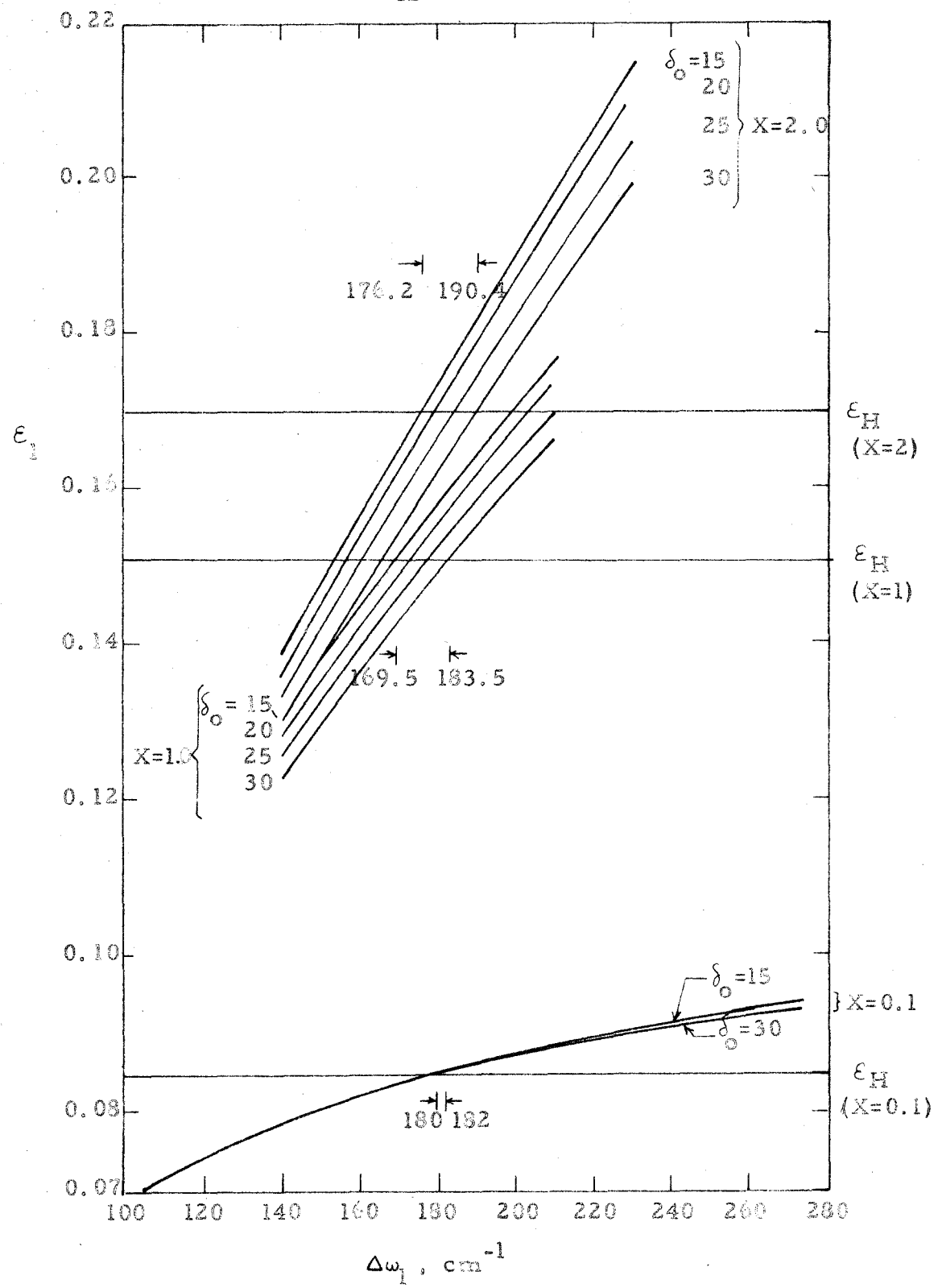

Fig. 14. Emissivities ε_1 of the first region as a function of region width and mean band spacing at 300°K, using appropriate values of the normalized blackbody function.

1 ft-atm while it is slightly less than ε_H at 2 ft-atm. For comparison, ε was also calculated at $\delta_o = 21\ cm^{-1}$ and $\Delta\omega_1 = 181\ cm^{-1}$ which gives increased importance to the emissivity at the larger optical depths. The results appear in Fig. 15. From an examination of the results, it may be concluded that the calculated emissivity at large optical depths cannot be as large as Hottel's almost linear extrapolation. As $X \to \infty$, ε must approach a constant value that is given by $(0.3148/T)\rho_1 \Delta\omega_1$.

C. Calculation of Emissivities at Elevated Temperatures Based on Parameters Determined from 300°K Results

As the temperature is increased above 300°K, the relative importance of the first region decreases while that of the remaining regions increases. At 600°K, preliminary calculations indicate that the emissivities of the first two regions are of the same order of magnitude while the second contributes about ten times the amount of the first at 1750°K. The third region contributes more than the first at 900°K and as much as the second at 1500°K. The largest value of ε_2 occurs at about 900°K and that of ε_3 at about 1300°K. The general shape of the ε vs. T curves, as seen in Figs. 1, 21, 22, and 23, arises largely from the variation of the blackbody curve with temperature.

1. Determination of region widths

For a region containing many bands, the width is well approximated by $(N_j-1)\,\delta_o$. When relatively few bands are present, the width lies between $N_j\,\delta_o$ and $\left[(N_j-1)\,\delta_o + \Delta\omega_B\right]$ for $\Delta\omega_B > \delta_o$. A suitable compromise is reached if we choose the region width as $N_j\,\delta_o$ which is valid for $\Delta\omega_B/2$ somewhat larger than δ_o. For region 1, we find $\Delta\omega_B/2 \simeq 2\,\delta_o$.

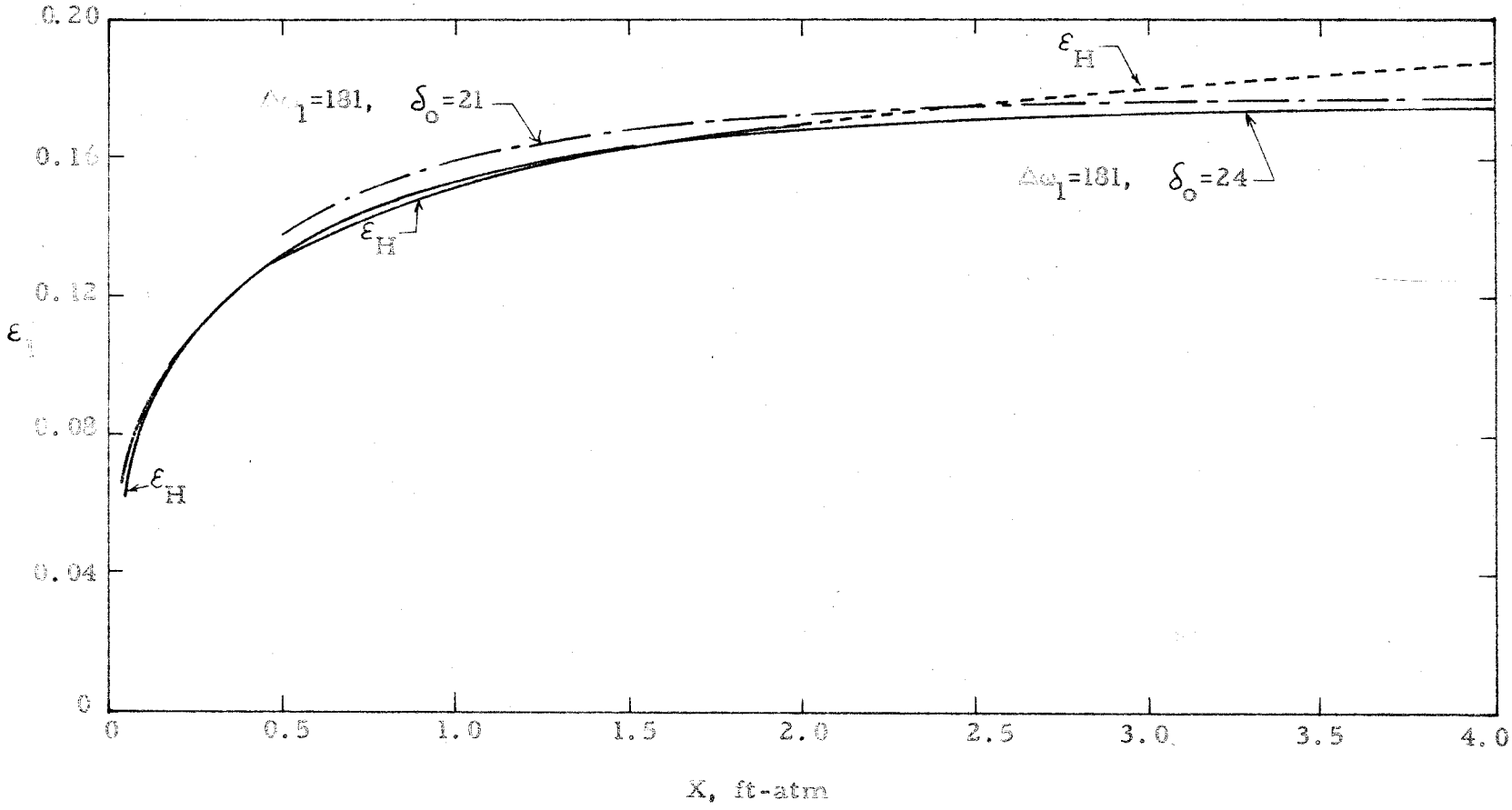

Fig. 15. Emissivity ε_1 of the first region at 300°K, calculated by the band multiplication model for the best choice of region width and mean band spacing (181 cm^{-1}, 24 cm^{-1}, respectively), and also for a choice of the parameters which gives increased importance to the results at the larger optical depths ($\Delta\omega_1$ = 181 cm^{-1}, δ_o = 21 cm^{-1}).

In order to extrapolate $\Delta\omega_1$ to higher temperatures, we consider $\Delta\omega_1$ (300°K) to be equal to $(N_1\text{-}1)\,\delta_o + D(T)$ making $D = 25\ cm^{-1} \simeq \Delta\omega_B/4$. This selection of D corresponds to computing the region width by adding 1/8 of the band width onto each end of the spectral interval between the extreme band centers of the region.

The form of the temperature dependent function D(T) is identified with the temperature variation of the effective width of an isolated band. Thus $D(T) \propto \sqrt{T}$ and $\Delta\omega_1$ is now computed from

$$\Delta\omega_1 = 156 + \Delta\omega_B/4 = 156 + 26.9\sqrt{T/300}\,. \tag{25}$$

Similarly, we compute $\Delta\omega_2$ from the relation

$$\Delta\omega_2 = \text{constant} + 26.9\sqrt{T/300}$$

where the constant has not yet been defined.

Calculations for region 3, which consists of two bands, have been performed using the just-overlapping line and box profiles for the bands. The band spacing is almost exactly the same as $\Delta\omega_B$ at 300°K. The extent of band overlapping at elevated temperatures is indicated in Table 5. For use with the box model, $\Delta\omega_3$ was calculated by adding

Table 5. Band overlapping in region 3

T	$\Delta\omega_B$	Spectral extent of band overlapping
300°K	108 cm^{-1}	1 cm^{-1}
600	152	45
900	187	80
1200	215	108
1500	241	134
1750	259	152

$(1/2)\left[\Delta\omega_B(300^\circ K)-\Delta\omega_B(T)\right]$ to the region width calculated at $300^\circ K$, viz.,

$$\Delta\omega_3 = 215 + (6.20/2)(\sqrt{T} - \sqrt{300}) = 161 + 53.7\ \sqrt{T/300}. \qquad (26)$$

2. Variation of the number of bands within a region with temperature

As the temperature increases, the number of bands contributing to the emissivity increases. This effect may be treated in two ways. The first involves a redistribution of the intensity through use of a mean band spacing $\delta(T)$ which decreases with temperature according to

$$\delta(T) = \delta_o\left(\frac{300}{T}\right)^{\mathcal{S}} \qquad (27)$$

where $\delta_o = \delta(300^\circ K)$ and $\Delta\omega_j$ is considered to be approximately constant. Calculations performed with values of $\mathcal{S}$ from 0 to 5 showed no significant change in ε_1 at $1500^\circ K$.

The second method, which will be discussed in Section C4, involves a system of bands that is assumed to cover the entire spectrum at the higher temperatures.

3. Calculation of emissivities

At elevated temperatures, ε_j may be calculated by assuming that $\Delta\omega_j = \Delta\omega_j(T)$ and $N_j = \Delta\omega_j(T)/\delta_o$ so that both the region width and the number of bands increase with temperature, without introducing any "new" integrated intensity into the region.*

---

* Comparative computations made according to other procedures indicated that the choice of method is unimportant for the calculation of ε_1 while it is of significance for the calculation of ε_2. The other procedures are the following: (a) the use of constant values of $\Delta\omega_j$ and N_j and (b) the use of $\Delta\omega_j=\Delta\omega_j(T)$ with $N_j=N_j(300^\circ K)$ = constant.

Using Eqs. (18) and (19), we obtain the following relations for the calculation of $\mathcal{E}_1$:

$$\mathcal{E}_1 = \frac{0.3148}{T} \rho_1 (1 - e^{-\bar{g}_1}) \Delta\omega_1 \tag{28}$$

where

$$\bar{g}_1 = \frac{36.1}{\Delta\omega_1} \sqrt{\frac{T}{300}} \left\{ I(K_{667}) + \left[\frac{\Delta\omega_1}{\delta_o} - 1 \right] I(K_1^*) \right\}, \tag{29}$$

$$K_1^* = 16.4 X \left(\frac{300}{T} \right)^{3/2} \left(\frac{\Delta\omega_1}{\delta_o} - 1 \right)^{-1}, \tag{30}$$

$$K_{667} = \left\{ \begin{array}{l} 405 X \, (300/T)^{3/2} \text{ for } a_{667} = 240(300/T) \text{ cm}^{-2} \text{ atm}^{-1} \text{*} \\ \\ 287 X \, (300/T)^{3/2} \text{ for } a_{667} = 169.5 (300/T) \text{ cm}^{-2} \text{ atm}^{-1} \end{array} \right\}, \tag{31}$$

and X is expressed in ft-atm. In practice, the two estimates of K_{667} are very close because of the insensitivity of I to K for large values of K. The higher value was actually used in our calculations. The results appear in Fig. 16 together with a listing of the variation of $\Delta\omega_1$ with T.

At 600°K and 1 ft-atm, $\mathcal{E}_1$ is calculated in the following fashion: from Eq. (25) we obtain $\Delta\omega_1 = 194$ cm^{-1} and, using $\delta_o = 24$ cm^{-1}, we find $N_1 = 8.08$. Equations (30) and (31) give $K_1^* = 0.889$ and $K_{667} = 144$ which leads, through use of Figs. 7 and 9, to $I(K_1^*) = 0.387$ and $I(K_{667}) = 2.53$. We therefore find $\bar{g}_1 = 1.39$ and, using $\rho_1 = 0.732$ from Table 4,

---

* We use the approximate relation $a(T) = (T_o/T)\, a(T_o)$, where T_o is a reference temperature, rather than Eq. (20).

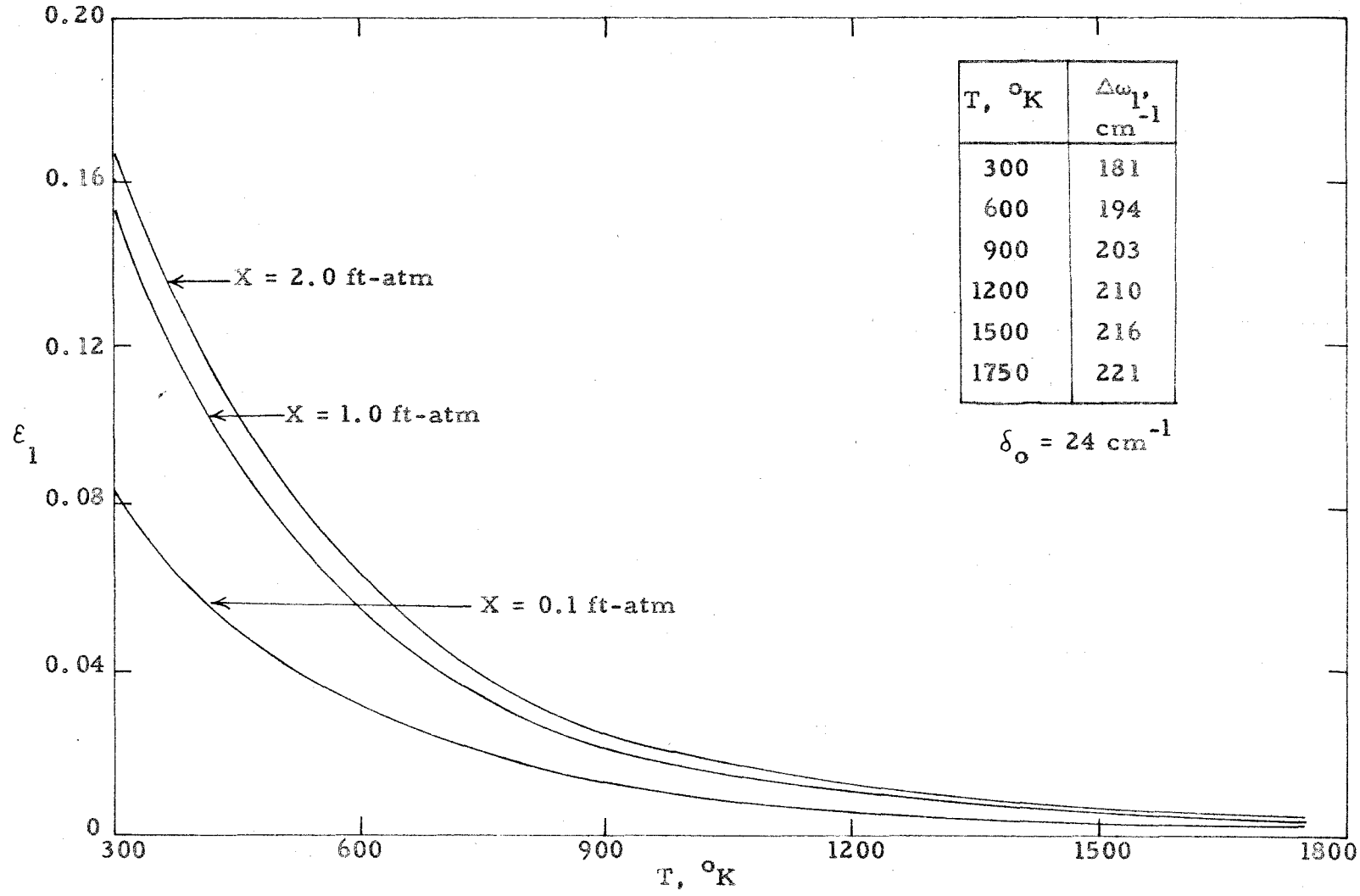

Fig. 16. Emissivities ε_1 of the first region, calculated by the band multiplication model.

we obtain $\varepsilon_1 = 0.0559$.

For the calculation of ε_2, we have

$$\bar{g}_2 = \frac{36.1}{\Delta\omega_2}\sqrt{\frac{T}{300}}\left\{I(K_{2349}) + I(K_{2285}) + \left[\frac{\Delta\omega_2}{\delta_o} - 2\right] I(K_2^*)\right\} , \qquad (32)$$

$$K_2^* = 0.389\,X\left(\frac{300}{T}\right)^{3/2}\left(\frac{\Delta\omega_2}{\delta_o} - 2\right)^{-1} , \qquad (33)$$

$$K_{2285} = 50.8\,X\,(300/T)^{3/2} , \qquad (34)$$

$$K_{2349} = 4525\,X\,(300/T)^{3/2} . \qquad (35)$$

The averaging of $I(K_{2349})$ and $I(K_{2285})$ is justified in view of the large spectral emissivities of the normal and isotopic ν_3-fundamentals.

The quantity ε_2 is plotted in Fig. 17 as a function of $\Delta\omega_2$ for constant temperature at 1 ft-atm. Computations of ε_2 corresponding to temperature-dependent values of $\Delta\omega_2$ are labelled $\varepsilon_2(a)$, which refers to the choice $\Delta\omega_2 = 322$ cm^{-1} at 900°K; $\varepsilon_2(b)$, corresponds to $\Delta\omega_2 = 422$ cm^{-1}; $\varepsilon_2(c)$ corresponds to $\Delta\omega_2 = 522$ cm^{-1}. The results are plotted in Fig. 18 for 1 ft-atm and in Fig. 19 for 0.1 and 2 ft-atm. The variations of $\Delta\omega_2$ with T for $\varepsilon_2(a)$, $\varepsilon_2(b)$ and $\varepsilon_2(c)$ are also listed in Fig. 18. Inspection of experimental and theoretical spectral profiles of the second region at elevated temperatures[8], [14], [15], [16] indicates that the region widths used in the calculation of $\varepsilon_2(b)$ are appropriate at the larger optical depths, while those used for $\varepsilon_2(a)$ are appropriate at small depths. The error in using a single choice for $\Delta\omega_2$ is smallest if we favor the larger optical depths for the selection of $\varepsilon_2(b)$.

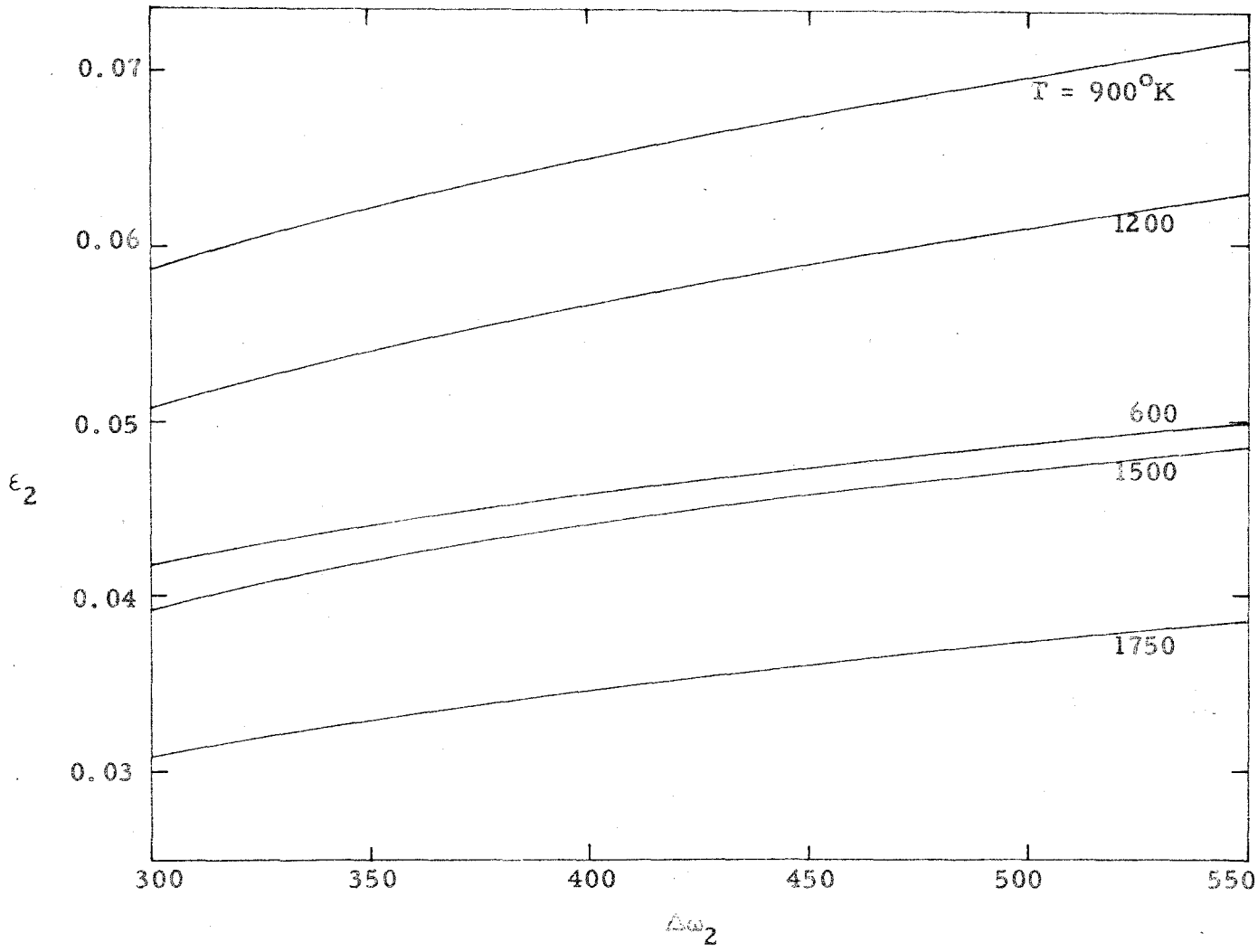

Fig. 17. Emissivities ϵ_2 of the second region calculated by the band multiplication model as a function of region width, for X = 1 ft-atm.

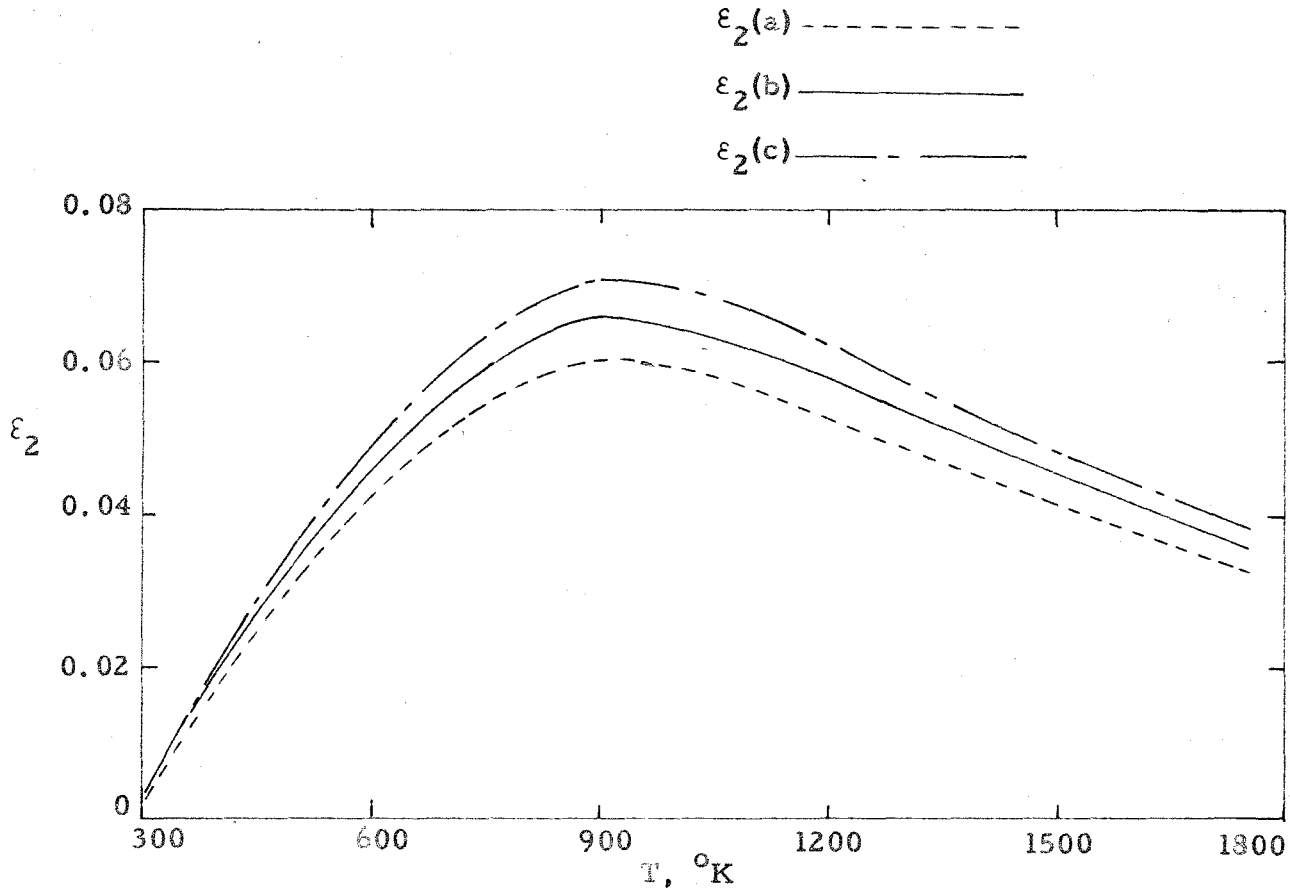

	$\Delta\omega_2$, cm^{-1} for		
T, °K	ε_2(a)	ε_2(b)	ε_2(c)
300	302	402	502
600	313	413	513
900	322	422	522
1200	329	429	529
1500	335	435	535
1750	340	440	540

δ_o = 24 cm^{-1}

Fig. 18. Emissivities ε_2 of the second region, calculated by the band multiplication model, for X = 1 ft-atm.

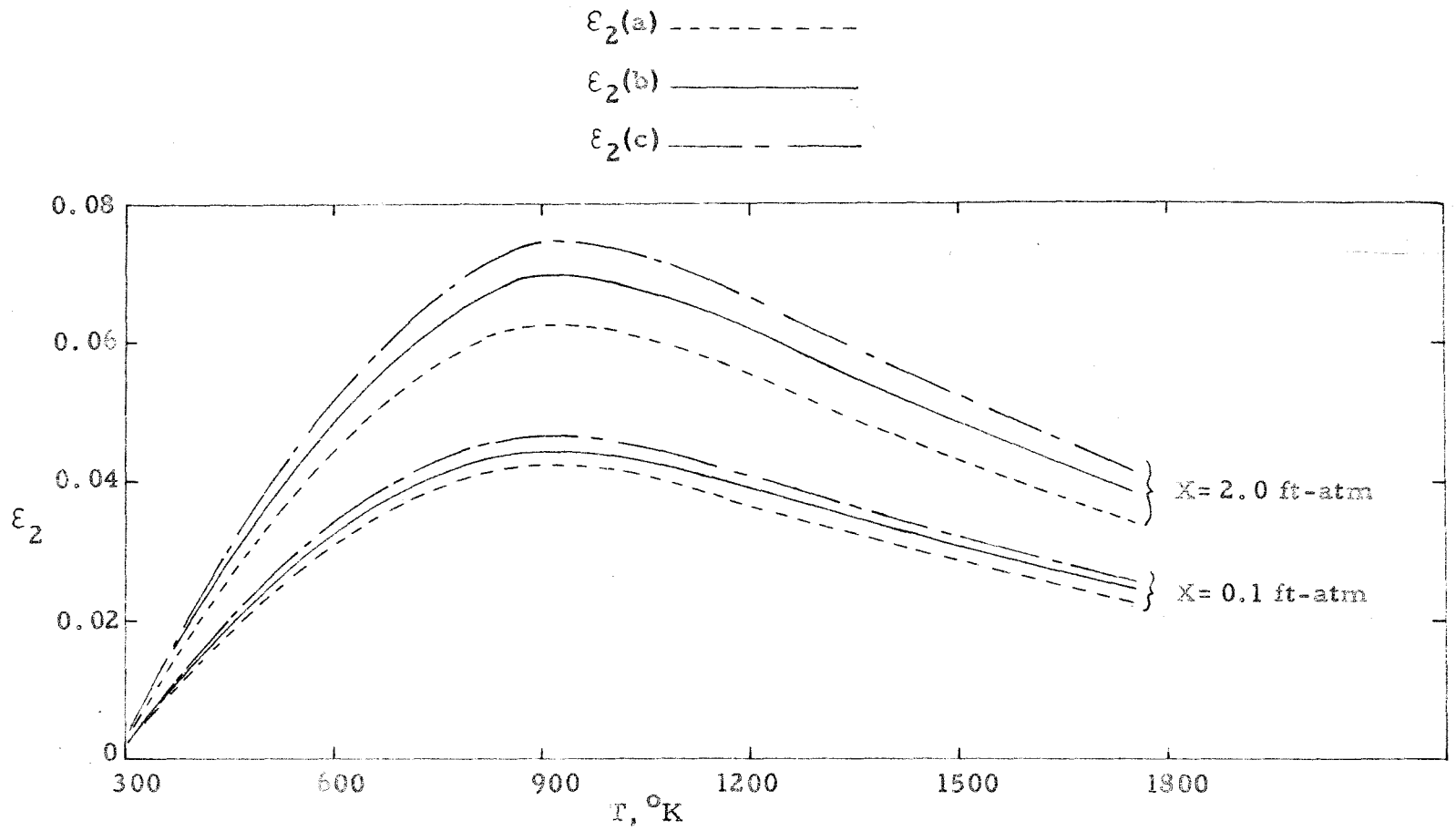

Fig. 19. Emissivities ε_2 of the second region, calculated by the band multiplication model, for X = 0.1 and 2.0 ft-atm.

Since region 3 contains only two "just-touching" bands at 300°K and since their integrated intensities are similar, ε_3 may be calculated by characterizing the two bands by an average absorption coefficient extending over a region width ($\Delta\omega_3$) that is given by Eq. (26). We obtain for the emissivity of region 3

$$\varepsilon_3(a) = \frac{0.3148}{T} \rho_3 \left\{1-\exp\left[-\frac{2160}{\Delta\omega_3}\left(\frac{300}{T}\right)X\right]\right\} \Delta\omega_3 \tag{36}$$

where ρ_3 is evaluated at the average wavenumber of the two band centers. The quantity ε_3 was also calculated by summing the emissivities of the two bands on the basis of the just-overlapping line model for the bands, viz.,

$$\varepsilon_3(b) = 0.0379\sqrt{\frac{300}{T}}\left[\rho_{3609}\, I(K_{3609}) + \rho_{3716}\, I(K_{3716})\right] \tag{37}$$

where

$$K_{3609} = 48.2\,X\,(300/T)^{3/2} \tag{38}$$

and

$$K_{3716} = 71.5\,X\,(300/T)^{3/2}\,. \tag{39}$$

The results, which are seen to be similar, are plotted in Fig. 20. It is believed that $\varepsilon_3(a)$ is more reliable than $\varepsilon_3(b)$ since band overlapping has been allowed for in the calculation of $\varepsilon_3(a)$.

The contribution to the emissivity from region 4 is very small; at the lower temperatures it is negligibly small. Above 900°K, calculations indicate that the transparent gas relation is appropriate and we obtain

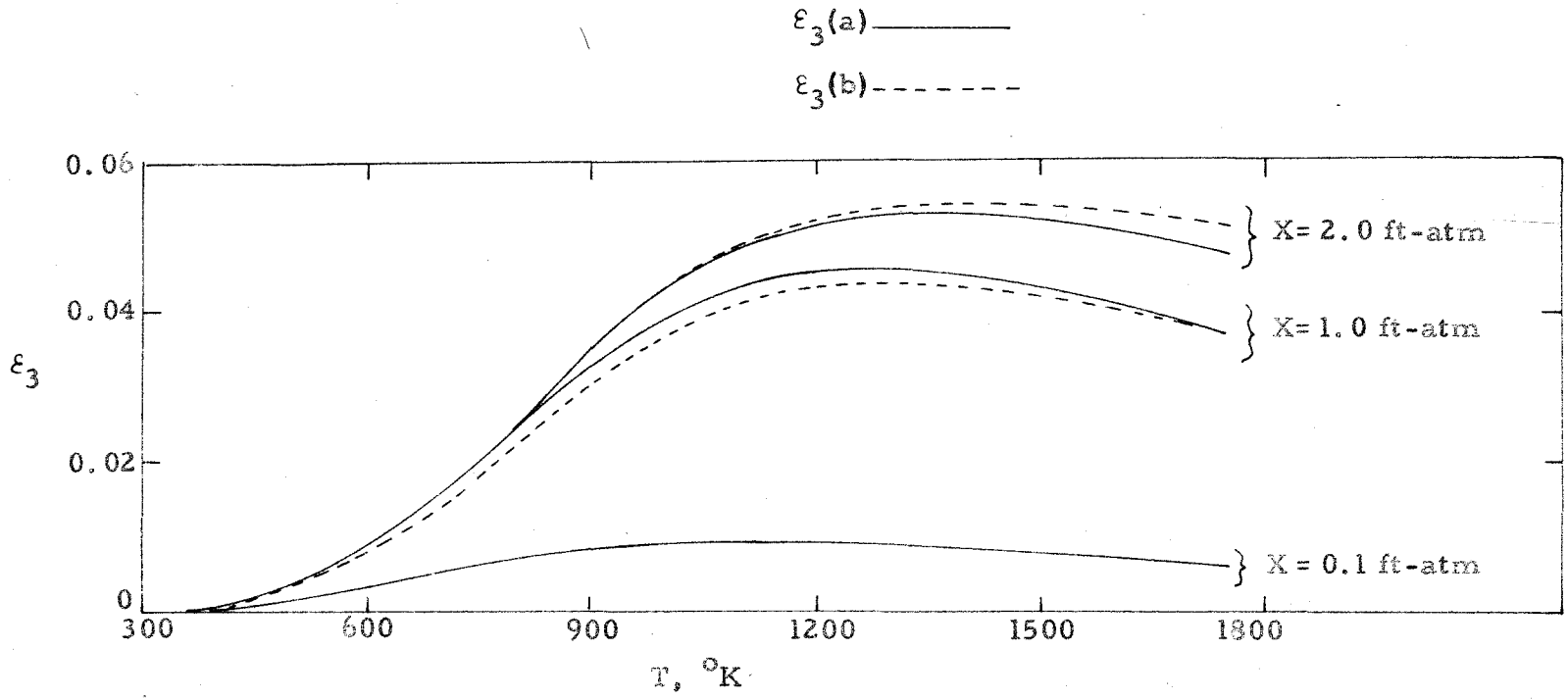

Fig. 20. Emissivities ε_3 of the third region, calculated by the box model $\left[\varepsilon_3(a)\right]$ and by the just-overlapping line model $\left[\varepsilon_3(b)\right]$.

$$\varepsilon_4 = 0.0544\ \rho_4 X\ (300/T)^2 \qquad (40)$$

where we have summed the contributions from the three bands. Here ρ_4 is evaluated at the average wavenumber of the band centers which is almost at the center of the middle (and strongest) band. Values of ε_4 appear in Table 6 to the nearest 0.0001.

Table 6. Emissivities of region 4

T \ X	0.1 ft-atm	1.0 ft-atm	2.0 ft-atm
300°K	--	--	--
600	--	0.0001	0.0002
900	0.0001	0.0007	.0015
1200	.0001	.0013	.0026
1500	.0001	.0014	.0028
1750	.0001	.0013	.0026

From Eq. (18a) we finally obtain for the total emissivity

$$\varepsilon = \varepsilon_1 + \varepsilon_2(b) + \varepsilon_3(a) + \varepsilon_4 . \qquad (18b)$$

Curves of ε and ε_H as functions of temperature at 0.1, 1.0, and 2.0 ft-atm appear in Figs. 21 and 22. Small contributions to the emissivity at 300°K from the second and third spectral regions cause the calculated values to exceed ε_H somewhat. Slight adjustments of $\Delta\omega_1$ and δ_o would remedy this but, in view of the overall accuracy, are not warranted.

4. Additional contributions to the emissivities

In order to explore the discrepancy between ε and ε_H, we considered next the possible existence of a continuous weak band distribution at

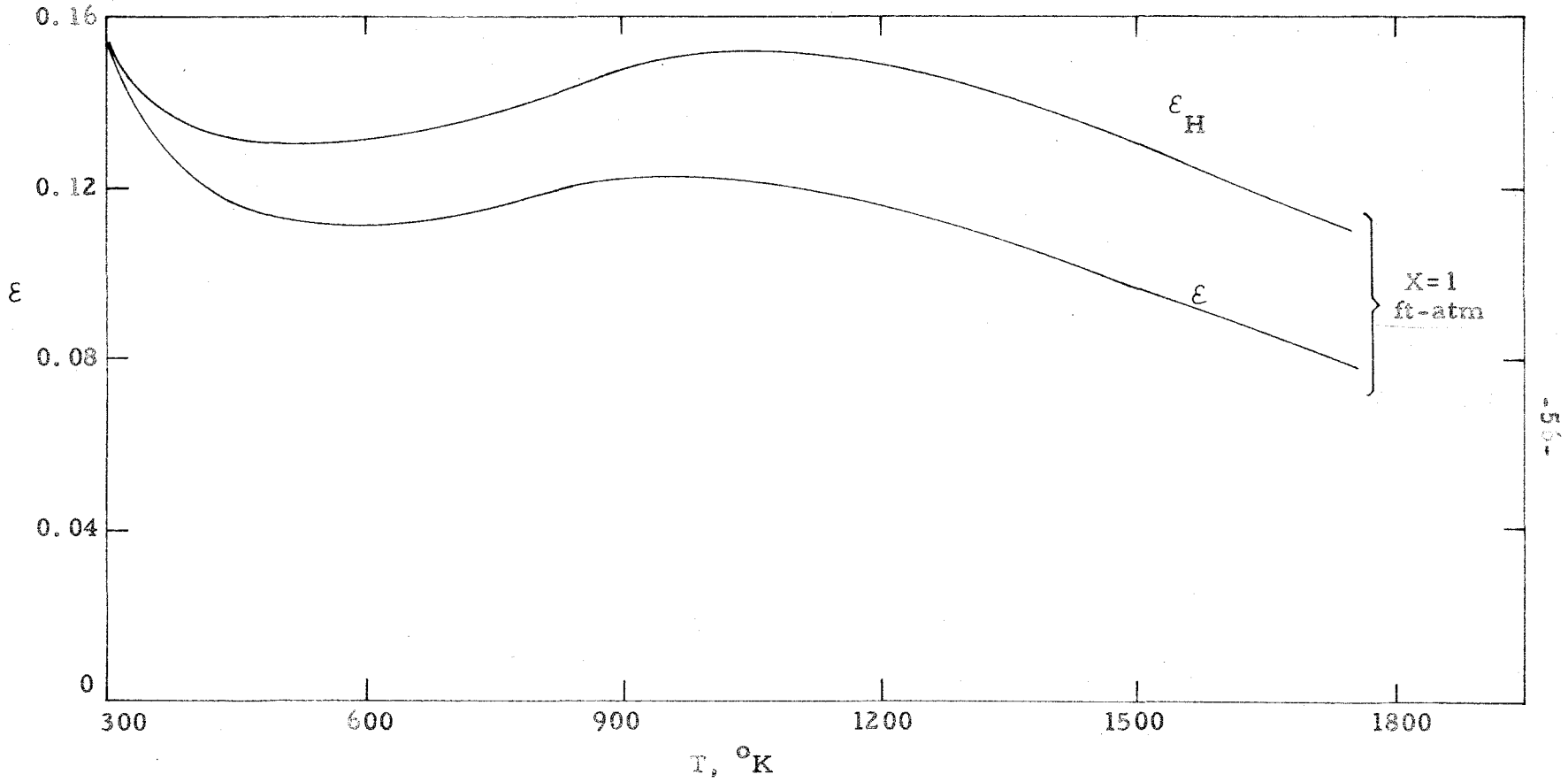

Fig. 21. Comparison between the emissivities ε and ε_H at 1 ft-atm; ε was calculated through use of the band multiplication model.

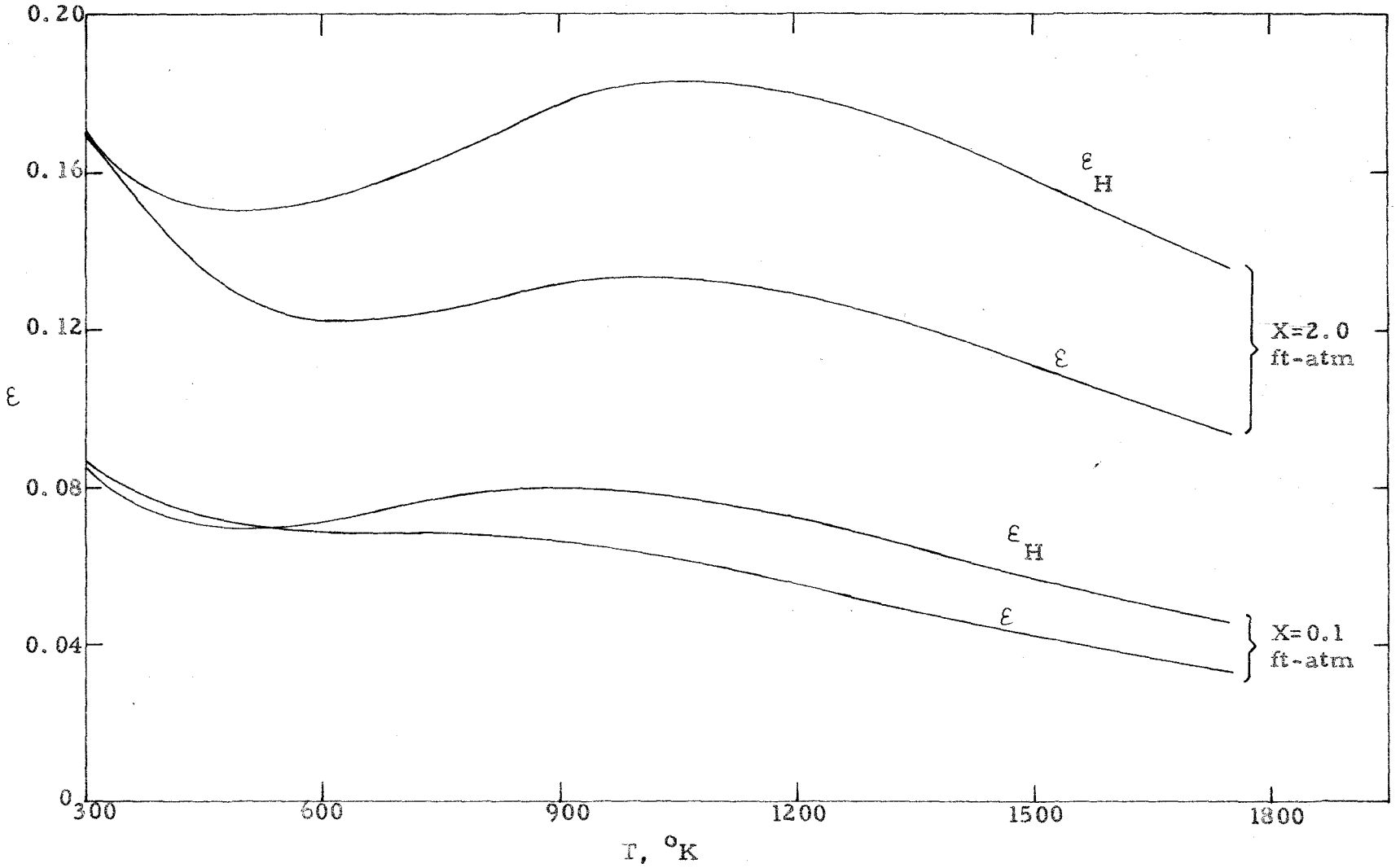

Fig. 22. Comparison between the emissivities ε and ε_H at 0.1 and 2.0 ft-atm; ε was calculated through use of the band multiplication model.

elevated temperatures. The contribution to the total emissivity (ε_5) may be separated into two parts: (1) ε_5' arising from transitions within the first four spectral regions and (2) ε_5'' arising from the remainder of the spectrum. The former contribution may be accounted for by replacing

$$a_1^*/(N_j-1) \quad \text{by} \quad \left\{a_j^* + \left[N_{5,j}(T)-N_{5,j}(300^\circ K)\right]\bar{a}_5\right\} \Big/ \left[N_j(T)-1\right]$$

where $N_{5,j}$ is the number of bands belonging to the weak-band continuum which exists in the interval $\Delta\omega_j$ and $\bar{a}_5$ is the mean intensity of these bands. In order to estimate this contribution we pick the mean band spacing to be δ_o, therefore setting $N_{\delta,j} = N_j$. The effect of ε_5' upon our previous results has been found to be negligibly small for reasonable choices of $\bar{a}_5$.

The second part of ε_5 may be written as

$$\varepsilon_5'' = \frac{0.3148}{T}\left\{\int_0^\infty \rho_\omega(1-e^{-\bar{P}_5 X})d\omega - \sum_j \int_{\Delta\omega_j} \rho_\omega (1-e^{-\bar{P}_5 X})d\omega\right\} = V(1-e^{-\bar{P}_5 X})$$

where $V = (1- \frac{0.3148}{T}\sum_j \rho_j \Delta\omega_j)$ and $\bar{P}_5 = \bar{a}_5/\delta_o$ is the average absorption coefficient of the weak-band continuum. Since V varies only from 0.83 to 0.78 at 1 ft-atm over the temperature range of these calculations, we use an average value of 0.81. Inspection of Fig. 21 indicates that $\varepsilon_H - \varepsilon$ for 1 ft-atm is about 0.03 at elevated temperatures; thus

$$\varepsilon_5'' = 0.81 X\ (\bar{a}_5/\delta_o). \tag{42}$$

In order to evaluate the temperature-dependent term ε_5'', we let $\bar{a}_5/\delta_o = \left[(\bar{a}_5)_o/\delta_o\right](T_o/T)f_o(T)$ where $(\bar{a}_5)_o$ is the average integrated intensity of a band at the reference temperature T_o and $f_o(T)$ represents any further temperature dependence of ε_5'' arising from changes in either $\bar{a}_5$ or δ_o. We obtain

$$\varepsilon_5'' = 1.0(\bar{a}_5)_o\,(T_o/T)\,f_o(T) \tag{43}$$

at 1 ft-atm. Permitting ε_5'' to be given by $\varepsilon_H - \varepsilon$ and choosing $(\bar{a}_5)_o$ as 10^{-3} cm^{-2}-atm^{-1}, we obtain a curve of $f_o(T)$ as a function of T and note that $f_o(T)$ varies from about 40 at 600°K to 175 at 1750°K. Similar results are obtained also at other optical depths. However, Eq. (42) requires that ε_5'' be a linear function of optical depth; this result is incorrect as may be seen from inspection of Figs. 21 and 22.

In order to attempt to account for the non-linear variation of $\varepsilon_H - \varepsilon$ with X, we modify our concept of the weak band continuum to one of a series of weak discrete bands spread over the spectrum at elevated temperatures. We now assume

$$\varepsilon_5 \equiv \varepsilon_H - \varepsilon = \frac{0.3148}{T} \sum_k \int_{\Delta\omega_k} \rho_\omega \left(1-e^{-\bar{P}_5 X}\right) d\omega$$

$$= \frac{0.3148}{T}\left(1-e^{-\bar{P}_5 X}\right) \Delta\omega_B \sum_k \rho_k \tag{44}$$

where the effective band width $\Delta\omega_B$ is less than the mean spacing of the weak bands. Defining $\beta_{X_1, X_2} = (\varepsilon_5)_{X_1}/(\varepsilon_5)_{X_2}$, we obtain

$$\beta_{X_1, X_2} = \frac{1-e^{-\bar{P}_5 X_1}}{1-e^{-\bar{P}_5 X_2}} \quad . \tag{45}$$

Since $\bar{P}_5 = \bar{\alpha}_5/\Delta\omega_B$ we may use calculated values of β_{X_1, X_2} to determine $\bar{\alpha}_5$. However, $\beta_{1.0,\,0.1}$ and $\beta_{2.0,\,0.1}$ both lead to unreasonably large values of $\bar{\alpha}_5$. Replacement of the box approximation band shape by the just-overlapping line profile does not alter the conclusions. More complicated descriptions of discrete weak band distribution also failed to yield the desired optical depth dependence together with reasonable values of integrated intensity.

IV. DISCUSSION OF RESULTS

A. Comparison with Experimental Data

Emissivity estimates by Edwards,[14] based directly on low-resolution spectral measurements of band absorptions at temperatures up to 1400°K and total pressures of 0.5 to 10 atm, are about 10% below the results of Hottel; adjustments to the same effective broadening agent reduces the discrepancy to about 5% for 300°K and optical depths of about 1 ft-atm. Edwards' results for the 2.7μ, 4.3μ, 9.4μ, 10.4μ, and 15μ bands are plotted in Fig. 23 as solid curves for X = 1 ft-atm; ε_1 corresponds to the contributions calculated by us from the 15, 10.4 and 9.4μ bands, ε_2(b) is the calculated emissivity of the 4.3μ bands, and ε_3(a) is the emissivity of the 2.7μ bands. Region 4 does not contribute in Edwards' work until optical depths larger than 1 ft-atm are achieved. Inspection of the curves in Fig. 23 shows agreement for our second and third regions,

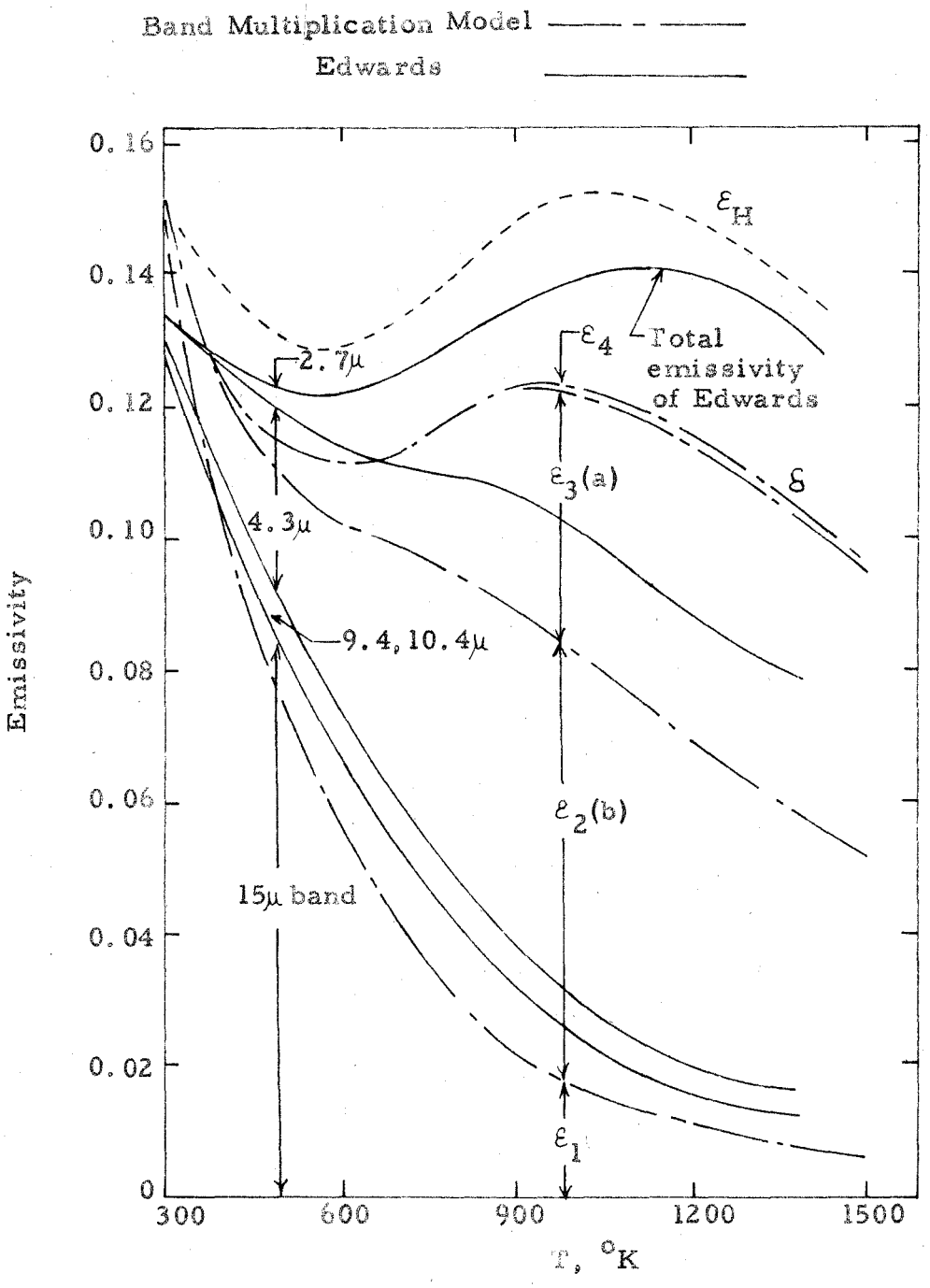

Fig. 23. Comparison of emissivity ε at 1 ft-atm (calculated through use of the band multiplication model) with emissivities obtained by Edwards[14] from band absorption measurements and with ε_H. Comparisons are also made between ε_1, ε_2(b), ε_3(a), ε_4 and the corresponding quantities estimated by Edwards from band-absorption measurements.

with ε_2(b) about 8% below and ε_3(a) about 2% above Edwards' empirical values at 1000°K, while ε_1 lies considerably below Edwards' experimental value. A part of this discrepancy arises because we considered the 9.4 and 10.4μ bands as weak adjuncts to the first spectral region. At 0.1 ft-atm, ε_1 agrees much more closely with Edwards' value but now ε_2(b) and ε_3(a) do not agree as well as before.

Comparison of the second and third region emissivities may be made with the experimental results of Tourin and Henry[15] at 1273°K and 0.384 and 0.0244 ft-atm for a total pressure p_T of 0.92 atm (see Table 7). Agreement of ε_2(b) with the corresponding experimental values

Table 7. Comparison of calculated emissivities at 1273°K with values determined experimentally by Tourin and Henry[15].

X ft-atm	ε_2(b)	Tourin and Henry's data for		ε_3(a)
		region 2	region 3	
0.384	0.0468	0.0532	0.0323	0.0277
.0244	.0292	.0296	.00283	.00242

is within 1% at the lower optical depth while the remaining three emissivities agree within 12 to 14%. The calculated values are too small in each case.

Values of ε_2(b) are compared with Plass' calculated results[8] up to 2400°K at 3.28 and 0.0328 ft-atm in Fig. 24. At 600°K we observe very good agreement but at elevated temperatures, ε_2(b) lies considerably above Plass' values. The experimental results of Tourin and Henry at 1200°K are also considerably larger than Plass' calculated

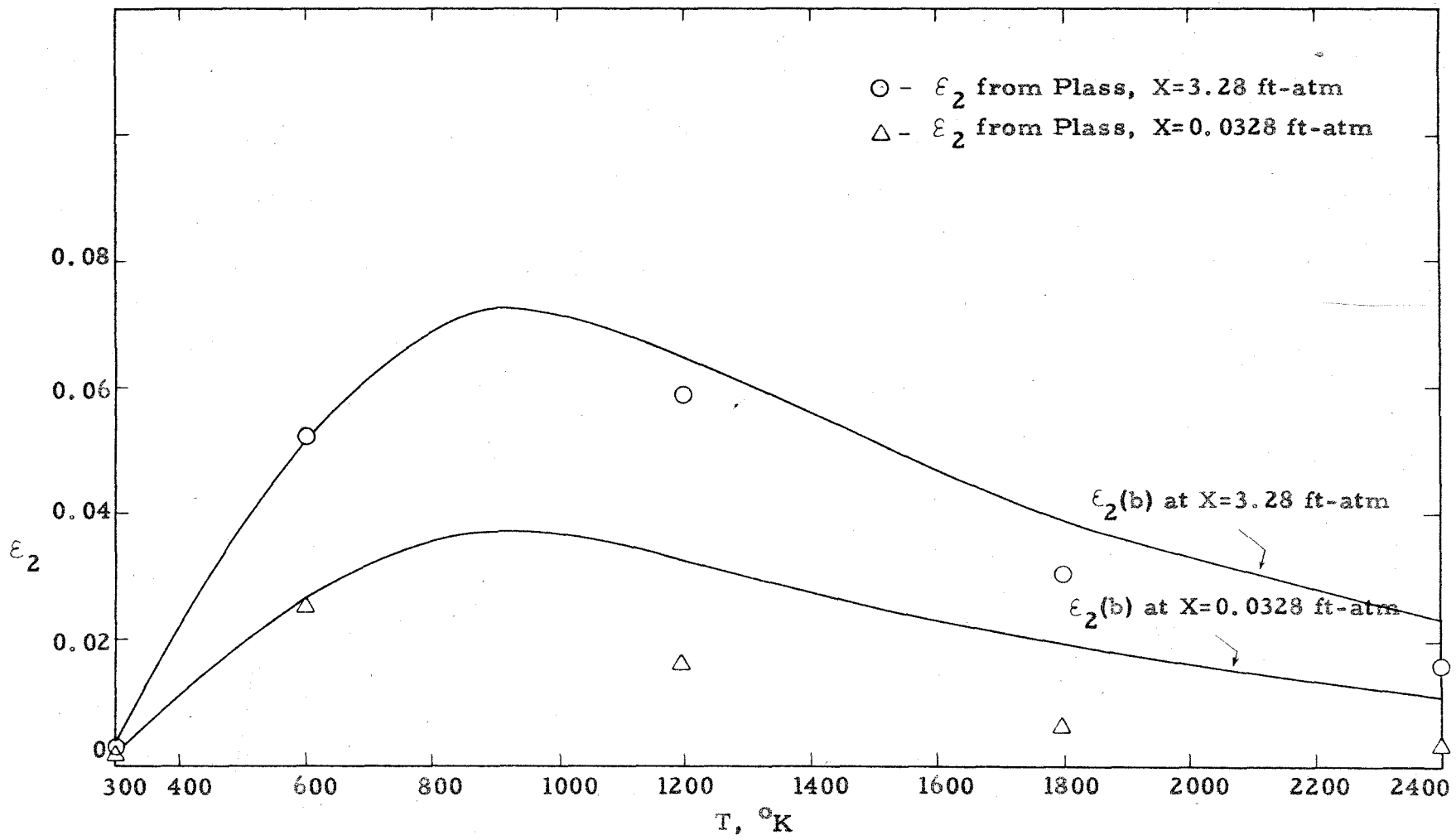

Fig. 24. Comparison of emissivities $\varepsilon_2(b)$ of the second region calculated by the band multiplication model with the results of Plass.[3], [11]

data; for small optical depths, Tourin and Henry observed data about 2.5 times larger than Plass' results. Experimental results obtained by Ferriso[16] in spectral measurements of rocket exhausts in the 4.3μ region at 1500 to 2100°K and low optical depths indicate emissivities that are roughly in agreement with our calculated values and with the measurements of Tourin and Henry.

B. Discussion of Rotational Band Structure

Our choice of the just-overlapping line description was motivated by the intense strengths of the fundamentals and by the reduction in complexity offered by a model that yields results which do not depend upon the line shapes. Furthermore, since a great many transitions become important at elevated temperatures, the spectrum may, in fact, be very rich and most of the lines overlap somewhat with other lines. This assumption is supported by the insensitivity of experimental absorption profiles to total pressures for pressures of about 1 atm or greater.[14],[15] The fact that our calculations agree reasonably well with experimental results indicates that our model is at least appropriate for the strong transitions. However, it is possible that discrepancies with ε_H arise from failure of the model for the weak bands for which the non-overlapping line model may be more appropriate. The influence of the weak bands on the just-overlapping line calculations is relatively small;* it is, however, larger for a non-overlapping line model.

---

* At 600°K and 2 ft-atm, ε_1 increases by only 8% if a_1^* is doubled; at 1500°K, the increase is 9%.

A discussion of the non-overlapping line model is given in Appendix 1. Previous calculation has shown that the total emissivity is greatly over-estimated at 300°K through use of this model for all bands (see Fig. 6). In order to ensure that we treat only the weak bands as non-overlapping, calculations of $\varepsilon_2(b)$ were performed at 900°K with $\Delta\omega_2 = 422\ cm^{-1}$ and $\delta_o = 24\ cm^{-1}$ using this model for all bands of region 2. At 1 ft-atm we obtain $\varepsilon_2(b) = 0.11$ while, at 0.384 ft-atm, $\varepsilon_2(b) = 0.078$. Inspection of Figs. 18, 19, and 24 show these values to be considerably too large. In fact, the value calculated by the non-overlapping line model at 0.384 ft-atm is larger than the value calculated by use of the just-overlapping line model at 3.28 ft-atm.

We thus conclude that an accurate fit to empirical data requires separate descriptions of the rotational structures of the strong and weak bands. An appropriate division would involve the calculation of the band absorptions for the fundamentals and for the strong bands at 3609 and 3716 cm^{-1} by the just-overlapping line model while the band absorption for the remaining bands of the first three regions* would be computed according to the non-overlapping line description. However, we must now introduce several new parameters into the program. If we treat the first three regions statistically, characterizing each by the relations

$$\Delta\omega_j(T) = \Delta\omega_j(300^\circ K) + (\delta_o/2)\sqrt{T} \qquad (46)$$

* Although no weak bands have been measured in region 3 at room temperature, we infer their existence at elevated temperatures from experimental spectral data.[14], [15]

and

$$a_j^* = (a_j^*)_o \, (300/T)^{\gamma} \, , \tag{47}$$

and assume that $\delta_1 = \delta_2 = \delta_3 = \delta_o$ and $b_c = (b_c)_o \, (300/T)^{\theta}$, we must pick nine parameters by fitting the calculated results to ε_H over a wide range of T and X. Three of these may be eliminated by choosing $\Delta\omega_j(300^{\circ}K)$ close to the values already found, i.e., $\Delta\omega_1 \simeq 200$ cm^{-1}, $\Delta\omega_2 \simeq 400$ cm^{-1}, and $\Delta\omega_3 \simeq 100$ cm^{-1}. Furthermore, the present value of δ_o (24 cm^{-1}) and values of $(a_j^*)_o$ obtained from Table 2 may be used for first iterations. A fruitful approach might involve determining $(a_j^*)_o$ and δ_o at 300°K while neglecting regions 2 and 3 as in the present work. Calculations may then be made at 600 and 900°K at small optical depths, neglecting a_3^*, and determining $(a_2^*)_o$, θ and γ. At 1500 and 1750°K, a_3^* is determined and the values for θ and γ are improved. Finally, the original estimates for $(a_1^*)_o$ and δ_o are improved as are the original values of $\Delta\omega_j(300^{\circ}K)$. If required, a weak band distribution could be included in the final correlation. The proposed numerical fit to Hottel's data is being performed by L. Gray.

CONCLUSION

Our calculations of CO_2 emissivities at elevated temperatures, using two parameters determined from room temperature emissivity measurements and a third parameter estimated from available spectral profiles, have been shown to agree within 30% or better with experimental data up to 1750°K and optical depths up to 2 ft-atm. At 600°K, the calculated emissivities agree with the measured values within at least

8%. We note that the H_2O emissivity correlation of Thomson* required five adjustable parameters to produce practically perfect agreement with high-temperature emissivity data. Strong multiplication of bands, introduced through a temperature-dependent mean band spacing and through a weak band distribution at elevated temperatures was discarded since these effects did not lead to significant improvement of results.

We note that the success of these calculations does not depend upon a fit to Hottel's data at 300°K since (a) we are able to calculate the total emissivity at 300°K with fair accuracy from spectroscopic data and (b) we are able to estimate the parameters required by our model directly from available spectroscopic information. The use of Hottel's data was adopted only as a convenience for this test calculation in order to provide a consistent check on our method of calculating emissivities at elevated temperatures.

---

* Ref. 7, Sections 11-17 to 11-20.

APPENDIX 1

The Non-Overlapping Line Model

The integrated intensity a of a band is given by

$$a = n \sum_{J} S_J \simeq n \int_0^{\infty} S_J dJ \tag{48}$$

where n = the number of branches of the band. As an approximate representation of the band shape, we use a slightly modified form of Eq. (14), viz.,

$$S_J = \frac{2ahcB_e}{nkT} J \; e^{-\frac{hcB_e}{kT} J^2} \tag{49}$$

where the factor n has been inserted in the denominator. We note that Eq. (14) is applicable to CO_2, whereas we now choose to develop this model for a molecule with every rotational line present and then specialize the results to CO_2.

For non-overlapping lines,

$$A_{band} = \int_{band} \left[1-e^{-P_\omega X}\right] d\omega = n \sum_J A_J \simeq n \int_0^{\infty} A_J \, dJ,$$

where

$$A_J = \int_{line\ J} \left[1-e^{-P_\omega X}\right] d\omega$$

and

$$S_J = \int_{line\ J} P_\omega d\omega \, .$$

General representations of the line absorption coefficient are available and the results of numerical calculations appear conveniently

on the curves of growth for spectral lines with combined Doppler and dispersion broadening.* In these curves $\left[\sqrt{\ell n 2}/2b_D\right] A_J$ is plotted as a function of P'X for various values of the damping parameter a; here b_D = Doppler half-width = $\sqrt{2kT\,\ell n 2/mc^2}\,\omega_J$, P' = maximum value of the absorption coefficient for a Doppler contour = $\sqrt{\ell n 2/\pi}\, S_J/b_D$, $a = \sqrt{\ell n 2}\,(b_N + b_C)/b_D$, b_N = natural half-width, and b_C = collision half-width.

The Doppler half-width is easily computed, whereas the natural half-width is negligibly small for our calculations. The collision half-width, for accurate results, should be measured under the conditions of interest since its temperature variation is often extremely complicated and since the half-width may vary considerably from line to line for a given band. In the absence of such detailed knowledge, we use a single measured value given at STP and extrapolate to the conditions of interest by using the factor $p/\sqrt{T}$ obtained from kinetic theory. Neglect of long-range forces causes this extrapolation to yield half-widths that are too small at elevated temperatures.

We use the following definitions:

$$u = \sqrt{\frac{hcB_e}{kT}}\ J,$$

$$\eta = 0.212\,\frac{aX}{nb_D}\sqrt{\frac{hcB_e\,\ell n 2}{\pi kT}},$$

$$H(\eta, a) = \int_0^\infty \frac{\sqrt{\ell n 2}}{2b_D}\, A_{J(u)}\, du$$

---

* See, for example, Ref. 7, Ch. 4.

Substitution of the new variables u, η, and P' into Eq. (49) yields

$$\eta u e^{-u^2} = 0.106 P'X. \tag{50}$$

We note that the integrand of $H(\eta, \underline{a})$ is the ordinate of the curve of growth and finally obtain

$$A_{band} = 2b_D n \sqrt{\frac{kT}{hcB_e \ell n 2}} H(\eta, \underline{a}). \tag{51}$$

The method of calculation is as follows: for a given temperature T, optical depth X, band integrated intensity α, and line J, we obtain a value of η; T and J yield u; u and η, in turn, give a value on the abscissa of the curve of growth through the use of Eq. (50); T and the total pressure lead to a value for $\underline{a}$ and this, together with the value on the abscissa, give us the corresponding ordinate of the curve of growth. We then plot this ordinate as a function of u, considering as many lines as are required for an accurate result, and determine the area under the curve to obtain a value of $H(\eta, \underline{a})$. Asymptotic relations for $H(\eta, 0)$ for $\eta \ll 1$ and $\eta \gg 1$ are available, as are also calculated results for $\underline{a} = 0.05$ and 0.125 with η varying up to 12.*

The appropriate values of η and $\underline{a}$ for use with these computations of CO_2 emissivity are much larger than those already available, requiring calculations for values of $\underline{a}$ ranging from approximately 8 to 30 and for η from 10^{-2} to 10^5. The values of the damping parameter correspond to those obtained by using $b_C = 0.064$ cm^{-1} at STP;[11] ω assumed the values 2349, 2285, and 2012 cm^{-1}; and T = 300, 600 and 900°K. The results appear in Table 8.

---

* Ref. 7, pg. 408.

Table 8. $H(\eta, \underline{a})$ calculated from the curves of growth.*

$\underline{a}$	η	$H(\eta, \underline{a})$
28.3	0.16	0.70
	1.60	6.38
	3.20	12.9
	8.00	30.2
24.9	0.0915×10^3	1.71×10^2
	.915	6.24
	1.83	8.94
	4.57	14.3
24.3	0.0800×10^5	0.189×10^4
	.800	.590
	1.60	.843
	4.00	1.33
14.2	0.0405	0.18
	.405	1.61
	.810	3.23
	2.02	8.20
12.5	0.0229×10^3	0.555×10^2
	.229	2.18
	.457	3.17
	1.14	5.02
12.1	0.0200×10^5	0.657×10^3
	.200	2.07
	.400	2.93
	1.00	4.65
9.59	0.0181	0.07
	.181	.73
	.363	1.47
	.906	3.61
8.31	0.102×10^2	30
	1.02	127
	2.03	182
	5.08	293
8.08	0.0889×10^4	0.357×10^3
	.889	1.14
	1.78	1.61
	4.45	2.55

* The numerical computations were carried out by L. Gray.

For very large values of log(10.6 P'X), the slopes of the curves of growth on a log-log plot are 0.5 while for very small values on the abscissa the slopes are unity. A slope of approximately 0.5 is achieved for log (10.6 P'X) > 3 and $\underline{a} > 0.5$ whereas the slope is approximately 1.0 for log (10.6 P'X) < 2 and $\underline{a} > 10$. Since log (10.6 P'X) $\propto \eta$, we expect $H(\eta, \underline{a})$ to be proportional to $\sqrt{\eta}$ for large η and to η for small η with $\underline{a}$ sufficiently large in each case. We find from Table 8, for example, that $H = 21.0\sqrt{\eta}$ within 1% for $\underline{a} = 24.3$ with $\eta > 8 \times 10^3$ and $H = 3.99\eta$ within 3% for $\underline{a} = 9.59$ with $\eta < 0.906$.

For application to CO_2, we modify our results by replacing Eq. (49) by Eq. (14). We obtain the result that Eq. (50) must be replaced by

$$\eta u\, e^{-u^2} = 0.053\ P'X\ . \tag{52}$$

We use our previous calculations by defining η^* to be the value of the parameter calculated correctly for CO_2 and note that $\eta^* = \eta/2$. Finally, Eq. (51) is replaced by

$$A_{band} = 2b_D \sqrt{\frac{kT}{hcB_e \ell n 2}}\ H(\eta^*, \underline{a}). \tag{53}$$

PART 2

SHOCK TUBE f-NUMBER MEASUREMENT FOR OH

I. INTRODUCTION

The shock tube has been used by a number of investigators in emission and absorption experiments for the determination of f-numbers.[17] The purpose of this experiment is the determination of the f-number for the (0, 0) vibrational band of the $^2\sum \longrightarrow {}^2\prod$ OH electronic transitions. This f-number has been measured previously by Oldenberg and Rieke[18] and by Dyne[19] for OH produced at equilibrium in furnaces and by Carrington[20] for OH in flames. The shock tube permits the attainment of temperatures in excess of those achieved by the furnaces and flames, with correspondingly increased accuracy in the estimation of equilibrium OH concentrations.

In this experiment, emission from OH formed behind the reflected shock was observed in an axial direction within a very small solid angle. We thus observed the radiation passing through the end plane of a cylinder of test gas the length of which grows linearly with time for constant reflected shock velocity. The experimental conditions were chosen in such a way that no OH emission could be detected from the gas behind the incident shock wave. The radiation was monitored by a 1P28 photomultiplier used in conjunction with a Perkin-Elmer quartz monochromator.

Since the length of the column of test gas grows linearly with time, we are able to determine whether the gas is transparent or self-absorbed.

Theoretical estimates of transparency are possible from available information but are often inconclusive because of the absence of accurate data for the line widths. We observed that the emission intensity was essentially a linear function of time after shock reflection, thus indicating that the radiating region was transparent. In order to determine the f-number, an absolute intensity calibration was made by imaging a source of known intensity at the shock tube exit port. In addition, relative intensity calibrations were performed immediately following each run. All tests were performed with H_2O-Ar mixtures. The gas composition was measured for each test and about 1% H_2O was usually found to be present. When the test-gases do not radiate in the linear portion of the curves of growth, the reduction of the data is more difficult. However, an absolute intensity calibration is not required in this case since each run corresponds to an infinite number of multiple-path experiments.

II. EXPERIMENTAL APPARATUS

A. The Shock Tube

The shock tube used for these experiments (see Figs. 25 and 26) has been constructed of Shelby seamless steel tubing of 3 inches internal diameter and 1/4 inch wall thickness.* The low-pressure section is either 78-5/8 or 66-5/8 inches long, depending upon the experimental testing time required. The high-pressure section is 60 inches long.

---

* This tube is a modification of one constructed under Contract No. AF 18(603)-2, Air Force Office of Scientific Research, Air Research and Development Command.

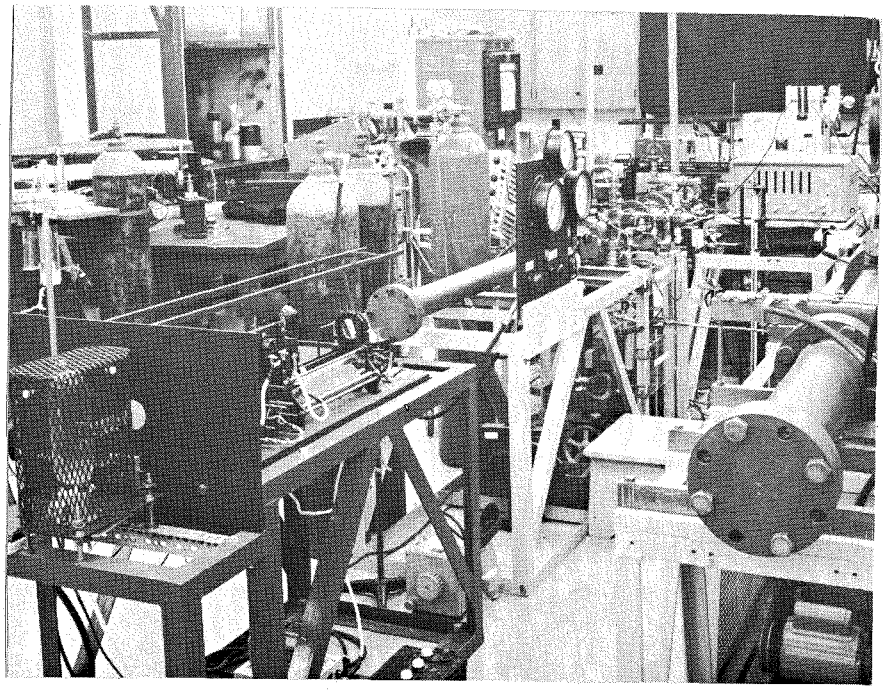

Fig. 25. Overall view of shock tube (high-pressure section is at the center of the picture) and calibration bench (left foreground).

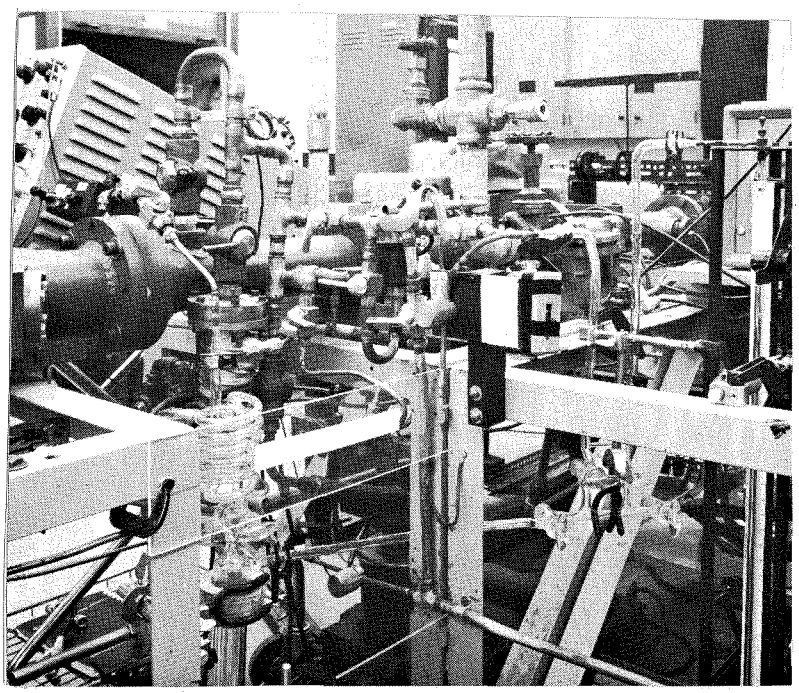

Fig. 26. Detail of shock tube near diaphragm position. Portions of the gas-handling manifold and concentration analysis system are shown (compare the schematic diagram shown in Fig. 27).

The length of the high-pressure section has been designed in such a way as to ensure that the reflected rarefaction waves do not reach the observation section before the experiments are completed. The tube was painted with red lead primer to resist rusting.

All mating flanges are joined with O-ring seals, using Dow-Corning silicone vacuum grease. The end plate of the tube is removable from a threaded mount and contains a 3/4 inch diameter, 3/8 inch thick, Linde synthetic sapphire (Al_2O_3) window. The window is cemented into a recess with Epibond No. 104 furane resin so that its surface is flush with the end wall of the shock tube. Sapphire window ports in the low-pressure section permit observations normal to the tube axis. Velocity measurements were made by determining the shock transit time between thin film heat gages.[21] These were constructed by sputtering thin layers of platinum onto glass blocks that were then cemented with furane resin into ports inserted into the shock tube wall at locations 24 inches apart.

The diaphragm section was secured with four heavy-duty bolts. It was seated with opposing O-rings on both sides. Copper diaphragms, scored with an "x" for efficient opening under pressure, were used in early operation of the equipment. A small ridge milled into the inside surface of the tube directly downstream of the flange of the diaphragm section aided in preventing petals of copper from being thrown downstream with subsequent damage to heat gages and windows. The tube was cleaned with acetone-soaked cloths after each run.

In subsequent experiments, described in Section III A, DuPont mylar diaphragms were used. With mylar, ultraviolet impurity radiation was greatly diminished. Furthermore, experimental scatter of measured

incident shock velocities (u_s) was reduced to about 1/2%, which is the accuracy with which the low-pressure section could be loaded with test gas. No scoring of the mylar was required. Available thicknesses range from 0.001 to 0.010 inch and several pieces may be stacked together. Changes in shock velocity were obtained by changing the thickness of the mylar diaphragms. It was also found that cleaning between runs could be accomplished by flushing the tube with high-pressure, dry nitrogen gas discharged through a hose directed at the tube walls at about 100 psi pressure. Use of mylar diaphragms, together with this cleaning procedure in several tube firings, produced "clean" interior conditions for these experiments.

B. The Gas-Handling System

A detail of part of the gas-handling system appears in Fig. 26, and a schematic diagram of the system is shown in Fig. 27. All lines were constructed of refrigeration copper tubing except for the glass concentration analysis system (cf. Section C), and the glass system for the introduction of H_2O vapor.

1. Low-pressure section

For the low-pressure section, Mueller Brass Co. solder fittings and $ZnCl_2$ flux were used. All valves not intended for metering were Circle Seal plug valves, with Hoke steel bellows valves used for the required metering stations.

The apparatus is evacuated through use of a Consolidated Vacuum Corp. MCF-60 oil diffusion pump (using Octoil pump fluid) and a Kinney KC-8 mechanical forepump discharging into a chemical hood. The

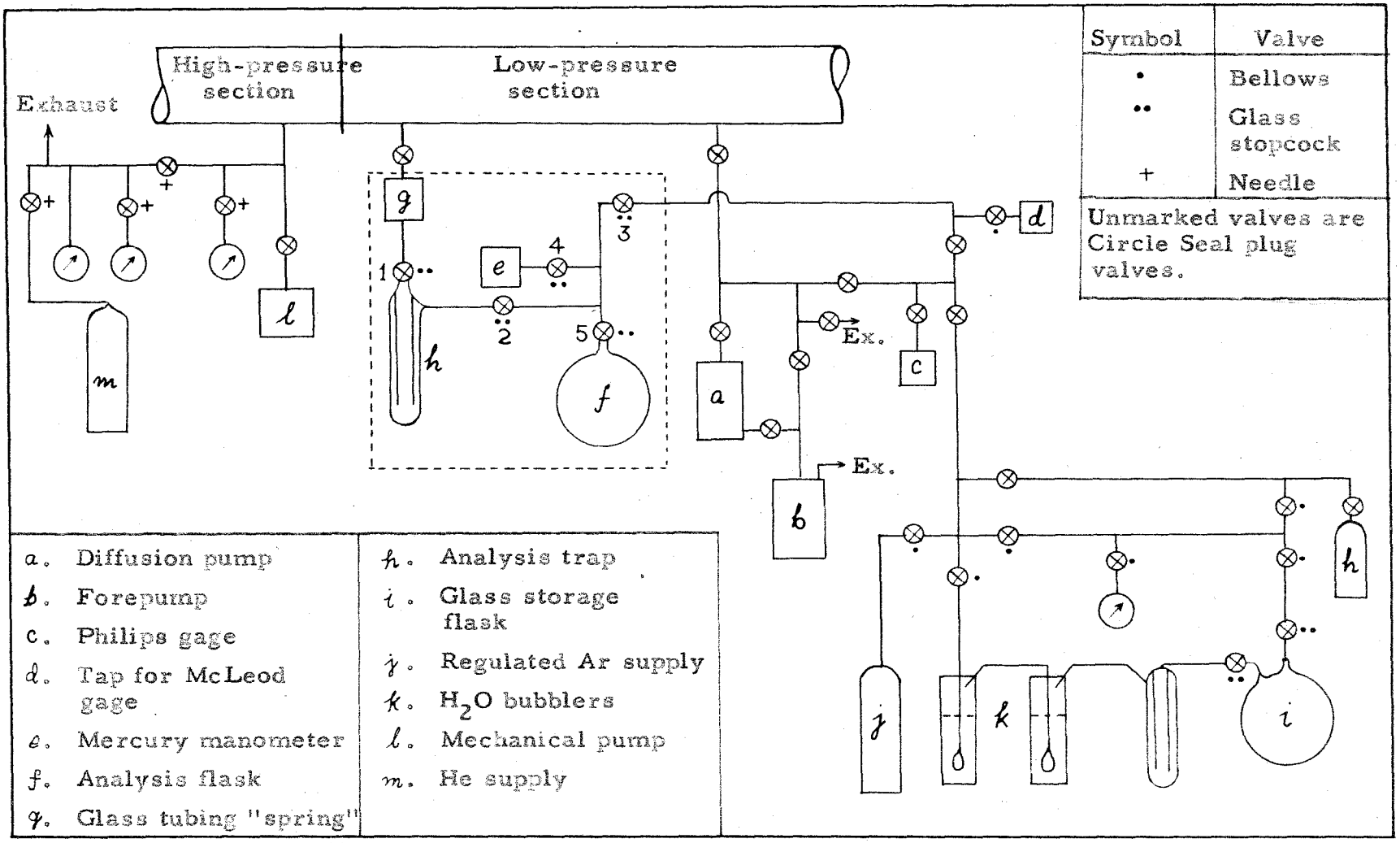

Fig. 27. Schematic of gas-handling and concentration analysis systems.

manifold is connected to the top of the shock tube through a U-shaped line in order to prevent diaphragm material from dropping in. The length of the direct line from the diffusion pump to the tube was minimized in order to provide efficient pumping speeds. It was constructed of 3/4 inch diameter copper tubing that corresponds to the largest diameter valve readily available for use at the shock tube. This valve must not only be vacuum-tight, but must also be able to withstand the high pressures present after the diaphragm is ruptured. A 3/4 inch Circle Seal plug valve was selected for this purpose and another used directly next to the diffusion pump. The valves leading back to the forepump were of 1/2 inch diameter and the remaining ones in the system were either 1/2 or 1/4 inch in diameter. The forepump was isolated mechanically from the rest of the system through use of American Brass Co. flexible metal lines as vibration eliminators.

Test gas was produced by bubbling Linde Ar (99.997% pure) slowly through H_2O contained in two chemical bubblers connected in series with ball and socket joints. All glass seals were lubricated with Apiezon N vacuum grease. The bubblers were connected to a 3 liter storage flask and to a steel mixing bottle constructed of a Norris-Thermador CO_2 cylinder into which were placed a quantity of glass beads. The steel bottle was attached to the system through a flexible metal line, permitting gas mixing by shaking. In order to prevent any surface contamination by rust, test gas was never permitted to remain longer than a few hours in the bottle. The chemical bubblers and associated glassware were always filled to a total pressure of 1 atm of Ar when not in use in

order to prevent air leaks. Boiled water was initially put into the bubblers and the system was evacuated with the forepump through a liquid nitrogen trap until the water in the trap became frozen solid. Pressures in this system were monitored with a vacuum-to-2 atm. Ashcroft test gage.

A Consolidated Vacuum Corp. type PHG-09 Philips Gage was used for high vacuum measurements and was calibrated against a McLeod Gage. The entire apparatus could be evacuated to approximately 5×10^{-5} mm of Hg with a leak rate of about 0.02μ of Hg/min. For experimental runs, a vacuum of less than 10^{-3} mm of Hg with a leak rate of about 1μ of Hg/min was considered satisfactory.

2. High-pressure section

The driver gas for these experiments (He) was supplied from 2000 psi cylinders connected to the manifold through Parker high-pressure flexible hose. The shock tube was also connected to the manifold through a section of this hose. Parker high-pressure flare fittings were used throughout in conjunction with Grove and Circle Seal O-ring seat needle valves and a Hoke needle valve. A Circle Seal plug valve connected the manifold to a Welch Duo-Seal mechanical pump. High pressures were read on either a zero-to-800 psi or a zero-to-200 psi Ashcroft Duragauge. Low pressures were read on a zero-to-1 atm Ashcroft gage. Since the shock velocity was measured electronically for each run, measurements of the driver gas pressure (p_4) were not required. However, the pressure measurements were performed in order to provide an auxiliary measurement in case of failure of triggering of the electronic

counter used for velocity measurements. In practice, the pressure in the shock tube was recorded after completion of the run for each run and plotted as a function of the measured shock speed (u_s). Actually the velocity measuring system failed to function only once during the course of the shock tube experiments.

C. Concentration Analysis

Because of strong adsorption of water vapor on the metallic walls, it was found necessary to determine the test-gas composition for each run. This determination was performed by admitting test-gas to the shock tube from the manifold while simultaneously withdrawing a sample from another tap in the tube. The initial test-gas pressure (p_1) was recorded on a Wallace and Tiernan type FA 135 precision Hg manometer, which could be read to the nearest 0.1 mm of Hg through use of a travelling telescope.

The analysis system functions by freezing the H_2O vapor from the test gas sample as it passes through the liquid-nitrogen trap beneath valve 1 of Fig. 27. This sample, which is now pure Ar, passes on to the 3 liter flask beyond valve 5, registering p_1 (the initial shock tube downstream pressure) on the Hg manometer. Valve 3 is closed during analysis, except to provide access to the pumping system when required. After equilibration of pressures, the shock tube valves and valve 1 are closed and the run performed. Immediately after the run, valve 5 is shut off and the liquid-nitrogen trap and manometer are evacuated. Next valve 3 is closed and the liquid-nitrogen Dewar removed, permitting the frozen H_2O to evaporate. We therefore obtain a sensitive indication of

test-gas composition by freezing the H_2O vapor from a relatively large sample and re-evaporating it into a relatively small volume. Calibration of the volume ratio involved shows that the gas is re-evaporated into a volume 0.0611 times the initial sample volume. This favorable ratio is attained by minimizing the space between the inner and outer trap tubes and by filling the inner tube with glass rods. Computation of the mole percentage of H_2O vapor present in the test-gas is made through use of the relation

$$\% \, H_2O = \frac{0.0611 \, p_1'}{p_1 + 0.0611 p_1'} \, ,$$

where p_1' is the manometer reading of the re-evaporated H_2O pressure.

A check on the analysis system was performed by analyzing a 1% CO_2-99% Ar mixture (measured by the Wallace and Tiernan manometer). The composition was determined with an accuracy of better than 1%.

D. Electronic Equipment

1. Shock velocity measurements

The thin film heat gages discussed in Section A permit the measurement of u_s by triggering a Berkeley Model 7360 counter with a time resolution of 1μ sec. The step pulse signal at the heat gages is about one millivolt and is amplified by identical Technology Instrument Co. Type 500 A 1000 gain wide-band amplifiers. These signals are attenuated by a factor of 10 at the counter inputs for greater stability of operation of the counter. The shock velocity measurement equipment is shown schematically in Fig. 28. Considering the transit time of an average shock ($u_s \simeq 1.3$ mm/μsec) past a gage (width $\simeq 3/4$ mm) to be about 0.6μ sec, the total error in shock velocity measurement is less than 1/2%.

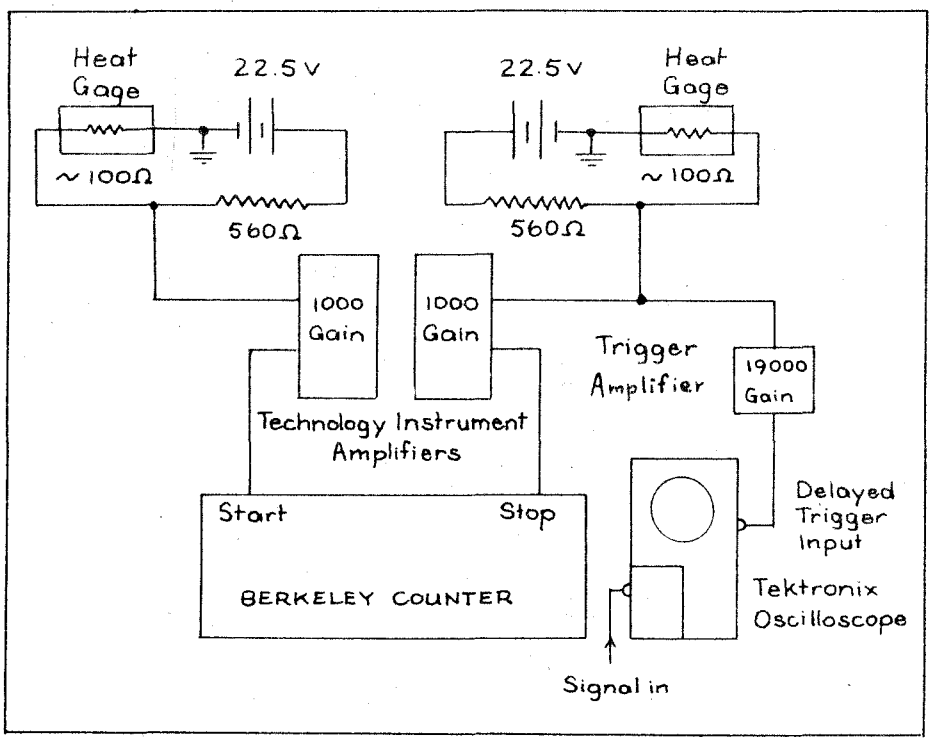

Fig. 28. Block diagram of shock tube electronic instrumentation used for shock velocity measurements and for triggering of the oscilloscope.

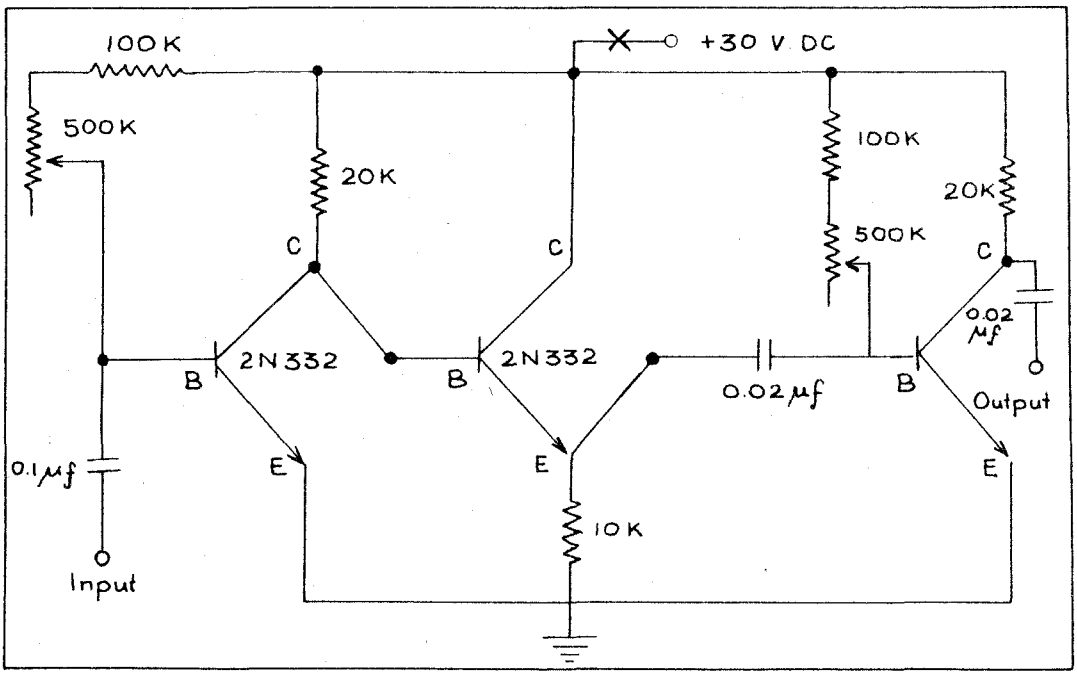

Fig. 29. Transistorized trigger amplifier.

2. Oscilloscope triggering and data recording

Experimental measurements of radiant intensity as a function of time were recorded on either a Tektronix Type 535 single-beam or Type 551 dual-beam oscilloscope through use of Polaroid transparency film and a DuMont oscilloscope camera. Most quantitative runs were performed on the Type 535 oscilloscope in order to use its built-in delay line to obtain high-speed delayed sweeps with correspondingly detailed results. The dual-beam oscilloscope was used to record simultaneously the output signal with high and low gains. All runs were performed with either Tektronix Type D or Type 53/54B plug-in preamplifiers.

The oscilloscope was triggered by a spike pulse from a transistorized trigger amplifier (see Fig. 29) which was fed by the step pulse output of the second heat gage. The amplifier voltage gain was measured to be about 19,000. The amplifier time constant τ, defined to be $1-(1/e) \simeq 2/3$ of the time required for the amplifier to respond to a step-pulse input, was found to be about 4μ sec. The time constant was determined by using the square-wave calibrator output of the oscilloscope as trigger amplifier input. Traces of the calibrator output and resultant trigger amplifier signal appear in Fig. 30. Use of this method for oscilloscope triggering was found to be very reliable.

Preliminary runs were performed using a step-function output of several volts from the Berkeley counter as oscilloscope trigger input. This method was found to be less satisfactory than the above-mentioned one.

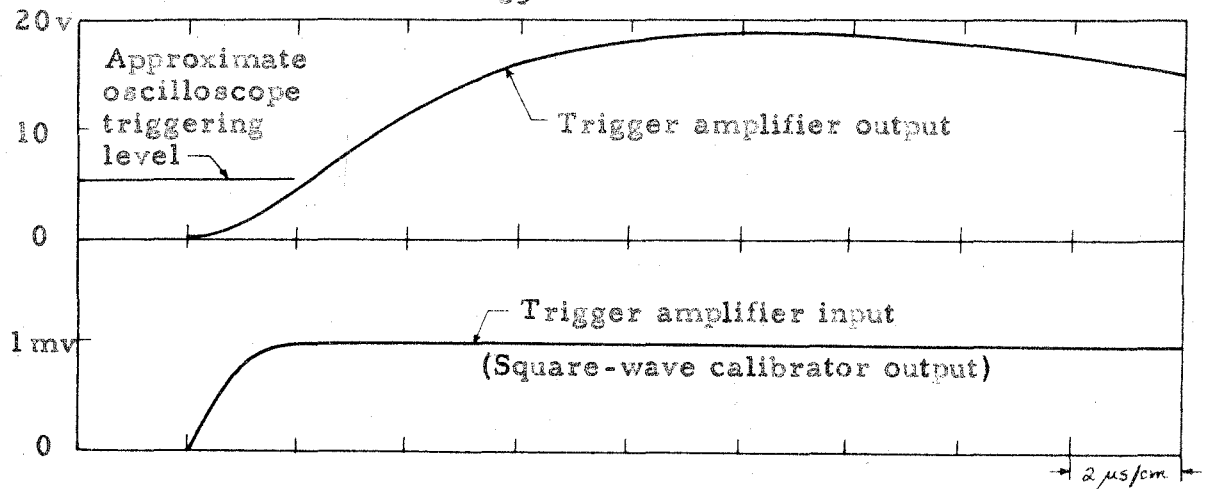

Fig. 30. Oscilloscope traces used in the determination of the time constant τ and the gain of the trigger amplifier.

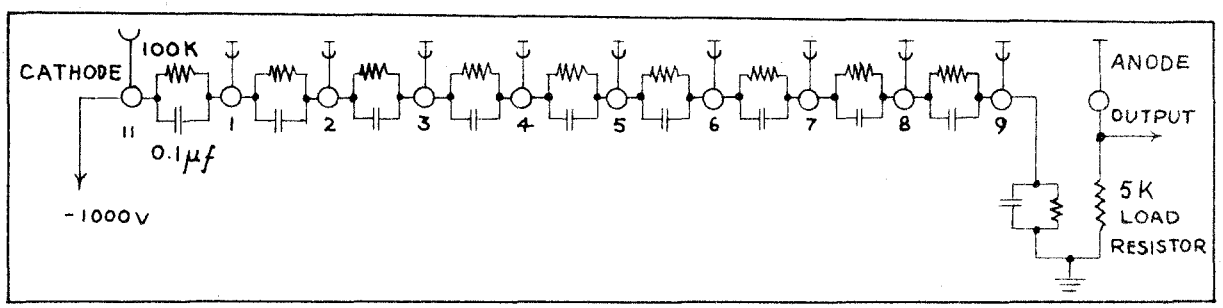

Fig. 31. Photomultiplier power supply.

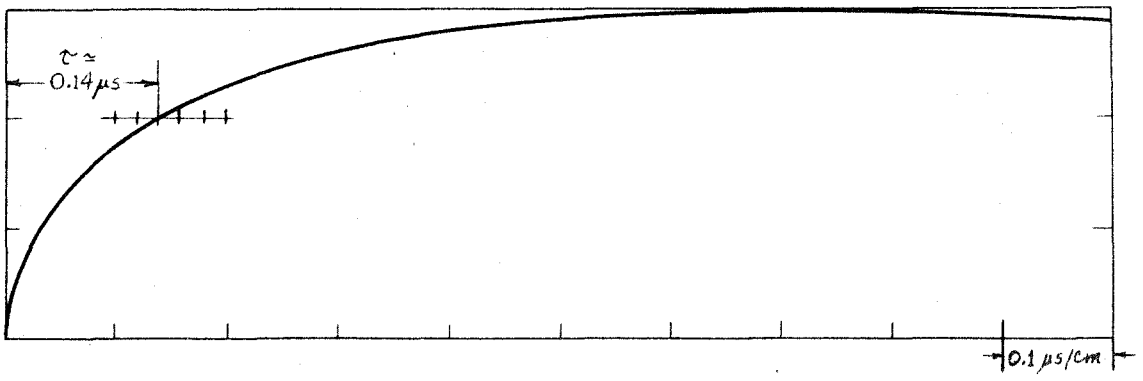

Fig. 32. Oscilloscope trace of photomultiplier output for a step function light input, as obtained in the "cathode ray tube" method for the determination of τ for the photomultiplier circuits.

3. Photomultiplier power supply

The photomultiplier power supply circuit that was found to give satisfactory time response for a rapidly varying radiative signal is shown in Fig. 31. The time constant introduced through use of this power supply was measured on the oscilloscope (i.e., cathode-ray tube or CRT) method. In this method, an oscilloscope is used as a pulse light source. The cathode-ray tube is masked off except for a small opening. The sweep traverses this opening rapidly and provides a step pulse of radiation. By placing the photomultiplier close to this light source and by recording its output signal on a second oscilloscope, we obtain the time constant of the electronic circuitry associated with the tube. For a 53/54 B plug-in preamplifier and the coaxial cable (RG-62/U) used in these experiments, τ was found to be about 0.14μ sec (see Fig. 32). This measurement was performed using a Tektronix 535 oscilloscope as light source with a 1.5 mm square aperture and source sweep speed of 0.1μ sec/cm. Thus, the source beam traversed the aperture in about 0.015μ sec or about 1/10 the value of the measured time constant.

The high voltage was supplied by a highly regulated power supply (Model 710-PR) built by the Electric Eye Equipment Co. (formerly Furst Electronics, Inc.) for the Perkin-Elmer Corp. Linearity of the photomultiplier output with changes in incident light intensity was checked for the photomultiplier currents used.

4. Experimental time constant

A 53/54 B plug-in preamplifier used with a Type 535 oscilloscope has a bandwidth extending to 9 Mc, or a time constant of $1/\left[2\pi x \text{ (frequency)}\right]$

$\simeq 0.02\,\mu$ sec. However, the most sensitive gain setting is 5mv/cm. In order to obtain measurements at 1 and 2 mv/cm, a Type D plug-in preamplifier was used. At 1 mv/cm gain its bandwidth extends to 0.35 Mc resulting in the value $\tau \simeq 0.45\mu$ sec. At 2 mv/cm gain, the bandwidth extends to 0.45 Mc resulting in $\tau \simeq 0.35\mu$ sec. These time constants exceed that of the photomultiplier power supply by more than an order of magnitude and represent the limiting time response. For the experiments performed, this time response is entirely adequate.

E. Exit Optics for the Shock Tube

A schematic diagram of the exit optics is drawn in Fig. 33 and a photograph is shown in Fig. 34. The axial exit port of the shock tube contains a sapphire window, the aperture of which is limited by a small ring of the resin used for cementing. The diameter of this aperture is approximately 10.4 mm. The window was fabricated by Linde Air Products Co. and has a transmission of about 82%[22] at the wavelengths of interest in this experiment ($\sim$3100 A). The exact value of this transmission is not required for reduction of the data since both the calibration radiation and the radiation emitted by the OH radicals pass through the window. Variation in the transmission over the wavelength interval of our experiments is too small to have any effect upon the results.

The reflectivity of the front-surface aluminized mirrors is about 82% at 3100 A and varies by less than one percent from 2600 to 3200 A.[23] The quartz lenses were all made of General Electric clear fused quartz (type 101). The transmission of one cm samples of this material is about

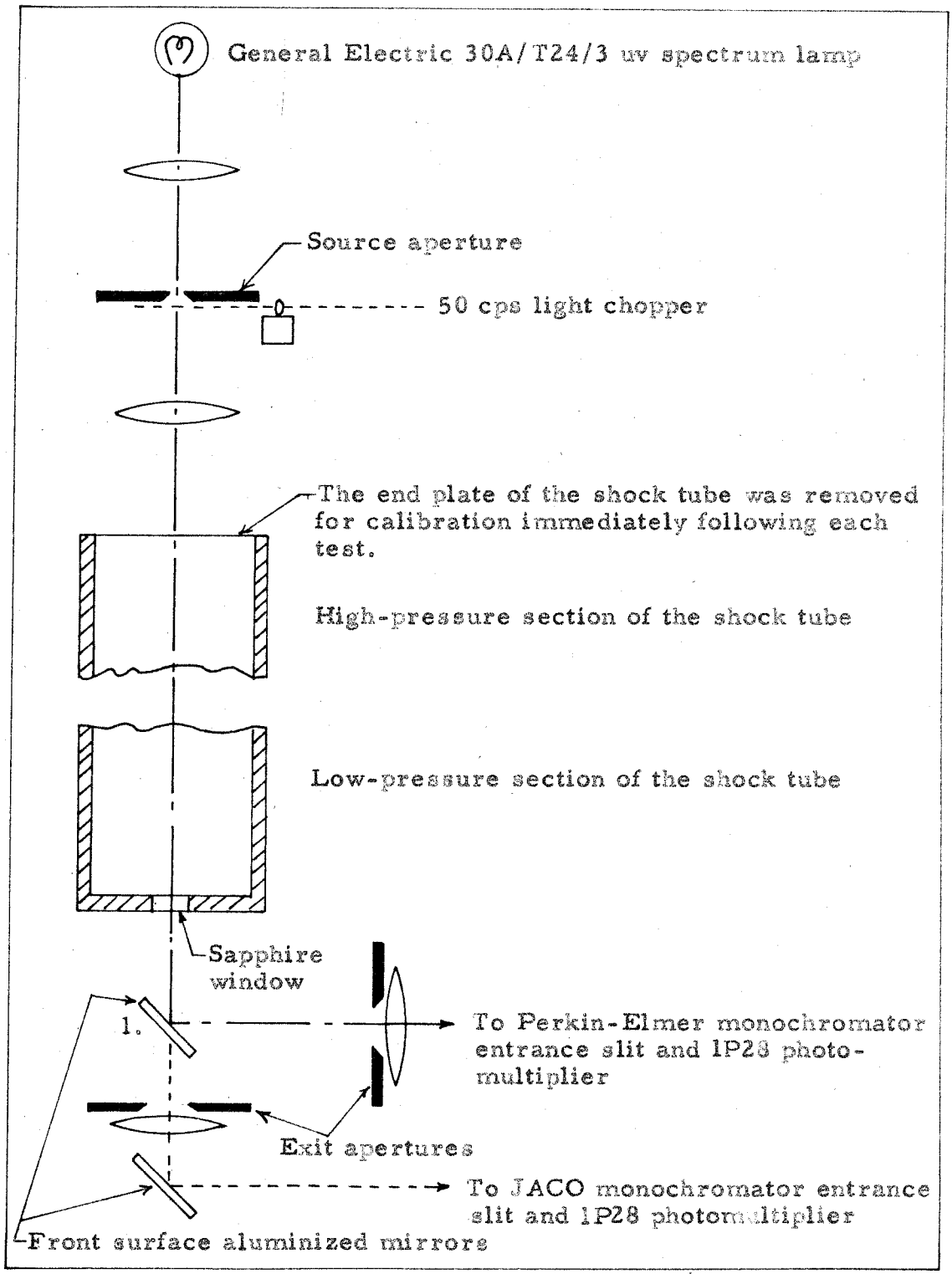

Fig. 33. Schematic diagram of calibration optics and shock tube exit optics. All lenses are made of quartz. Mirror 1 is either removed or displaced in order to use the JACO instrument.

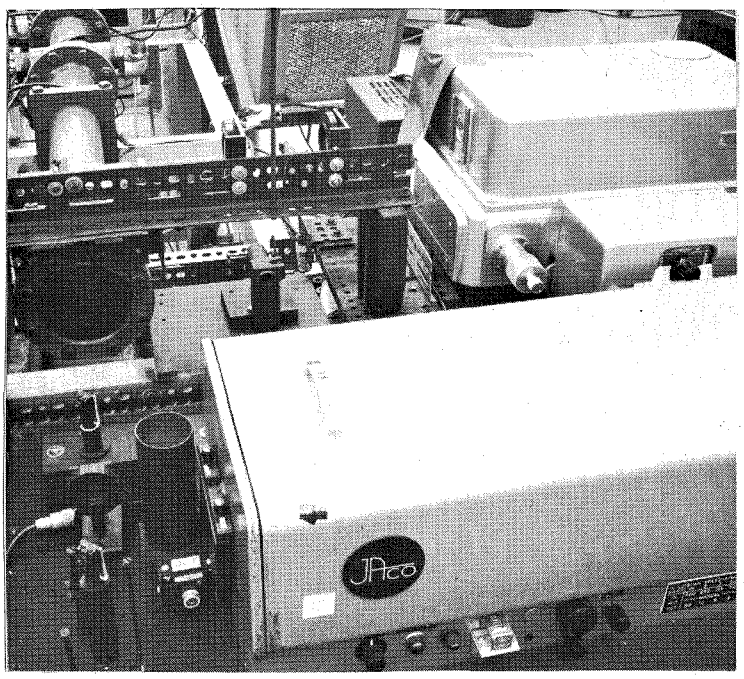

Fig. 34. Shock tube exit optics (compare the schematic diagrams shown in Figs. 33 and 46).

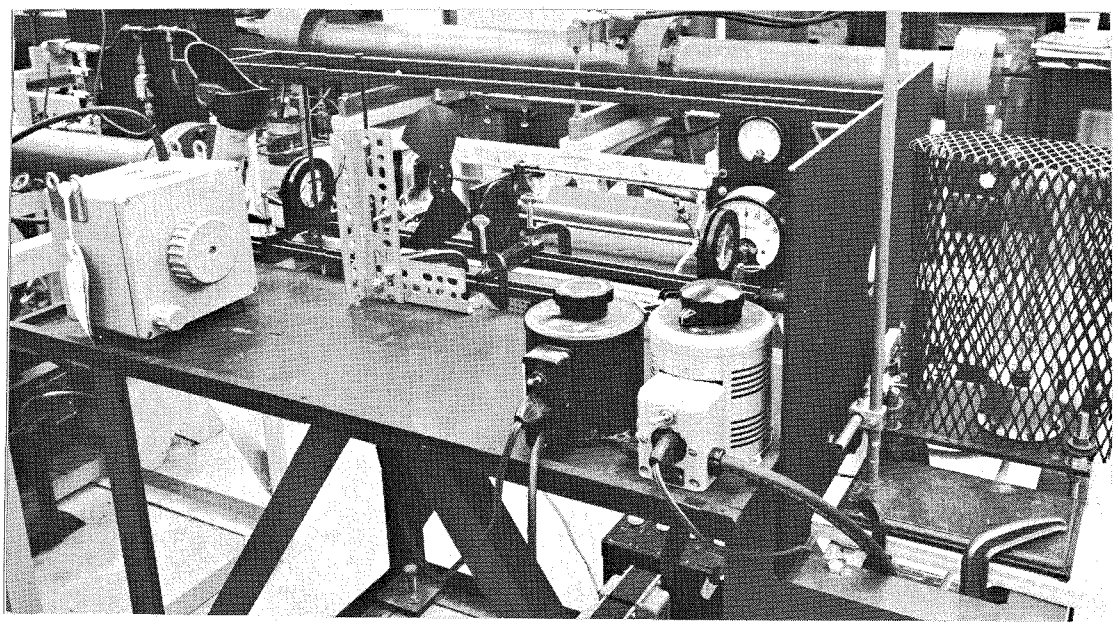

Fig. 35. Absolute intensity calibration bench (compare the schematic diagrams shown in Figs. 33 and 46).

99.8%, not including surface reflection losses,[24] with negligible variation over the experimental wavelength range.

All quantitative experiments were performed using the monochromator from a Perkin-Elmer Model 13 Spectrophotometer. This device is a single pass Littrow instrument which was used with a fused quartz prism as dispersing element. The dispersion of this prism was obtained from a Perkin-Elmer publication.[25] Preliminary experiments were performed using a Jarrell-Ash (JACO) Model 8200 1/2 meter Ebert monochromator. A 1200 lines/mm grating used in the first order produces a dispersion of 16 A/mm at the exit slit. Both monochromators were calibrated spectrally through use of a low-pressure Hanovia Mercury Lamp, No. 36595, Type SH (quartz envelope).

The exit system solid angle ($\Delta\Omega_E$) used for the quantitative runs is 3.40×10^{-5} steradians. This small angle resulted in imaging and recording the hot gas radiation from a volume practically equal to a column of cross-sectional area equal to the exit port area.

A selected RCA 1P28 photomultiplier detector was used for all experiments, with a supply voltage of 1000 volts between the anode and cathode. The spectral response of this tube is classified as S-5, indicating a wavelength of maximum spectral response of approximately 3400 A with a maximum response variation of about 15% from 2900 to 4100 A. The variation of spectral response with wavelength is small in the region of interest for our experiments.

F. Calibration Optics

An absolute intensity calibration of the apparatus is performed by imaging a known intensity per unit area at the shock tube exit plane and by then comparing the resultant oscilloscope deflection with that from OH emission during a shock-tube run. The image is produced with the optics shown in the photograph in Fig. 35 and in the schematic diagrams in Figs. 33 and 46.

A General Electric 30A/T24/3 ultraviolet spectrum lamp was used as source. The SR 8 tungsten strip filament has a useful area of 46 x 3 mm. A 1-1/4 inches diameter, 1/16 inch thick, type 101 quartz window is attached through a graded tube seal. Power for the lamp was supplied by a 40 amp, 6 volt transformer power supply. Regulation was provided by use of a Sola constant voltage transformer. Current was read on either a Weston 0-to-30 amp or a Simpson 0-to-50 amp ammeter and could be varied through use of a carbon pile rheostat. Each time the lamp was used for a calibration, the filament brightness temperature (T_B) was measured with a Leeds and Northrup type 8622-C optical pyrometer. This instrument had been calibrated against another pyrometer and a blackbody. The ammeters were used only as a convenient auxiliary aid in obtaining the same intensity for each calibration. Two heavy-duty 12 volt wet cells in parallel were also used as a power supply for the lamp. However, this supply was found unsatisfactory because of intensity variations caused by battery drainage. Use of ac instead of dc current results in less than a 1% decrease in lamp intensity at 3000 A.[26] A small 50 cps light chopper was inserted in the calibration optical bench in order to permit the use of ac amplifiers.

The focal lengths of the lenses used in the calibration bench were measured as a function of wavelength in order to determine their radii of curvature. The focal lengths at 3090 A, the Perkin-Elmer wavelength setting for the quantitative runs, could then be calculated. Thick lens paraxial formuli were used.

The lamp filament is first imaged (1:1) on an accurately measured square source aperture of dimensions 1.519 ± 0.003 x 1.527 ± 0.003 mm. The aperture is then imaged at the shock tube exit plane by the second lens. The resulting magnification produces an image larger than the exit port. The solid angle of the calibration beam exceeds that of the shock tube exit optics ($\Delta\Omega_E$) thus permitting a calibration to be made. The lenses are carefully positioned according to their focal lengths calculated at 3090 A producing a monochromatically aligned calibration system. The aberrations introduced into the image at the exit port do not significantly affect the accuracy of our experiment since we may make suitable measurements to correct for them (see Section III B).

III. EXPERIMENTAL PROGRAM AND DATA ANALYSIS

A. Shock Tube Measurements

1. Experimental gas properties

Equilibrium computations of the gas properties (state functions) behind the incident and reflected shocks were made through use of relations expressing the conservation of energy, momentum, and mass and thermochemical data relating to the chemical species present (Ar, H_2O, OH, H_2, O_2, H, O).* The computations were performed at the Rand

* The heat of formation of OH used in this program is 9.27 kcal/mole.

Corp. with an IBM 704 program developed for the calculation of shock wave parameters by Dr. R. E. Duff of Los Alamos.*

The standard notation for state functions is used, as may be seen in Fig. 36. The subscript 1 refers to initial downstream conditions; 2, to conditions behind the incident shock; 3, to conditions behind the contact surface; 4, to the initial upstream conditions; and 5, to conditions behind the reflected shock with speed u_{sr}. We use p_2 and p_5 for total gas pressures and p_2* and p_5* for partial pressures of OH behind the incident and reflected shocks. The initial pressure (p_1) and temperature (T_1), the incident shock speed (u_s), and the initial test gas composition are all that are needed in order to determine the equilibrium state functions.

The calculations were performed for initial pressures of 20, 45, 50, and 55 mm of Hg with the percentage of H_2O varying from 0.25 to 2.00.** All quantitative experiments were made with $p_1 \simeq 50$ mm of Hg, and the final data used correspond to 0.67 to 1.40% of H_2O. Computations were made for temperatures behind the reflected shock (T_5) of about 3100 to 4400°K. For these values of T_5, the corresponding lower values of T_2 indicate that the kinetics of the thermal decomposition of H_2O is sufficiently slow[27] to justify the assumption that no significant reaction occurs in the gas behind the incident shock. Estimates made on the basis of data given in Ref. 27 show that the time constant for the formation

---

* Dr. Duff very kindly supplied us with a copy of his IBM deck.

** The variation of T_5 and u_{sr} with small changes of p_1 is negligible. For example, with $u_s = 1.3$ mm/μsec and a 1% H_2O test-gas, T_5 and u_{sr} decrease by about 0.2% for p_1 varying from 50 to 45 mm of Hg. However, this decrease in p_1 causes a 12% decrease in p_5*.

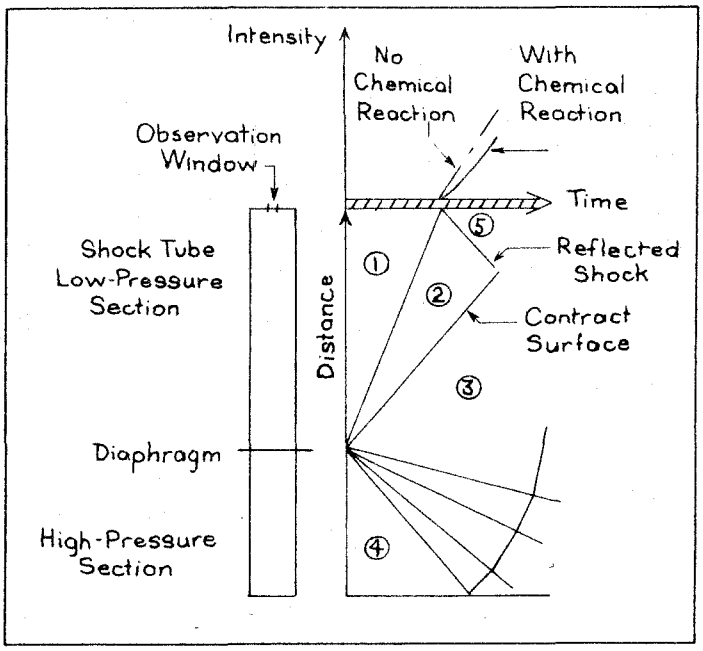

Fig. 36. Representative distance-time plot for the shock tube experiments.

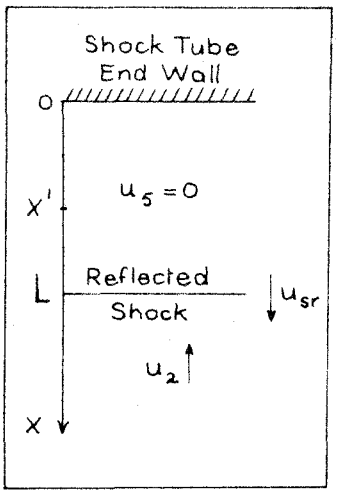

Fig. 37. Reflected shock coordinates.

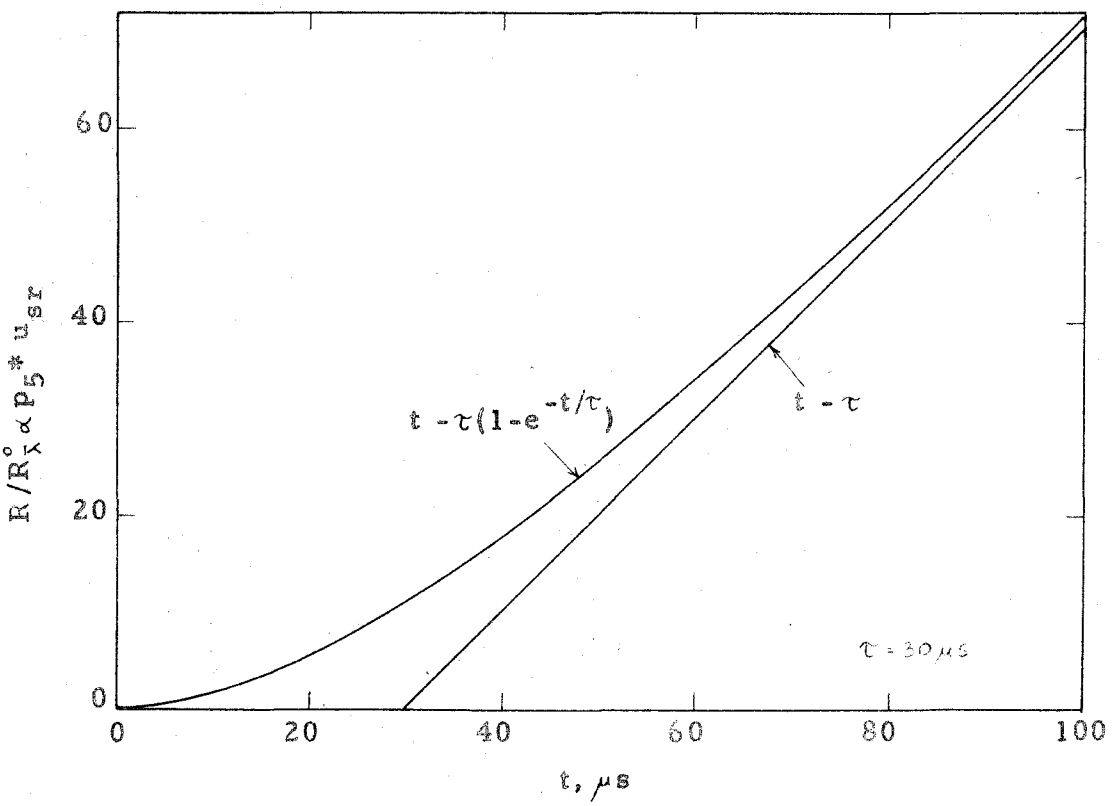

Fig. 38. Schematic diagram of the intensity-time profiles for a chemically-reacting gas with characteristic time constant τ.

of OH is* about 8000 μ sec at 2000°K with 0.68% H_2O present initially, whereas it is only about 20 μ sec at 4250°K. Therefore, the state function computations were made by considering no chemical reaction to occur behind the incident shock while, on the other hand, chemical equilibrium was assumed to exist behind the reflected shock wave. Calculations were also carried out for the case where no chemical reactions occur behind the reflected shock in order to estimate the temperature before chemical reaction occurs; a temperature of 4250°K directly behind the reflected shock is reduced to about 3920°K at chemical equilibrium for 0.68% H_2O present initially with p_1 = 50 mm of Hg.

Results of the calculations of T_5, u_{sr}, and p_5* as functions of u_s for p_1 = 50 mm of Hg appear in Figs. 39 to 42.

2. Qualitative data

Preliminary experiments were performed to determine (a) the presence of OH radicals in the shocked gas and (b) the presence of any impurities which radiate significantly in the region of the OH emission. Photographic spectra taken with a Hilger small quartz spectrograph established the presence of OH in the test gas, as may be seen in Fig. 43.

Further exploration of OH and impurity radiation was made through use of the JACO monochromator and a 1P28 photomultiplier. Runs were made at wavelength settings varying from 3070 to 3093 A with a spectral

* Inspection of Fig. 5 of Ref. 27 indicates that the OH concentration profile as a function of distance behind a shock may be represented approximately by an exponential curve.

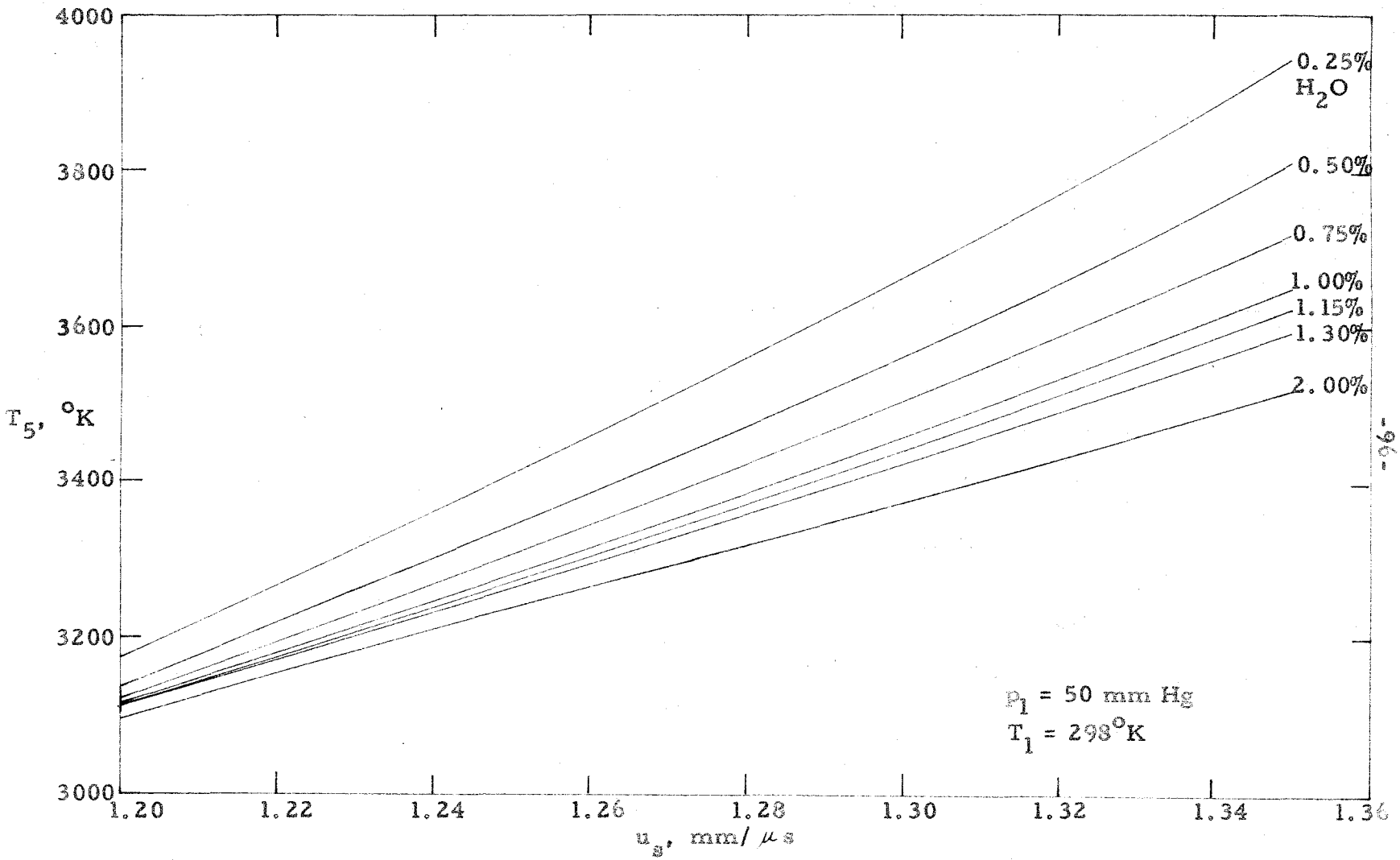

Fig. 39. Temperature T_5 behind the reflected shock as a function of incident shock speed u_s.

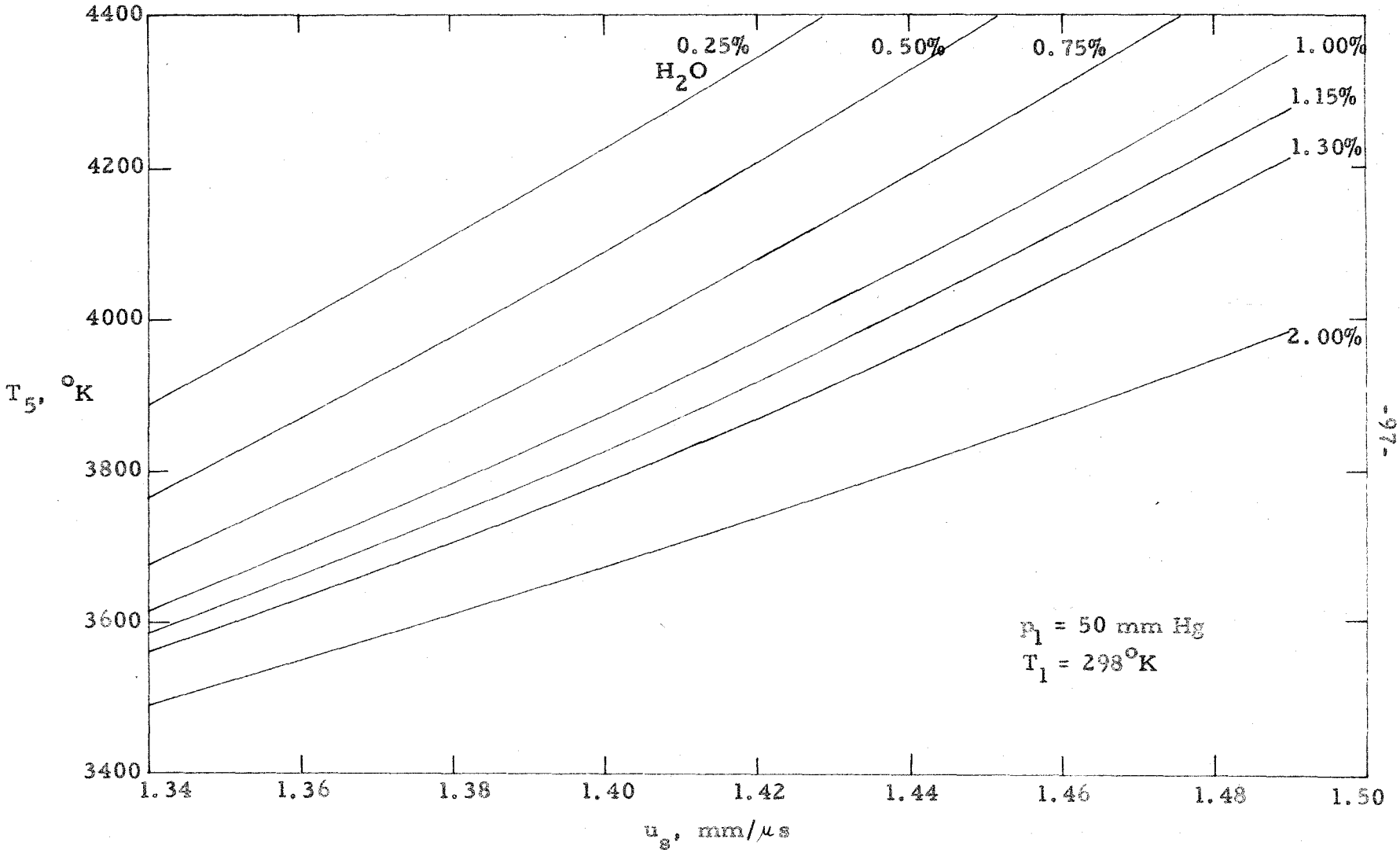

Fig. 40. Temperature T_5 behind the reflected shock as a function of incident shock speed u_s.

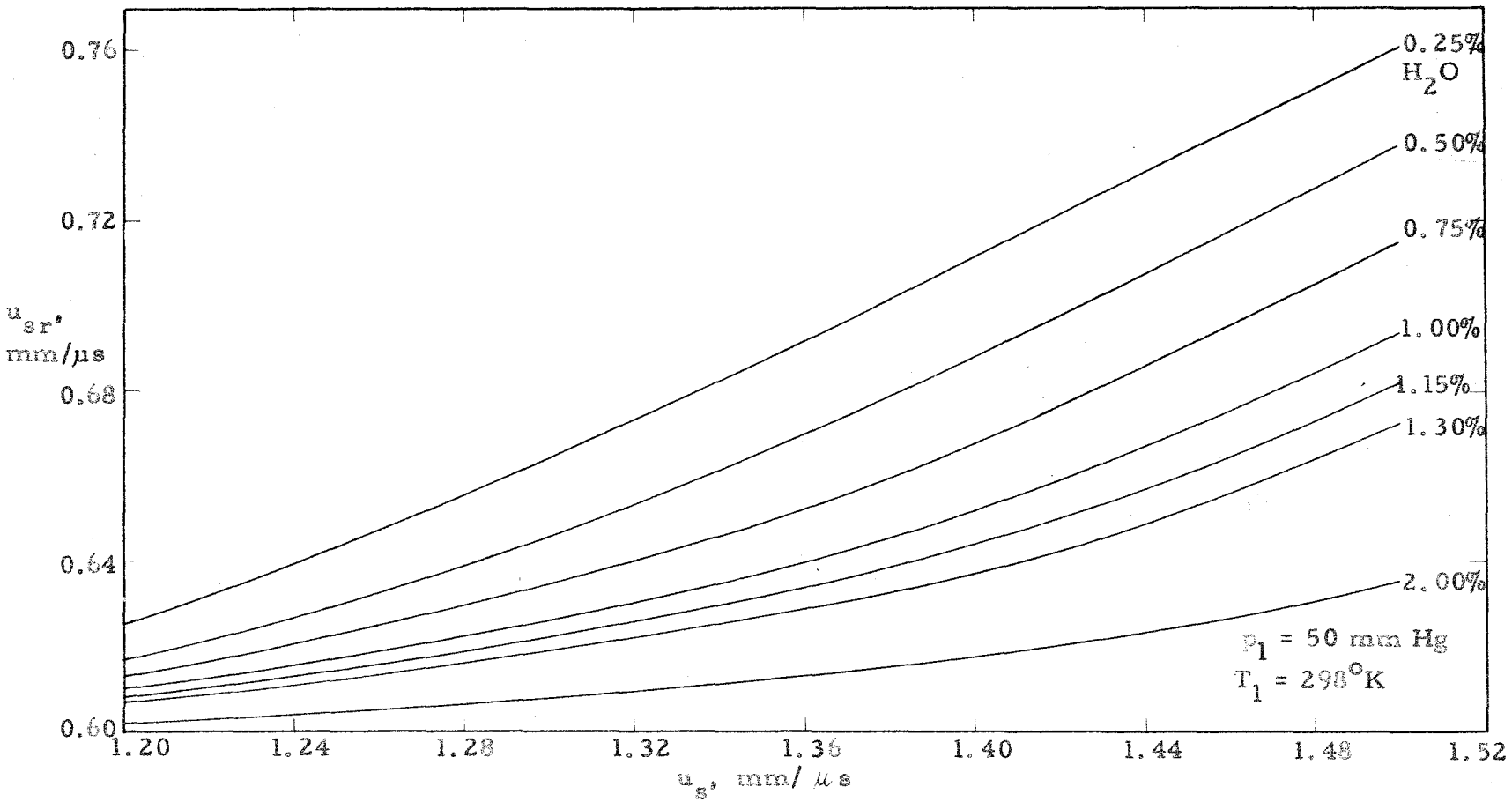

Fig. 41. Reflected shock speed u_{sr} as a function of incident shock speed u_s.

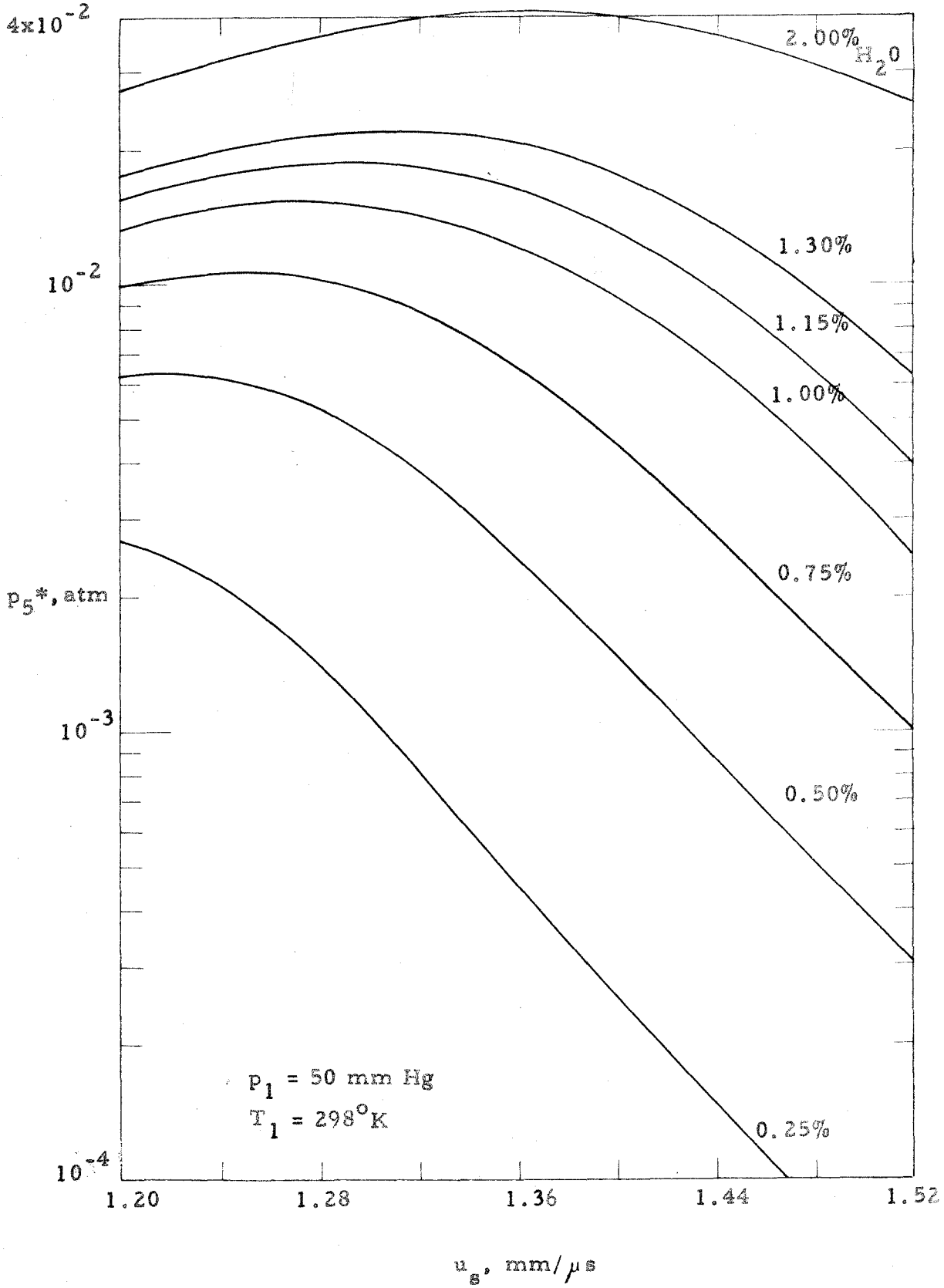

Fig. 42. Partial pressure p_5^* of OH behind the reflected shock as a function of incident shock speed u_s.

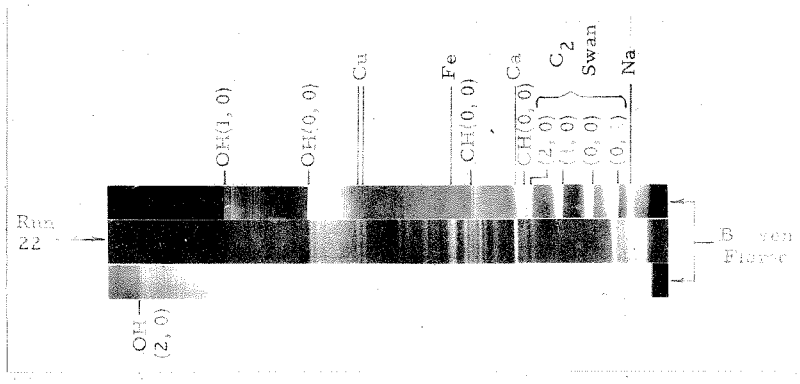

Fig. 43. The spectrum obtained from shock tube run 22 and two spectra taken with a Bunsen flame.

slit width of 8 A both with and without H_2O vapor added to the Ar. When the tube was properly cleaned and evacuated, the impurity radiation became negligibly small whereas a H_2O-Ar test-gas produced an essentially linear intensity-time profile.* The effects of not cleaning the tube thoroughly after the preceding run (using mylar diaphragms) and of not pumping the tube for a sufficiently long time were found to be quite similar, both leading to high levels of impurity radiation.

The Perkin-Elmer monochromator was used for quantitative runs since its dispersion exceeds that of the JACO instrument in the spectral region of interest and since the reduction of experimental data is simplified if the observed OH radiation corresponds, as nearly as possible, to the entire (0, 0)-band, $^2\sum \rightarrow {}^2\prod$ transitions of OH. In addition, use of

* After several hundred μ sec, the reflected shock intersects the contact surface and we consider the useful experiment to be ended. The intensity after reflection may either increase or decrease, depending upon the state functions and the presence of impurity materials.

a wide spectral slit width minimizes any errors introduced by slight misalignments. At 3090 A, the Perkin-Elmer instrument has a dispersion of 44.7 A/mm. Use of this instrument in Ar and Ar-H_2O runs indicated that, for a 1 mm slit width, the impurity level was still negligibly low.

3. Quantitative data

Sample oscillograms obtained with the Perkin-Elmer instrument set at 3090A with a 1 mm slit are shown in Figs. 44 and 45. These and the previously discussed linear traces suggest that the OH gas is optically transparent, and that the linear intensity rise is due to the linear growth of the optical depth (partial pressure of emitter times geometric path length) $X = p_5 * u_{sr} t$ for u_{sr} = constant. Estimates of the transparency of OH under the conditions of these experiments ($X \simeq 0.02$ to 0.1 cm-atm, $T_5 \simeq 3300$ to $3900^{\circ}K$, $p_5 \simeq 7.5$ atm) made according to available estimates of line intensities and half widths[18], [19], [20], [28] indicate that the gas is probably transparent for most of the spectral lines.

Quantitative interpretation of the data requires an explanation of the initial non-linear portion of the intensity-time curves. This non-linearity arises from the finite time required to form OH from H_2O, given a step pulse of temperature. The situation may be analyzed by reference to Fig. 37. Here we show the reflected shock at position x = L at time t after reflection. The gas at $x = x'$ will have been placed under conditions 5 for a time $t' = (L-x')/u_{rs}$. The partial pressure of OH at this station is given by $p_5 * (t')$. If we let R^{o}_{λ} = the average blackbody radiancy, α = the integrated intensity of the observed transitions, and X the optical depth,

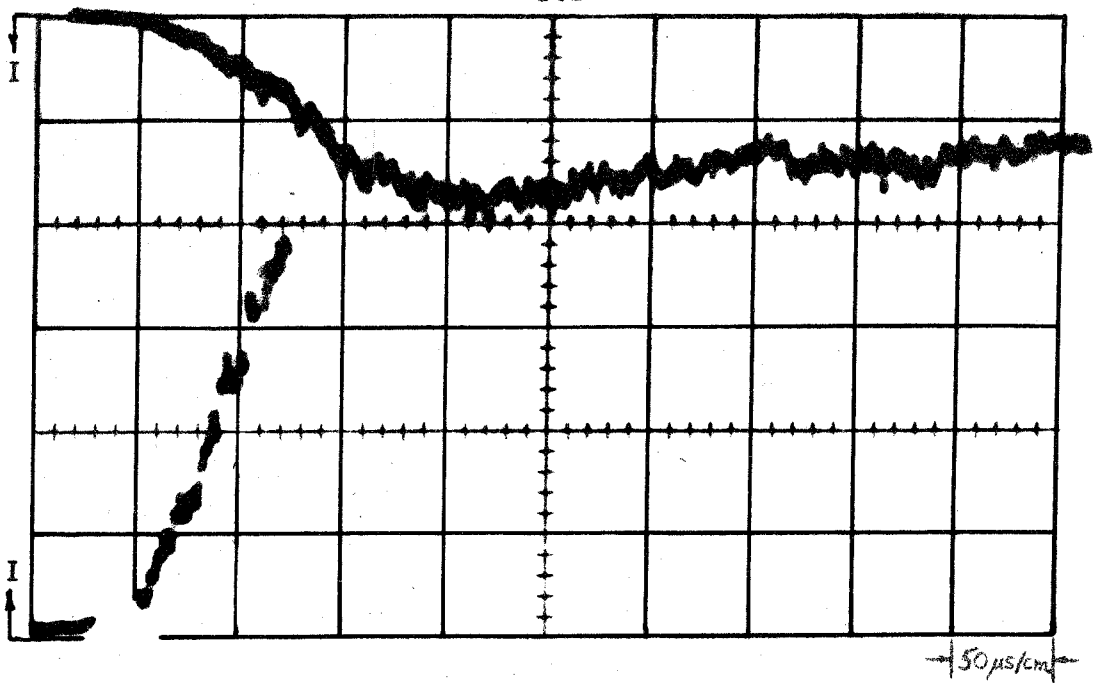

Fig. 44. Dual-beam oscilloscope traces for run 59 (1.24% H_2O, $p_1 \simeq$ 50.3 mm of Hg, $u_s \simeq 1.27$ mm/ μs). The OH emission has been measured with two different gains. Intensity increases downward for the upper trace (5 mv/cm) and upward for the lower trace (1 mv/cm).

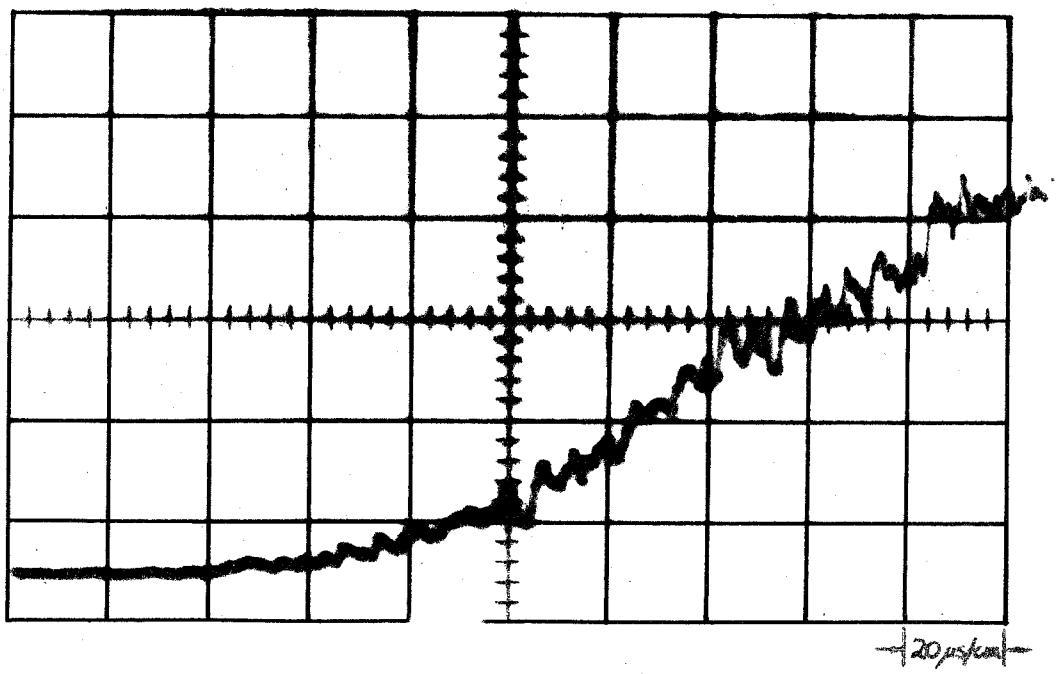

Fig. 45. Single-beam oscilloscope trace for run 65 (1.15% H_2O, $p_1 \simeq 50.3$ mm of Hg, $u_s \simeq 1.27$ mm/ μs).

we obtain for the (axial) radiancy (in erg/sec-cm^2-steradian) $R = R^o_{\bar{\lambda}} a x$:

$$R = R^o_{\bar{\lambda}} a \int_0^L p_5^*(t')dx' = R^o_{\bar{\lambda}} a p_5^* \int_0^L f_o\left(\frac{L-x'}{u_{sr}}\right) dx'$$

where $p_5^*(t) = p_5^* \times f_o(t)$, p_5^* is the value of OH partial pressure at chemical equilibrium, $f_o(0) = 0$ and $\lim_{t\to\infty} f_o(t) = 1$. An appropriate form for $f_o(t)$ is $1-\exp(-t/\tau)$ where τ is defined as the time constant for the reaction (see discussion in Section 1). We obtain

$$\frac{R}{R^o_{\bar{\lambda}} a p_5^*} = \int_0^L \left[1-\exp\left(-\frac{L-x'}{\tau u_{sr}}\right)\right] dx'$$

$$= L - \int_0^L \exp\left(-\frac{L-x'}{\tau u_{sr}}\right) dx'$$

$$= L + \tau u_{sr} \int_{L/\tau u_{sr}}^0 e^{-v}\, dv$$

$$= L - \tau u_{sr}\left[1-e^{-L/\tau u_{sr}}\right].$$

Since $L = u_{sr}t$, we may write

$$R = R^o_{\bar{\lambda}} a p_5^* u_{sr}\left[t - \tau(1-e^{-t/\tau})\right]. \qquad (54)$$

For t large compared with τ, we have

$$R \simeq R^o_{\bar{\lambda}} a p_5^* u_{sr}(t-\tau). \qquad (55)$$

For $t = \tau$

$$R = R\frac{o}{\lambda}\, a\, p_5^*\, u_{sr}\tau(1/e). \tag{56}$$

For t small compared with τ,

$$R \simeq R\frac{o}{\lambda} a\, p_5^*\, u_{sr}(t^2/2\tau). \tag{57}$$

Results obtained from Eqs. (54) and (55) for $\tau = 30\mu$ sec are plotted in Fig. 38. The shape of the curve obtained from Eq. (54) is seen to be very close to the experimental results as seen in Fig. 45.

In the absence of knowledge of the chemical kinetics relating to OH formation, other than estimates of τ made from the data of Ref. 27, a convenient method for reducing the results of our experiments is obtained by fitting a straight line to the measured intensity-time data in correspondence with the relative positions of the two curves shown in Fig. 38. From Eq. (55) we may then obtain values for $a = R/R\frac{o}{\lambda} p_5^* u_{sr}(t-\tau)$ that are directly proportional to the f-number. Rough estimates for τ from our data are reasonably close (within 20%) to approximate estimates derived from the Los Alamos data.

B. Calibration Procedures

In order to reduce the experimental data, we must now perform the following absolute calibrations:

(1) we must estimate the fraction of the total intensity to which our system responds, i.e., we must measure the instrumental slit function;

(2) we must estimate the absolute intensity of the source radiancy that is actually imaged at the shock-tube exit port and is then recorded by the detector;

(3) we must relate the instrumental output to the absolute incident energy flux.

Schematic diagrams of the optical system used for intensity calibrations and for converting observed intensities to absolute intensities are drawn in Fig. 46. If we let R_T represent the total radiant flux (ergs/sec) produced by heated OH, we obtain

$$R_T \simeq \left(\begin{array}{l}\text{source radiancy } R_s \\ (\text{ergs/cm}^2\text{-sec-A-} \\ \text{steradian})\end{array}\right) \times \left[\left(\begin{array}{l}\text{source solid} \\ \text{angle } \Delta\Omega_s \text{ sub-} \\ \text{tended by the} \\ \text{source optics} \\ (\text{steradian})\end{array}\right) \times \left(\begin{array}{l}\text{source} \\ \text{area} \\ \Delta A_s \\ (\text{cm}^2)\end{array}\right) \times \left(\begin{array}{l}\text{wavelength} \\ \text{interval} \\ \Delta\lambda(\text{A})\end{array}\right)\right]$$

$$\times \left(\begin{array}{l}\text{intensity loss factor F} \\ \text{due to quartz optics,} \\ \text{off-axis rays, and the} \\ \text{ratio of the shock tube} \\ \text{exit port area to the} \\ \text{area of the image made} \\ \text{of the source}\end{array}\right) \times \left(\begin{array}{l}\text{ratio Y of the intensity} \\ \text{of the shock tube data} \\ \text{(mv) per mv of the} \\ \text{calibration intensity} \\ \text{corresponding to } R_s\end{array}\right). \qquad (58)$$

The quantity R_T is related to the expression given for R in Eqs. (54) to (57) as follows:

R_T = R × (solid angle subtended by the receiver optical system)

× (shock-tube exit area actually viewed).

The effect of the slit function on Eq. (58) must still be considered.

1. Monochromator slit function

A monochromator is characterized by a slit function $g(|\lambda - \lambda_o|, b')$ which indicates the response of the instrument at wavelength λ when

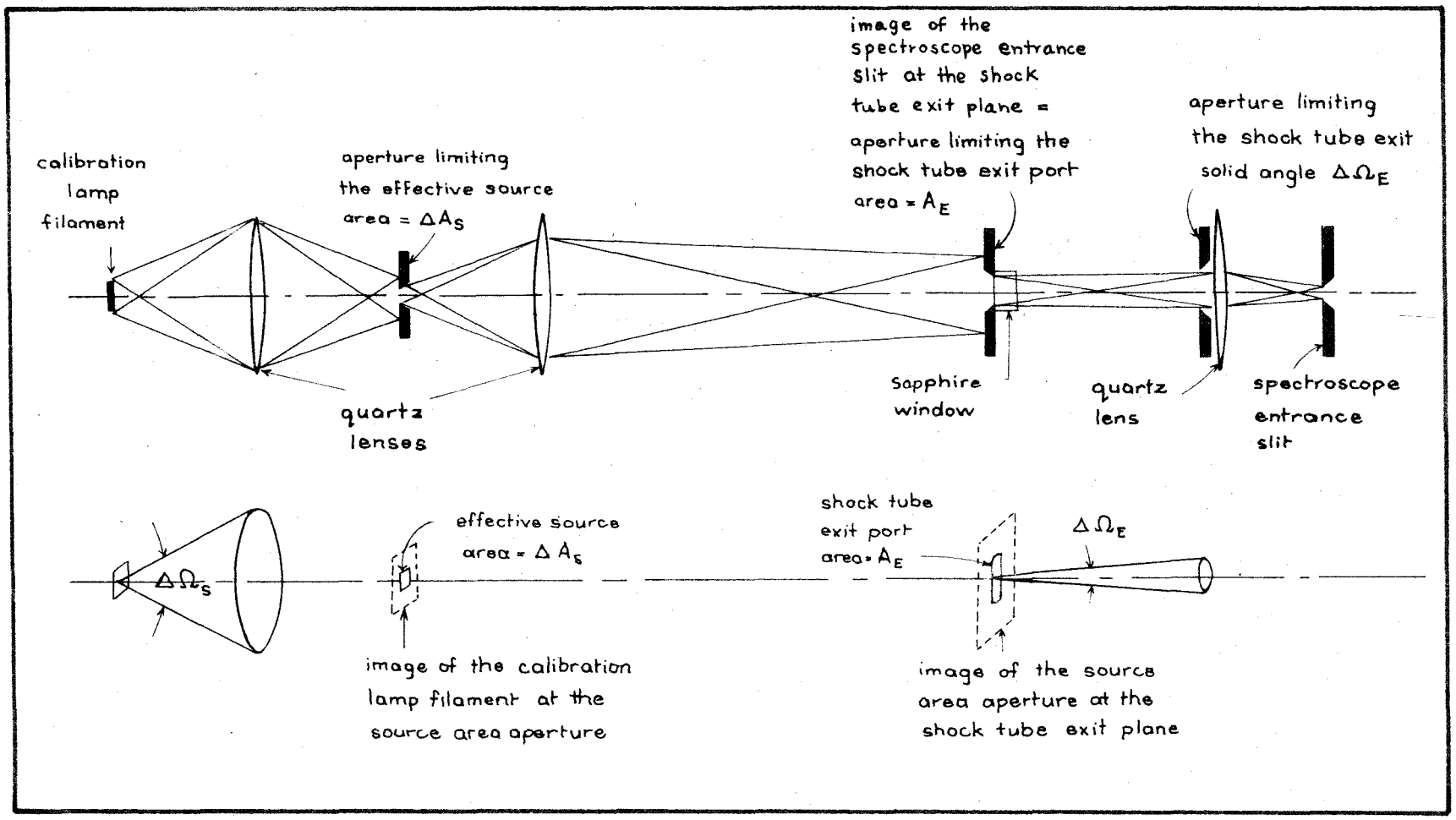

Fig. 46. Schematic diagram of the optical system used for intensity calibrations and for converting observed intensities to absolute intensities.

it is set at λ_o. Here b' represents all of the instrumental constants. For a prism spectrograph, the entrance slit of which is uniformly filled with radiation, we expect the slit function to be of triangular shape if we neglect small variations of prism dispersion with wavelength. The base of the triangle is expected to equal twice the spectral slit width if the instrument is aligned perfectly.

An experimental determination of the slit function was performed by imaging the low-pressure Hanovia mercury lamp on the spectroscope slits. The central portion of the U-shaped lamp was placed at the high-pressure end of the shock tube in such a fashion that a line image was formed at right angles to the slits. After setting at a given slit width, selected mercury lines were scanned mechanically and the resulting output displayed with a pen recorder. Since no strong isolated mercury line exists within the spectral interval used for the shock tube runs, scans were made of available nearby lines. All scans indicated that the slit function base exceeded the ideal value. A relatively isolated strong line exists at 4358 A. Repeated scans with mechanical slits varying in width from 0.3 to 1.0 mm indicated that the ratio D of the measured slit function base to the calculated value is 1.52 to within 3%. A check on the validity of using this value of D for the spectral region of these experiments was made by scanning the closely spaced mercury lines at 3131.8, 3131.6 and 3125.7 A with a 1 mm slit width. A value of D almost exactly equal to the value quoted above was obtained.

Since the prism dispersion at 3090 A is such that the effective width is 2 x 44.7 A/mm, the base of the triangular slit function for the shock-

tube experiments, with a 1 mm slit, is 1.52 x 2 x 44.7 = 136 A. This slit function has been drawn in Fig. 47 together with data from the extensive tabulation of relative intensities of the OH uv transitions given in Ref. 28. These relative intensity data will be discussed in Section C. Since the slit function is triangular, its effect upon the calibration procedure is to make the wavelength interval $\Delta\lambda$ in Eq. (58) equal to 1/2 of the spectral base of the slit function, i.e., approximately 68 A.

2. Determination of the intensity loss factor F

Since the optics of the calibration bench have been placed according to paraxial calculations, the computed source intensity per unit area imaged at the shock tube end plane applies only in the limit as the exit area approaches zero. We correct for the finite area A_E of the shock tube exit port through use of the factor

$$B = \frac{\text{calibration intensity per unit area at the shock tube exit plane for exit area } A_E}{\lim_{\text{exit area} \to 0} (\text{calibration intensity per unit area at the shock tube exit plane})}$$

In order to determine B, a set of accurately machined apertures was placed at the shock tube end plane and the oscilloscope deflections determined for each aperture. Ten apertures of diameters from 0.95 to 10.5 mm were used and the resulting relative values of intensity per unit area plotted as a function of the exit area. For diameters less than about 6 mm, the relative intensity per unit area was constant to within about 7%. The value of B obtained was 0.83.

Another contribution to the loss factor F comes from the reflection

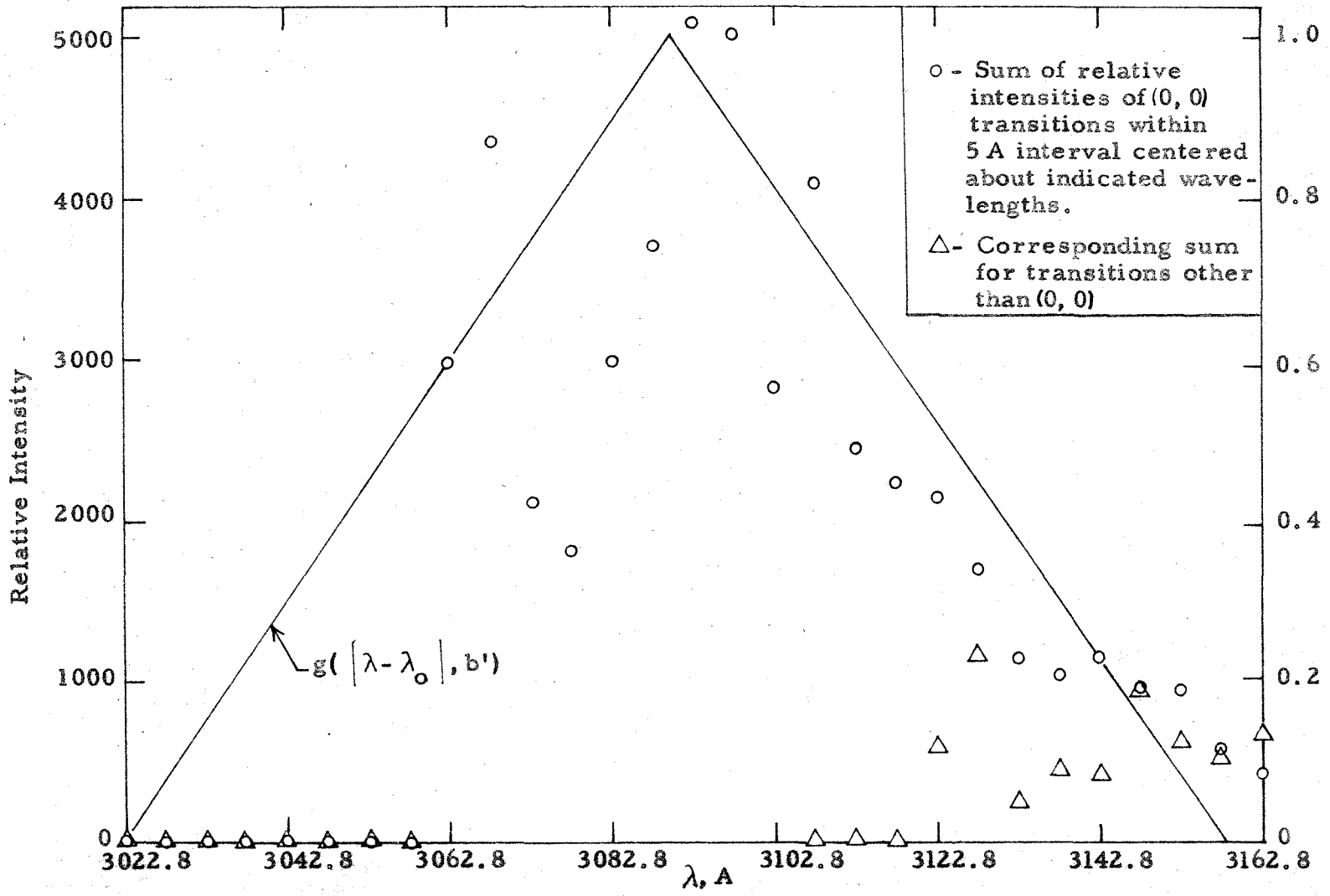

Fig. 47. Relative intensities of OH $^2\Sigma \rightarrow {}^2\Pi$ transitions over a selected portion of the spectrum.[28] Intensities lying between 0 and 30 on the scale used for the abscissa are indicated as 0. The spectroscopic slit function g is also shown.

losses at the six quartz surfaces of the calibration bench. The fractional transmissivity Q of these quartz optics is approximately equal to 0.792. We finally consider the fraction U of the source image at the shock tube exit plane that falls within the exit port area $A_E \simeq 0.486$ cm^2. The magnification of the effective source area $\Delta A_s \simeq 0.0232$ cm^2 is such that $U \simeq 0.486/2.73 = 0.178$. We finally obtain $F = BQU \simeq 0.117$.

3. Relation of shock-tube intensity data to absolute intensity calibration

We shall now describe how the parameter Y in Eq. (58) was determined. In order to ensure a reasonable lifetime for the calibration lamp, it was operated at its rated current of 30 amps resulting in a filament (source) temperature T_s of about 2090°K as measured by a Leeds and Northrup pyrometer. The source intensities at 2090°K are too low to permit a good absolute calibration at 3090 A. Therefore, relative intensity calibrations were performed at three other wavelengths for each run, and these relative intensity calibrations were related to an absolute calibration at 3090 A after all runs had been completed. This absolute calibration* was performed by operating the lamp at approximately 40 amps with $T_s \simeq 2440$°K. The relative calibrations were performed at the following three wavelengths (λ_o = 3800, 3920, and 4120 A.

We let $R' = R_s \Delta\Omega_s \Delta A_s \Delta\lambda F$ ergs/sec and I_c' = the receiver signal in mv for an absolute calibration at 3090 A and 2440°K. Then R'/I_c' = the absolute energy flux in ergs/sec per mv of receiver output. We also

* A calibrated 1000 gain Tektronix Type 122 low-level battery-operated preamplifier was used for this measurement.

let I = the receiver signal in mv for OH emission as measured from our shock-tube data. Thus, if the photomultiplier sensitivity and the electronic gain did not change with time, $(R'/I_c')I$ = the absolute radiant flux in ergs/sec corresponding to the OH emission from a shock-tube run. Since the gain and sensitivity actually change somewhat with time, the relative intensity calibrations were performed immediately following each run. We let $I_c(\lambda_o)$ = the receiver signal in mv obtained from one of these relative calibrations at λ_o and T = 2090°K. We also let $I_c^*(\lambda_o)$ = the corresponding signal obtained under the same conditions of photomultiplier sensitivity and electronic gain as existed during the absolute intensity calibration. Therefore, $\left[I_c^*(\lambda_o)/I_c(\lambda_o)\right](I)$ gives the receiver signal for OH emission from the shock tube corrected to the conditions of the absolute calibration. We finally obtain

$$Y = \left[\frac{I_c^*(\lambda_o)}{I_c(\lambda_o)}\right]\frac{I}{I_c'}$$

= the receiver signal $\left[I_c^*(\lambda_o)/I_c(\lambda_o)\right](I)$ in mv for the flux in erg/sec emitted from the heated OH in the shock tube divided by the receiver signal (I_c') in mv corresponding to the flux in erg/sec originating from the calibration source for the amplification scale and photomultiplier sensitivity existing in the OH radiant flux measurement.

We may now use Eq. (58) to relate our observed radiant flux in the shock-tube studies to the absolute intensity calibration, viz.,

$$R_T \simeq R_s \, \Delta\lambda \, \Delta\Omega_s \, \Delta A_s \, F \frac{I_c^*(\lambda_o)}{I_c(\lambda_o)} \frac{I}{I_c'} \text{ ergs/sec} . \tag{58a}$$

Here R_s = radiancy of the calibration lamp at 3090 A and 2440°K $\simeq$ 10.3 ergs/sec-cm^2-A-steradian,[29] $\Delta\lambda \simeq 1/2$ the spectral base of the triangular slit function $\simeq$ 68 A, $\Delta\Omega_s$ = solid angle associated with the calibration source 0.00400 steradian, ΔA_s = source area $\simeq$ 0.0232 cm^2, and F = intensity loss factor $\simeq$ 0.117. The absolute intensity calibration oscilloscope deflections I_c^* were found to be equal to 0.975 mv at 3800 A, 1.83 mv at 3920 A, and 3.90 mv at 4120 A and the deflection I_c' was found to be 0.0343 mv. We finally obtain

$$R_T \times \frac{I_c}{I} = \left\{ \begin{array}{l} 0.216 \text{ ergs/sec for calibration at 3800 A} \\ 0.406 \text{ ergs/sec for calibration at 3920 A} \\ 0.865 \text{ ergs/sec for calibration at 4120 A} \end{array} \right\} . \tag{58b}$$

C. Calculation of the f-Number

The integrated intensity $a_{(0,0)} = \int_{(0,0)\text{-band}} P_\lambda \, d\lambda$ is related to the f-number through

$$a_{(0,0)} \simeq \frac{\pi e^2}{mc^2} \frac{N_\ell}{p} \lambda_o^2 \, f \simeq 0.0227 \left(\frac{273}{T}\right) f \text{ atm}^{-1} \tag{59}$$

where λ_o = 3090 A, p = pressure in atm and N_ℓ = number of molecules per unit volume in the ground state. The induced emission term has been omitted since it is practically unity. Also $N_\ell \simeq$ total number of molecules per unit volume. The f-number defined by Eq. (59) is the total f-number for the (0, 0) vibrational band of the $^2\Sigma \rightarrow {}^2\Pi$ transitions of OH.

Since the OH radiators are in the linear part of the curves of growth, we may use Eq. (55) to relate the partial integrated intensity a' of those OH transitions that make contributions falling within the limits of the slit function to the experimentally measured radiant flux R_T. Thus

$$R_T = R \Delta\Omega_E A_E = R^o_\lambda \Delta\Omega_E A_E a' p_5 * u_{sr}(t-\tau). \qquad (60)$$

The influence of the slit function upon this result is to replace

$$a' = \sum_{\substack{\text{all OH transitions} \\ \text{for which the slit} \\ \text{function is non-zero}}} S_J$$

by the expression

$$a' = \sum_{\substack{\text{all OH transitions} \\ \text{for which the slit} \\ \text{function is non-zero}}} g(|\lambda - \lambda_o|, b') S_J,$$

where S_J is the integrated intensity of the Jth line at wavelength λ and where λ_o is the wavelength of the spectroscope setting. For the measured triangular slit function* and $\lambda_o = 3090$ A, we may compute the ratio

---

* Inaccuracies in the measurement of the slit function do not materially alter this result since most of the intensity is concentrated near the center of the slit function.

$$G = \frac{\sum_{\substack{\text{all OH transitions for which the slit function is non-zero}}} g(|\lambda - \lambda_o|, b')S_J}{\sum_{\substack{\text{all (0, 0)-band transitions for which the slit function is non-zero}}} S_J} = 0.67 \qquad (61)$$

from the relative intensities tabulated in Ref. 28 (cf. Fig. 47).* The correct value of the integrated intensity ($a_{(0,0)}$) of the (0, 0)-band is then given by

$$a_{(0,0)} = a'/G = a'/0.67. \qquad (62)$$

Using the values $A_E = 0.486$ cm^2 and $\Delta\Omega_E = 3.40 \times 10^{-5}$ steradian, we obtain from Eqs. (59), (60), and (62)

$$f \simeq 0.0398\, R_T/R^o_\lambda\, p_5^*\, u_{sr}(t-\tau)(273/T_5), \qquad (63)$$

where R^o_λ is in ergs/sec-cm^2-A-steradian. We are now able to compute the f-number from our experimental calibration and shock-tube data through use of Eq. (63) together with the three numerical relations given as Eq. (58b). The resultsof eight experimental determinations of f with T_5 varying from 3330°K to 3925°K, the composition varying from 0.67% to 1.40% H_2O, and $p_1 \simeq 50$ mm of Hg is

$$f = (0.90 \pm 0.10) \times 10^{-3}$$

for the (0, 0)-band, $^2\Sigma \rightarrow {}^2\Pi$ transitions of OH. The indicated 10% uncertainty represents the rms scatter of the shock-tube data.

---

* These relative intensities were measured experimentally from high-dispersion spectra of flames and checked by theoretical predictions.

D. Discussion of Results and Error Estimates

Previously published values for the f-number are 1.2×10^{-3} (Oldenberg and Rieke[18]), 0.6×10^{-3} (Dyne[19]) and 1.3×10^{-3} (Carrington[20]). When corrected to equivalent thermodynamic data for the computation of the partial pressures of OH, Oldenberg and Rieke's value is reduced to about 1.0×10^{-3}.

Oldenberg and Rieke and Dyne used similar experimental techniques. Both produced OH radicals by heating H_2O-O_2 mixtures in furnaces to about 1400 to 1500°K. Densitometer records of photographic absorption spectra were used to provide the absorption coefficient profiles (P_ω) of selected lines. The line integrated intensities (S) were obtained through use of the relation $S_{line} = \int_{line} P_\omega d\omega$ and were then corrected by extrapolation to "zero intensity". Carrington's measurements were carried out with various H_2-O_2 flames. The f-number was measured by the "curve-of-growth" method* in which the total line absorptions are plotted as a function of

log(constant x partial pressure of absorbing particles x relative line f-number).

Fitting this experimental curve of growth to an absolute curve of growth[7] then determines the f-number by fixing the constant in the expression for the abscissa.

An overall estimate of the experimental accuracy in our experiments is about ± 60%, i.e., $f = (0.9 \pm 0.5) \times 10^{-3}$ although it is difficult

* Dyne also measured the f-number by the curve-of-growth method and obtained a value about 10% lower than his "best" value.

to give an exact figure because of uncertainties in the temperature T_5. About 10% of this error estimate arises from quantities associated with the source optics; about 10% from the shock tube data and state functions; and about 40% from the intensity calibrations and shock tube exit optics.

Several compensating effects tend to make T_5 somewhat uncertain: (1) reflected shock velocities u_{sr} in Ar lower than those calculated from the usual gasdynamic relations have been observed experimentally[30], [31] and predicted theoretically.[32] These lower reflected shock velocities correspond to lower temperatures T_5. (2) The OH formed immediately behind the reflected shock is initially at a higher temperature than the calculated equilibrium value of T_5. (3) It is possible that excessive populations of OH in the $^2\sum$ state may be produced behind shock fronts as is known to occur in flames. This problem can be settled only by performing a difficult, time-resolved population temperature measurement for the OH radicals formed behind a shock wave. We note that the first effect tends to make our computed f-number too small while the second and third effects tend to make it too large.

We may correct roughly for the first effect by modifying u_{sr} according to a procedure given by Goldsworthy.[32] A correction to u_{sr} due to heat conduction to the end wall of the shock tube is given, such that the reduction in u_{sr} varies inversely with $\sqrt{t}$. Estimates made from Goldsworthy's relations indicate that this reflected shock velocity reduction is about 1% over the range of time considered in our shock-tube experiments. A small decrease of u_{sr} produces negligibly small changes in our calculations except for a decrease of T_5 of about 100°K. Since the

blackbody radiancy depends exponentially on T_5, this temperature decrease corresponds to an f-number increase of about 30%.

We may estimate the magnitude of the second effect, by considering a temperature decrease with time for the OH formed behind the reflected shock estimated from calculations of the state functions made for assumed chemical equilibrium behind the reflected shock and for no chemical reaction behind the reflected shock. For the conditions of our shock-tube experiments, this effect may decrease the f-number by roughly 15%. The possibly large effects associated with chemiluminescent radiation cannot be estimated theoretically.

REFERENCES

1. McAdams, W.H., Heat Transmission, Third Ed.; Ch. 4, Radiant Heat Transmission by H.C. Hottel, p. 83, McGraw-Hill Book Co., Inc., New York, 1954.

2. Hottel, H.C., and Mangelsdorf, H.G., Trans. Am. Inst. Chem. Engrs. 31, 517-549 (1935).

3. Hottel, H.C., and Smith, V.C., Trans. ASME 57, 463-470 (1935).

4. Herzberg, G., Infrared and Raman Spectra of Polyatomic Molecules, p. 274, D. Van Nostrand Co., Inc., New York, 1945.

5. Mayer, H., Los Alamos Scientific Laboratory Report LA-647 (1947).

6. Goody, R.M., Quart. J. Roy. Met. Soc. 78, 165-169 (1952).

7. Penner, S.S., Quantitative Molecular Spectroscopy and Gas Emissivities, p. 409, Addison-Wesley Pub. Co., Inc., Reading, Mass., 1959.

8. Plass, G.N., J. Opt. Soc. Am. 49, 821-828 (1959).

9. Kaplan, L.D., and Eggers, Jr., D.F., J. Chem. Phys. 25, 876-883 (1956).

10. Plass, G.N., J. Opt. Soc. Am. 48, 690-703 (1958).

11. Plass, G.N., "Emissivity of the 4.3 Micron Band of Carbon Dioxide", ASI Publication No. U-238, Aeronutronic, A Division of Ford Motor Co., Glendale, Calif. (1958).

12. Howard, J.N., Burch, D.L., and Williams, D., Contract AF 19(604)-516, Air Force Cambridge Research Center, Ohio State University Research Foundation, Columbus (1954).

13. Tourin, R., Rept. No. 258, Warner and Swasey Research Corp., New York, 1954.

14. Edwards, D.K., Ph.D. Thesis, University of California, Berkeley, 1959.

15. Tourin, R.H., and Henry, P.M., "Infrared Spectral Emissivities and Internal Energy Distributions of Carbon Dioxide and Water Vapor at High Temperatures", The Warner and Swasey Co., Control Instrument Division, New York, AFCRC-TR-60-203 (1959).

16. Ferriso, C.C., Rocket Plume Radiance, Vol. III, "The Temperature, Spectrum, and Emissivity of Exhaust Gases from a Small Rocket", Report No. AZR-014, Vol. III, Convair (Astronautics), San Diego, (1960).

17. See, for example, Keck, J., Camm, J., and Kivel, B., J. Chem. Phys. 28, 723-724 (1958); Keck, J., Camm, J., and Wentink, Jr., T.W., Annals of Physics 7, 1-38 (1959); Wurster, W.H., Glick, H. S., and Treanor, C.E., "Radiative Properties of High Temperature Air", Report No. QM-997-A-2, Cornell Aeronautical Lab., 1958.

18. Oldenberg, O., and Rieke, F.F., J. Chem. Phys. 6, 439-447 (1938); See also Dwyer, R.J., and Oldenberg, O., J. Chem. Phys. 12, 351-361 (1944).

19. Dyne, P.J., J. Chem. Phys. 28, 999-1000 (1958).

20. Carrington, T., J. Chem. Phys. 31, 1243-1252 (1959).

21. Rabinowicz, J., Jessey, M.E., and Bartsch, C.A., J. Appl. Phys. 27, 97-98 (1956).

22. Kebler, R.W., "Optical Properties of Synthetic Sapphire", Linde Air Products Co., A Division of Union Carbide and Carbon Corp., New York.

23. Allen, C.W., Astrophysical Quantities, p. 102, University of London, The Athlone Press, London, 1955.

24. General Electric Co., Willoughby Quartz Plant, Willoughby, Ohio (personal communication).

25. Instruction Manual, Perkin-Elmer Infrared Equipment, Vol. 1, Introduction to Infrared Spectrometry.

26. Condell, W.J., and Byrne, F.T., J. Opt. Soc. 47, 1135-1136 (1957).

27. Bauer, S.H., Schott, G.L., and Duff, R.E., J. Chem. Phys. 28, 1089-1096 (1958).

28. Dieke, G.H., and Crosswhite, H.M., "The Ultraviolet Bands of OH", Bumblebee Report No. 87, The Johns Hopkins University, 1948.

29. "Tables for the Spectral Radiant Intensity of a Blackbody and of a Tungsten Ribbon", Rocketdyne Research Report No. 59-32.

30. Strehlow, R.A., and Cohen, A., J. Chem. Phys. 30, 257-265 (1959).

31. Toennies, J.P., and Greene, E.F., J. Chem. Phys. 26, 655-662 (1957).

32. Goldsworthy, F.A., J. Fluid Mech. 5, 164-176 (1959).